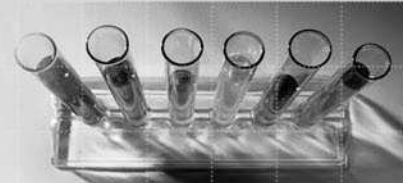




Air Turbine Design Study for a Wave Energy Conversion System



by
Paul Henry Ackerman

Thesis presented in partial fulfilment of the requirements for the degree M.Sc.
Engineering at the University of Stellenbosch

Supervisor: Prof. T.W. von Backström

Co supervisor: Prof. J.L. van Niekerk

Department of Mechanical and Mechatronic Engineering

University of Stellenbosch

Private Bag X1, Matieland 7602, South Africa

29/10/2009

Declaration

I, the Undersigned, hereby declare that the work contained in this dissertation is my own original work and that I have not previously in its entirety or in part submitted it at any university for a degree.

Signature:

P. H. Ackerman

Date:

Abstract

Objectives of this study are threefold. Firstly a numerical model of the airflow through the Stellenbosch Wave Energy Converter (SWEC) is developed. Secondly a turbine and diffuser are specified and designed for operation in the SWEC. Thirdly the operation and performance of the turbine is studied under various flow conditions and for both constant and variable speed.

The airflow system is modelled using Simulink (Mathworks, 2008), the results of which predict a power curve that follows experimental scale model results up to a wave height of 3m. Results from this modelling process at the design wave condition (2m) are used for specification and design of the turbine and diffuser. Turbine design is initiated by investigating turbine layout and expected performance with a non-dimensional analysis. An algorithm is written to calculate flow over the turbine stage at sections throughout the blade length to determine an estimate of performance. The turbine blade is assembled by stacking blade sections between hub and shroud. A Computational Fluid Dynamics (CFD) analysis is used to gauge the performance of the turbine under various flow conditions. The diffuser is modelled at design conditions only to limit computational time.

The airflow system model overestimates performance of SWEC in wave heights larger than 3m; this overestimation is believed to stem from inaccurate estimations of added mass and damping. The results of the CFD analysis validate the turbine design assumptions at the design conditions. The constant speed turbine design approach to negate the use of expensive variable speed generators proved ineffective at off-design conditions, with stall occurring in the rotor blade row for wave heights above 3m. Poor turbine performance is predicted for wave heights of 1.5m and less. Variable speed turbine operation was modelled and improved poor performance at off-design conditions.

Uittreksel

Doelwitte van hierdie studie is drievoudig. Eerstens word 'n numeriese model van die lugvloei deur die Stellenbosch Golf Energie Omsetter (SGEO) ontwikkel. Tweedens word 'n turbine en diffusor gespesifiseer en ontwerp vir gebruik in die SGEO. Derdens word die werking van die turbine bestudeer onder verskeie vloeitoestande vir beide veranderlike en konstante spoed.

Die lugvloei stelsel word gemodelleer met die gebruik van Simulink (Mathworks, 2008). Die resultate voorspel 'n kragkurwe wat die eksperimentele skaalmodel resultate tot by 'n golf-hoogte van 3m navolg. Resultate van hierdie modelleringsproses by die ontwerp golftoestand (2m) word gebruik vir die spesifikasie en die ontwerp van die turbine en diffusor. Turbine ontwerp word aangepak deur 'n ondersoek van turbine uitleg en verwagte vertoning deur dimensielose analise. 'n Algoritme word geskryf om vloei oor die turbine stadium te bereken by seksies dwarsdeur die lem lengte om 'n beraming van die vertoning te bepaal. Die turbinelem word saamgestel deur lemseksies tussen die naaf en omhulsel te stapel. 'n Berekeningsvloeidinamika (BVD) analise word gebruik om turbine vertoning te bepaal onder verskillende vloei omstandighede. Die diffusor word gemodelleer by ontwerpstoestande slegs om berekeningstyd te beperk

Die lugvloei stelsel model oorskat die vertoning van die SGEO tydens golf hoogtes groter as 3m; die oorskatting is skynbaar die gevolg van onakkurate beramings van bygevoegde massa en demping. Die resultate van die BVD analise bevestig die turbine aannames by ontwerpstandighede. Die konstante-spoed turbine-ontwerp benadering om die gebruik van duur veranderlike spoed kragopwekkers teen te werk is oneffektief weg van ontwerp toestande, met staking in die rotor lemry by golfhoogtes bo 3m en swak turbine vertoning vir golfhoogtes van 1.5m en minder. Veranderlike spoed turbinewerking is ondersoek en het werking weg van die ontwerp punt verbeter.

Acknowledgements

My thanks and appreciations to the following people:

To my supervisors Proff. von Backström and van Niekerk, and Mr Deon Retief for their continual support and guidance throughout the duration of my project, it has been and an honour and a privilege to be associated with them.

To thank James Joubert, Andrew Gill, Andrew de Wet, Dr. Tom Fluri and my office mates Warrick and Johan, for their support.

To Dr. Hildebrandt and the staff of NUMECA for there tireless help answering my questions regarding their software no matter how complex or trivial.

The Center for Renewable and Sustainable Energy Studies (CRSES) for financial support.

Lastly I would like to thank my family and friends for the love and support they provided.

Contents

Declaration	i
Abstract	ii
Uittreksel.....	iii
Acknowledgements.....	iv
Contents	v
List of Tables.....	ix
List of Figures	x
Nomenclature	xiii
1. Introduction	1
1.1. Water waves and renewable energy.....	1
1.2. Previous work.....	2
1.3. Objectives of this study.....	3
1.3. Approach to the study.....	4
1.4. Conclusion.....	4
2. Literature survey	5
2.1. Wave theory	5
2.1.1. Wave Theory and modelling	5
2.1.2. Wave power in a real wave climate.....	6
2.2. Origins of wave energy converters	7
2.2.1. Contemporary wave energy converters	7
2.2.2. Subsurface velocity and pressure distributions	9
2.3. Wave energy turbine design	9

2.4. Stellenbosch Wave Energy Converter	11
2.5. Conclusion.....	12
3. System layout and turbine module schematic design.....	13
3.1. Introduction.....	13
3.1.1. SWEC structure	14
3.2. SWEC detail layout.....	16
3.2.1. OWC Chamber layout.....	16
3.2.2. High and low pressure manifold layout	16
3.3.3. Turbine housing schematic	17
3.4. Conclusion.....	18
4. Air flow system modelling and simulation	19
4.1. Wave actuation force	20
4.1.1. Wave profile.....	20
4.1.2. Subsurface mechanisms.....	21
4.1.3. OWC dynamics added mass and damping	23
4.2. Air flow system	25
4.2.1. Losses	26
4.2.2. Turbine modelling.	29
4.3. Modelling Air flow	29
4.3.1. Closed chamber model.....	30
4.3.2. Single chamber exhausting through a turbine	31
4.3.3. Chamber exhausting to an auxiliary volume.....	31
4.3.4. Chamber exhausting through turbine to collecting chamber.....	31
4.3.5. Full single chambered model.	31
4.3.6. Full converter	32
4.4. Air flow system modelling results.....	35
4.4.1. Objectives.....	35
4.4.2. Sea state and sea environment	35
4.3.3. Results and discussions	37
4.4. Conclusion.....	43

5. Turbine design	44
5.1. 1D Preliminary aerodynamic design	44
5.1.1. Introduction to 1D design	44
5.1.2. Preliminary turbine sizing and performance	45
5.2. 2D design Flow vectors and angles	47
5.2.1. Turbine design input data	49
5.2.2. Flow angle program algorithm.....	50
5.2.3. Results	57
5.3. 3D turbine Design.....	58
5.3.1. Blade section design.....	58
5.3.2. Blade stacking law	59
5.3.3. Blade taper	61
5.3.4. Tip clearance	62
5.3.5. Blade spacing	62
5.3.5. 3D turbine assembly	62
5.4. Conclusion.....	63
6. Turbine numerical modelling.....	64
6.1. Introduction.....	65
6.2. Pre-processing	65
6.2.1. Blade passage.....	65
6.2.2. Diffuser	66
6.3. Numerical model.....	66
6.3.1. Flow configuration.....	66
6.3.2. Boundary conditions	66
6.3.3. Numerical model.....	67
6.4. Post processing (results)	67
6.4.1. Design condition	67
6.4.2. Off-design conditions	70
6.4.3. Diffuser performance	73
6.4.4. Conversion efficiency.....	73
6.5. Conclusion.....	74

7. Conclusions and recommendations	75
7.1. Air flow system conclusions	75
7.1.1. Sub-conclusions	75
7.2. Turbine design conclusions	75
7.2.1. Sub-conclusions	76
7.3. Air flow system recommendations	76
7.3.1. Sub-recommendations.....	76
7.4. Turbine design recommendations.....	76
7.4.1. Sub-recommendations.....	77
8. References.....	78
Appendix A: SWEC dimensional discrepancies.	86
Appendix B: Derivation of SWEC state equations.	92
Appendix C: Simulink modelling process.	102
Attached CD	
Wave energy and power	
Verification SWEC numerical model	
2D sample calculation	

List of Tables

Table 1: Water depth classification (Coastal, 2006)	21
Table 2: SWEC design conditions (in bold) and variations used for sensitivity analysis.	35
Table 3: Summary of design options plotted in Figure 47.....	46
Table 4: Boundary conditions for design condition (2m Hs).	66

List of Figures

Figure 1: The distribution of annual wave power in kW/m wave crest (Thorpe, 1999)....	2
Figure 2: Artists impression of SWEC in operation (Retief, 2006).....	3
Figure 3: Cnoidal wave shape.	6
Figure 4: Classification with respect to wave front and shore line (Falnes, 2005).	7
Figure 5: Pelamis, surface motion.	8
Figure 6: Dam Atoll, overtopping.	8
Figure 7: OWC, pressure fluctuation.	8
Figure 8: Submerged buoys.	8
Figure 9: Subsurface water particle displacements (Coastal, 2006).	9
Figure 10: Wells turbine (Raghunathan, 1982).	10
Figure 11: Impulse blade row layout.	10
Figure 12: SWEC layout, with the “V” pointing toward the coast, (Autodesk, 2009).	11
Figure 13: Operating principal of the SWEC HP and LP phases (Retief, 2006).	12
Figure 14: Project component diagram (Retief, 1982).	13
Figure 15: SWEC air flow system and turbine inlet and outlet (diffuser) ducting.	14
Figure 16: Flow vortices deflecting flow in the original design and "curved" inlet design.	14
Figure 17: Turbine layout concepts from left, horizontal, tandem and vertical turbines.	15
Figure 18: Cross-section through an OWC chamber and Module of four chambers. ...	16
Figure 19: HP and LP manifolds shown in the modules and turbine base module.....	17
Figure 20: Final turbine module concept and transparent view showing ducting.....	17
Figure 21: Effect of surface waves on the systems that drive SWEC and SWEC itself.	19
Figure 22: Wave profile definitions and subsurface particle dynamics (Coastal, 2006).	20
Figure 23: Subsurface pressure and velocity fluctuations.	22
Figure 24: Representations of added mass on ships hull (Smith, 2003) and the OWC.	23
Figure 25: SWEC airflow system, turbine situated between HP and LP manifolds.....	25
Figure 26: Loss factor for elbows or bends (Idelchick, 1986).	27
Figure 27: Expansion and contraction loss factors (Idelchick, 1986).....	27

Figure 28: Moody diagram (Ingram, 2009).	28
Figure 29: Flap valve loss factor (Idelchick, 1986).	28
Figure 30: Merging, diverging and plenum chamber flow loss factors (Idelchick, 1986).	29
Figure 31: Modelling of a simple "piston" chamber to a full single chambered SWEC.	30
Figure 32: Added mass and added damping sensitivity analysis.	32
Figure 33: Added mass and added damping investigations.	33
Figure 34: Turbine flow rate, output power, pressure signals and pressure ratio.	34
Figure 35: Wave height occurrence and SWEC power curve.	36
Figure 36: NCEP wave directional rose for the SW South African coast (Joubert, 2008).	37
Figure 37: Subsurface pressure and OWC motion.	38
Figure 38: OWC chamber pressure and the effect of OWCs on manifold pressures.	38
Figure 39: Turbine generated and OWC input power and Mass flow.	39
Figure 40: Scale model and numerical model results and the SWEC energy budget.	39
Figure 41: Water depth model sensitivity and subsurface pressure fluctuations.	41
Figure 42: Model sensitivity to submergence and pressure fluctuations.	41
Figure 43: Model sensitivity to wave approach angle.	42
Figure 44: Model sensitivity to wave period and length.	42
Figure 45: Current model and revised arm length model mass flow.	43
Figure 46: Dimensionless speed and diameter chart (Balje,1981).	45
Figure 47: Blade loading vs. flow coefficient (Gannon, 2002).	46
Figure 48: Effect of vortex type on hub reaction, 50% reaction stage (Aungier, 2006).	48
Figure 49: Flow velocity triangle convention (Cohen, 2001).	49
Figure 50: Design program flow with respect to chord and blade number selection.	49
Figure 51: Pressure distribution around a turbine cascade blade (Dixon, 1998).	52
Figure 52: Soderburg loss coefficient vs. fluid deflection (Dixon, 1998).	52
Figure 53: Conical diffuser geometry (Dixon, 1998).	53
Figure 54: Flow regime chart for two dimensional diffusers (Sovran 1967).	55
Figure 55: Model sensitivity to diffuser inlet blockage.	56
Figure 56: Effect of inlet boundary layer blockage on performance (Sovran, 1967).	56
Figure 57: Flow angles and Reaction ratio.	57
Figure 58: Turbine solidity and chord.	58
Figure 59: Stream lines over blade profiles illustrating correct profile design.	59

Figure 60: IGV inlet and outlet flow vectors at hub, quarter, half, three quarter and tip profiles and profile stacking.....	60
Figure 61: Rotor inlet and outlet flow vectors at hub, quarter, half, three quarter and tip profiles and profile stacking.....	61
Figure 62: Spherical hub, shroud and diffuser, flow enters from the left though IGV....	63
Figure 63: Computational domain (turbine layout).....	64
Figure 64: Meshing scheme of blade rows (Fluri, 2008) and of a sector of the diffuser.	65
Figure 65: Multi grid functionality from fine (0 0 0) to course (2 2 2).	67
Figure 66: Turbine inlet flow magnitude.....	68
Figure 67: Rotor inlet flow velocity magnitude.	68
Figure 68: Turbine outlet flow velocity magnitude.....	69
Figure 69: Turbine flow angles for station 2 and 3.	69
Figure 70: Turbine efficiency and power output.	70
Figure 71: Turbine pressure drop and flow rate.	71
Figure 72: Profile section stream lines (95, 50 and 5% span, top to bottom), for 1, 2 and 4m Hs (left to right).	72
Figure 73: Meridian stream line plots for 1m, 2m, and 4m Hs conditions.....	72
Figure 74: Static pressure recovery through the diffuser.....	73
Figure 75: Predicted SWEC conversion efficiency.....	74
Figure 76: Turbine constant and variable speed performance variation.	74

Nomenclature

Symbols:

a	Wave amplitude (half wave height) (m)
AR	Area ratio
A	Cross-sectional Area (m ²)
b	Blade axial chord (m)
B	Blockage
Br	Breath (m)
c	Chord (m)
C	Actual flow vector velocity (m/s)
C _g	Wave group velocity (m/s)
C _w	Phase velocity of wave celerity L_w/τ (m/s)
C _o	Sprouting velocity $2g\sqrt{H_{ad}}$ (m/s)
C _p	Coefficient of static pressure recovery
C _p	Specific heat at constant pressure (J/kgK)
C _v	Specific heat at constant volume (J/kgK)
d	Water depth measured from SWL (m)
D	Diameter (m)
Dh	Hydraulic diameter (m)
Dis	Distance (m)
E	Effective area fraction A/A_{eff}
En	Energy (J)
f	Wall friction loss factor
F	Force (N)
g	Gravitational acceleration (m/s ²)
Hs	Significant wave height (m)
H	Height (m)
H _{ad}	Adiabatic head (m)

h	Enthalpy (J/kg)
l	Pipe flow loss coefficient (J/kgK)
k_t	Turbine constant
k	Wave number $2\pi/L_w$ (1/m)
K	Coefficient of performance or specific pipe flow loss coefficient (J/kgK)
L	Length (m)
m	Mass (kg)
\dot{m}	Mass flow (kg/s)
Ma	Added mass (kg)
n	Wave surface profile parameter(m)
N	Number
Ns	Turbine rotational speed (rpm)
Per	Perimeter (m)
P	Power (W)
p	Pressure or subsurface pressure (Pa)
Q	Heat (J)
\dot{Q}_t	Flow rate through turbine (m^3/s)
R	Gas constant for air (J/kgK)
r	Radius (m)
s	Blade pitch (m)
sc	Space to chord ratio
T	Temperature (K)
t	Time (s)
U	Turbine rotor circumferential speed (m/s)
u	Specific internal energy (J/kg)
u	Horizontal (x) velocity component (m/s)
\forall	Volume (m^3)
V	Velocity or in the turbine design case relative flow velocity (m/s)

w	Vertical (z) velocity component (m/s)
W	Work (J)
x	Horizontal distance or wave phase shift distance (m)
y	y-Direction in accordance with right hand coordinate system (m)
Y	Blade loading coefficient (kg/s ²)
z	Vertical distance or Vertical distance measured from SWL (m)

Greek Symbols:

Λ	Reaction ratio
α	Flow angle of actual flow velocity vector (rad)
β	Flow angle of relative flow velocity vector (rad)
Δ	Finite difference
δ	Diffuser divergence angle (rad)
ε	Deflection (rad)
ε_D	Diffuser effectiveness
Φ	Collector arm angle to oncoming waves
φ	Flow coefficient
η	Efficiency
κ	Wave Spectra constant
γ	Ratio of specific heats
λ	Hub to tip ratio
μ	Dynamic viscosity (kg/ms)
ν	Kinematic viscosity (m ² /s)
θ	Wave phase angel $\omega t - kx$ (rad)
ϑ	Overall diffuser effectiveness
ρ	Density (kg/m ³)
ζ	Loss coefficient
τ	Wave Period (s)
ω	Wave (radial) frequency $2\pi/\tau$ (rad/s)

ξ	Soderburg primary loss factor
ξ'	Soderburg secondary loss factor
Ψ	Zwiefel space chord ratio
Ψ	Load coefficient
ζ	Stagger angle (rad)

Subscripts:

a	Atmospheric air properties or relating to axial velocity components
B	Body
b	Blade
corr	Correction
C	Contraction losses
ch	Chamber
cho	Chamber opening
D	Diffuser
d	Downstream
E	Expansion losses
f	Wall friction
F	Frontal
eff	Effective
H	High pressure or hub
h	Hydraulic equivalent
id	Ideal
i	Control volume inlet or individual wave
k	Kinetic
L	Low pressure
m	Mean
man	Manifold
mod	Module

mer	Meridional
o	Control volume outlet
p	Potential
r	Radial
ra	Ratio
R	Rotor
S	Stator or IGV
sec	Secondary
s	Static quantity
sh	Shore
sub	Submergence
T	Tip or total flow conditions (pressure, temperature)
t	Turbine or tangential
tt	Total to total
u	Upstream
v	Vapour
W	Wave properties
w	Water piston control volume or water properties
x	X direction
y	Y direction
z	Z direction
1	Control volume 1 (CV 1), integration boundary or station number
2	Control volume 2 (CV 2), integration boundary or station number
3	Control volume 3 (CV 3) or station number
4	Control volume 4 (CV 4) or diffuser outlet flow
5	Control volume 5 (CV 5) or diffuser outlet flow
0	Total conditions
θ	Tangential direction

Superscripts:

–	Average value
\dot{m}	First derivative with respect to time
\ddot{m}	Second derivative with respect to time

Acronyms:

JONSWAP	Joint North Sea Wave Project
AWS	Archimedes Wave Swing
NCEP	National Centres for Environmental Prediction
WEC	Wave Energy Converter
IGV	Inlet Guide vane
OWC	Oscillating Water Column
SWEC	Stellenbosch Wave Energy Converter
OERG	Ocean Energy Research Group
SWL	Still Water Level
OPEC	Organization of the Petroleum Exporting Countries
LP	Low Pressure
HP	High Pressure
1D	One Dimensional
2D	Two Dimensional
3D	Three Dimensional
FBD	Free Body Diagram
FNMB	Full Non – Matching Boundary
CV	Control Volume

Dimensionless numbers

n_s	Dimensionless speed
d_s	Dimensionless diameter
Re	Reynolds number

1. Introduction

This chapter describes the role of wave energy at a global renewable energy level and the reasons for the initiation of wave energy converter (WEC) design. Work done on the design of the Stellenbosch Wave Energy Converter (SWEC) is also introduced.

1.1. Water waves and renewable energy

Renewable energy technologies have become more attractive over the past few years, but further advancements are necessary to increase their effectiveness. According to recent estimates oil production will peak within the first 10 to 15 years of the 21st century and then decline rapidly (Campbell, 2005). It is imperative that as oil supply dries up alternative (renewable) sources of generating energy should become mature enough to take over energy production.

Ocean energy is a popular area of research in countries with long coastlines and feasible or significant tidal, current and wave resources. These three resources are the major manifestations of ocean energy. Both waves and ocean currents can be considered to be caused by the sun's heating of the earth's surface while tidal fluctuations are dependent on the orbits of the moon around the earth and the earth around the sun.

Wave energy can be considered a tertiary form of solar energy. The heating of the earth's surface results in the occurrence of high and low pressures areas. These pressure gradients cause wind, as winds blow over large bodies of water they impart some of their energy to the water resulting in waves. The size and frequency of waves depend on the length of time, wind speed and distance (known as the fetch) that the winds blow over the water surface. Long fetches tend to generate the most energetic wave climates. Consequently, coast lines with exposure to prevailing wind directions, and long fetches, tend to have the most energetic wave climates; e.g., the western coasts of the Americas, Europe, Southern Africa, Australia and New Zealand (Figure 1). Figure 1 shows that the best wave climates can be found within 30 to 60 degrees latitude where strong storms frequently occur. However, attractive wave climates are still found within ± 30 degrees latitude where regular trade winds (easterly surface winds found in the tropics near the equator) blow.

Wave energy is a viable energy option on the south and south western coastlines of South Africa because of the length of the country's coastline, the proximity of the national electrical grid to these areas, the power potentially available in the waves on this coastline (Figure 1) and the low variability in the wave climate.

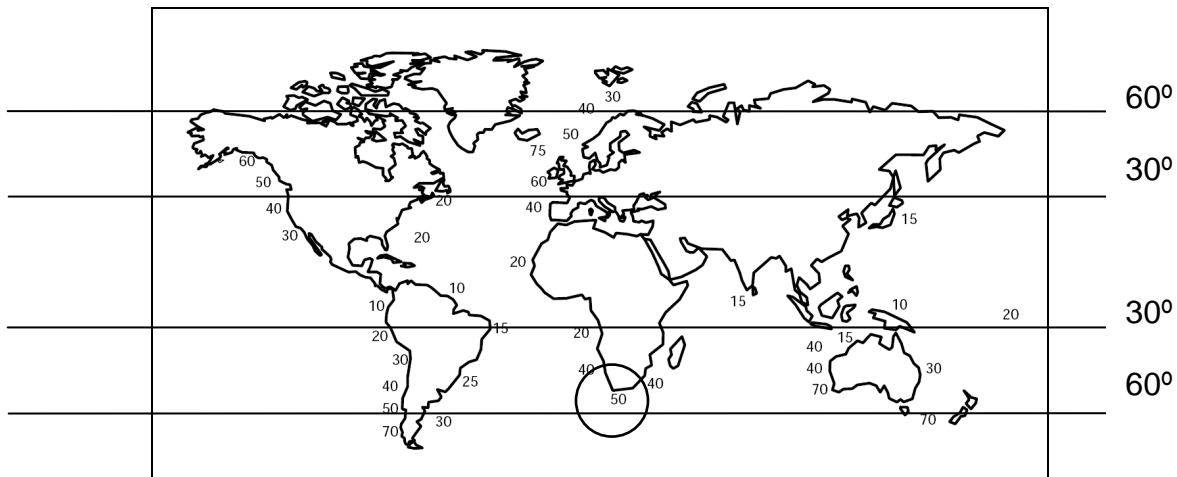


Figure 1: The distribution of annual wave power in kW/m wave crest (Thorpe, 1999).

1.2. Previous work

The Ocean Energy Research Group (OERG) was established in 1979 to research ocean energy conversion technologies. The formation of this research group was triggered by the increase in the oil price as a result of the implementation of oil limits by the Organization of the Petroleum Exporting Countries (OPEC). The OERG investigated the ocean energy resource along the South African coast (i.e., thermal gradients, current, wave and tide), concluding that wave energy is the most promising (Retief, 2006). A site on the west coast of South Africa, south of Saldahna was selected due to its regular wave climate, proximity to the national grid and national roads (Retief, 1984). The OERG then set about designing a Wave Energy Converter (WEC) especially suited to converting the inshore wave power at the proposed site and the SWEC was the result.

The SWEC (Figure 2) consist of two 160m long submerged arms arraigned in a “V” with an air turbine-generator unit situated at the apex. The arms consist of concrete modules housing Oscillating Water Column (OWC) units which feed high (HP) and low pressure (LP) manifolds, these manifolds run the length of the arms supplying and drawing air from a unidirectional turbine. The SWEC was designed to absorb only some of the

energy of a passing wave. The OWCs utilize subsurface pressure fluctuations to force air to flow through the system.

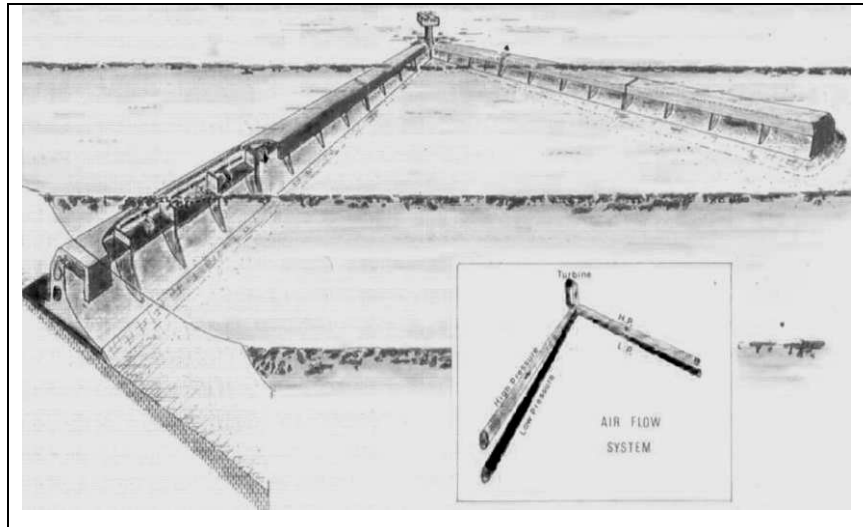


Figure 2: Artists impression of SWEC in operation (Retief, 2006).

The OERG halted work on the SWEC concept in the late 1980's due to the lowering of energy prices as a result of the reduction in the oil price. Up to that stage the work had concentrated on the SWEC structure, including sediment transport, forces and structural strength, cost, manufacture, installation and converter arm profile optimisation for absorption of the subsurface wave effects. Most of the work had been done using scale model studies in wave flumes and model basins.

1.3. Objectives of this study

Some of the work not undertaken before the initiation of this project, included numerical modelling and optimisation of the airflow system, design of the turbine ducting (inlet and diffuser), turbine design and testing of this design both numerically and experimentally.

The modelling of the airflow system and turbine design are the most important aspects of the work to be undertaken. The development of numerical models to describe system airflow and turbine performance will save cost and time in future investigations into the SWEC design. An initial turbine design is important as a “benchmark” on which future work can be based and compared.

The study was limited to the specification and design of a turbine and the numerical modelling of the turbine and the airflow system. A critical analysis of original design

documentation was done to determine the most current SWEC design. The objectives of the study are listed below:

- To complete a one dimensional (1D) numerically model of the SWEC airflow system. The model must be completed with the objective of being used as a structural optimisation tool where all structural and orientation aspects of the SWEC can be investigated.
- To investigate the dimensional requirements for the airflow system for a typical “V” converter unit with a rated output of 5MW. This entails searching the literature to determine the most adequate set of dimensions for the SWEC units. These dimensions are to be used to assemble the SWEC which is modelled.
- To design and model a full sized turbine to generate the required power at design conditions. The turbine design must be validated using the CFD package FINE/Turbo 8.4-3 of NUMECA (Fine, 2008). Turbine operation must be modelled at off design conditions to characterize operation due to variations in wave conditions.

1.3. Approach to the study

A study of the literature in which the SWEC design process was documented was undertaken. Similar turbine and WEC designs were investigated and discussed. An airflow system layout and turbine module schematic design was presented.

A 1D airflow system model was developed using Simulink (Mathworks, 2008) to numerically integrate the governing equations describing the states of the system. The results of this model are used as input to the turbine design process. Once a satisfactory turbine design was completed the design was validated and off-design operation characterised in a CFD study.

1.4. Conclusion

In conclusion the thesis has attempted to contribute to the completion of a concept developed over 30 years ago and possibly a new energy generating device specifically suited to South African conditions.

2. Literature survey

The literature survey is divided into sections dedicated to introducing wave theory, typical WEC design, theory behind the operation of the OWC WEC, WEC turbine design and finally the work already done by the OERG on the SWEC design.

2.1. Wave theory

This section is presented in two parts. The first describes wave theory, as to familiarize the reader with terms and theory behind the formation and modelling of sea states. Secondly the theoretical calculation of wave power in a random sea state is discussed.

2.1.1. Wave Theory and modelling

Knowledge of the forces which cause and propagate waves is essential when designing structures that are to survive in the ocean. Breakwaters, buoys, ships and WECs are but a few examples of such structures.

Surface waves are composed of two types of waves: seas and swells. Seas refer to short-period waves created “locally” by winds, over short fetches. Swells refer to waves that have moved from generating areas, over long fetches. Swells are generally more regular with well defined long crests (Coastal, 2006) and longer periods than seas. The sea surface is best described as being three dimensional (3D), irregular and unsteady, it is not yet possible to describe a sea state to its full complexity (both on the surface and subsurface) and therefore estimates and assumptions are required to analyse the effects of these waves.

The development of swells is not definite. The point when swells stop growing (theoretically) is termed a “fully” developed sea condition. From this point onwards, energy is dissipated mainly by the breaking of waves, to a lesser degree by internal dissipation, by interaction with the atmosphere, percolation and friction with the seabed. This is one attractive aspect of wave energy, in that a swell can travel vast distances without much loss of energy. Seas lose energy more readily than swells and as a consequence the periods of swells tend to be longer than seas. Swells typically have periods longer than 10 seconds.

This thesis is limited to the range of regular waves, in which we assume the sea state is two dimensional (2D), the waves are of sinusoidal shape, with small amplitude (with respect to length) and are progressive (in motion). These waves can be defined by wave height, period and length (Coastal, 2006). The wave dynamics (subsurface displacements, velocities, accelerations and pressures) are of importance in engineering design as they are the main determining factors in designing for survivability.

A simple wave form can be described by a sinusoid. A periodic wave is so termed if the form reoccurs over a certain time period (wave period). Waves are considered oscillatory if particle orbitals are circular in orbit (and of the same period as the wave).

The theory most widely used is the so called linear, or Airy wave theory (Airy, 1845), equivalent to first order Stokes (Stokes, 1847, 1880) wave theory (Coastal, 2006). This theory describes a sinusoidal wave, but according to Coastal (2006) most engineering problems can be approached with reasonable accuracy using this theory even if the waves (in reality) are not sinusoids (with the exception of breaking waves).

An example of non-sinusoidal waves, are when waves become large (in respect to water depth), troughs become shallower and flatter and the peaks become thinner and higher, they are termed cnoidal (Figure 3). Higher order Stokes theories can be used to approximate this effect.

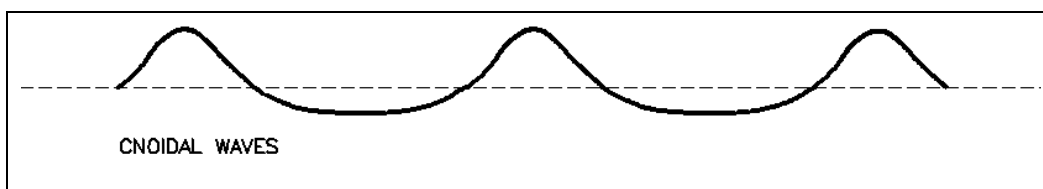


Figure 3: Cnoidal wave shape.

2.1.2. Wave power in a real wave climate

Irregular wave spectra are described by statistical wave spectrums, examples of which include Pierson–Moskovitz (Pierson, 1964) and JONSWAP (Hasselmann, 1973, 1976). Pierson–Moskovitz, one of the earliest developed spectrum, assumes that wind has blown over a large sea for a long time and those waves have come into equilibrium with wind (Pierson, 1976). The JONSWAP spectrum came about when Hasselmann (1973)

analyzed data collected during JONSWAP and found that a sea is never fully developed and that it is ever changing through wave to wave interactions. Equation 1 (Coastal, 2006) predicts the time averaged power per unit width of irregular wave spectra.

$$\overline{P_w} = \kappa H_w^2 \tau \quad \text{Equation 1}$$

Constant κ is dependent on an assumed standard wave spectrum, see Attached CD.

2.2. Origins of wave energy converters

Concentrated effort in research of WECs began in 1973 with the onset of the Arab-Israeli war when Arab nations began using oil as a means of applying pressure on the international supporters of Israel. These sanctions became the major driving force behind the need to develop alternative energy sources internationally.

The concept of producing useful energy or work from wave action predates sanctions with the first patent taken out in France in 1799 (Ross, 1995). Utilizing the effect of wave surface motion on a large buoyant object (a ship of the line as stated in the patent) to operate a lever with its fulcrum on the ship, used for lifting, pumping, milling etc.

2.2.1. Contemporary wave energy converters

Early WECs were usually designed to float and as a result classified by size, method of extracting energy and orientation with respect to wave front. A classification describing orientation with respect to the shore and the SWL is perhaps a more useful method as it better describes both floating and submerged WECs, Figure 4 (Cruz, 2008).

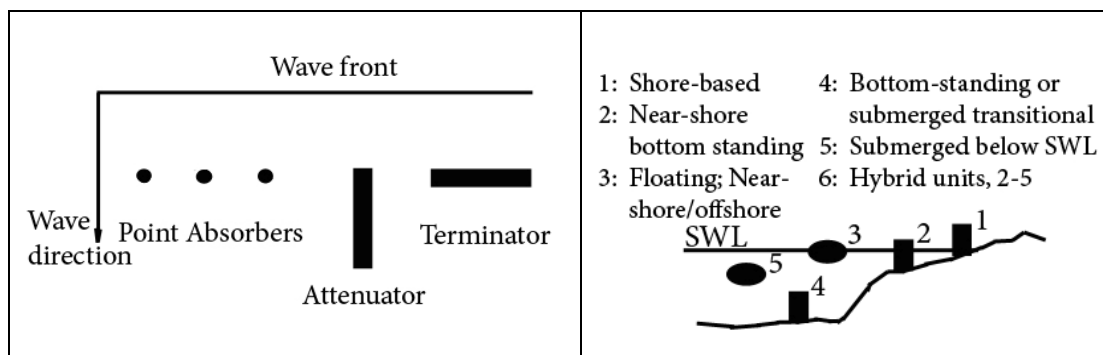


Figure 4: Classification with respect to wave front and shore line (Falnes, 2005).

This thesis, being a technical document, focuses on the operation of a WEC, it is intuitive therefore that discussions be focused on the methods used to extract energy. The three main mechanisms for extracting energy will be discussed in this section.



Figure 5: Pelamis, surface motion.

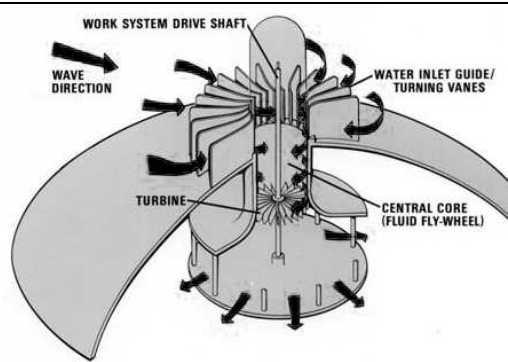


Figure 6: Dam Atoll, overtopping.

Wave surface motion is the most obvious mechanism used to extract energy (Figure 5). The WEC acts as a buoy, using the vertical motion of the sea surface to pump water or hydraulic fluid to drive linear motors, turbines etc. to generate energy. Over topping devices use the head created by a wave crest. This head crashes over the device and the water then moves through a turbine (Figure 6).

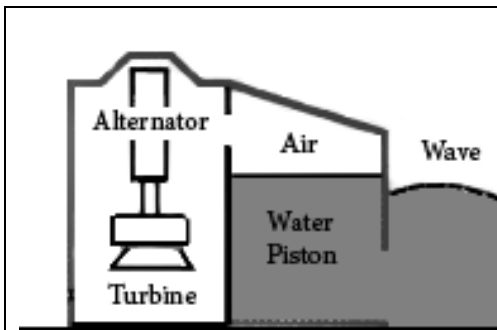


Figure 7: OWC, pressure fluctuation.

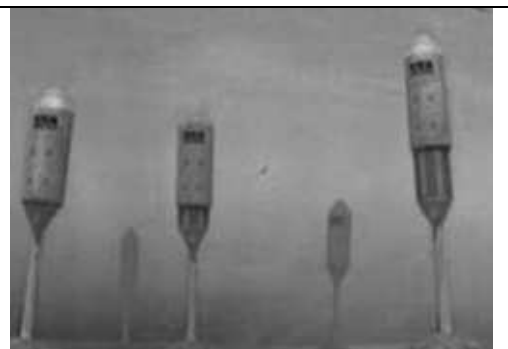


Figure 8: Submerged buoys.

Subsurface velocity and pressure fluctuations can be harnessed to generate energy by the OWC or submerged buoys, Figure 7 and Figure 8. Cruz (2008) gives extensive explanations to the operation of WEC devices and the advantages and challenges faced by each. The following paragraph describes the subsurface effects caused by surface waves and how these effects drive the SWEC.

2.2.2. Subsurface velocity and pressure distributions

Surface waves are associated with subsurface pressure fluctuations and water particle dynamics. Figure 9 shows the effect of the sea floor on particle orbitals; pressure undergoes a similar decay of fluctuations with increasing submergence. These subsurface effects force the OWC into motion which in turn pumps air through a bi-directional turbine, Figure 7.

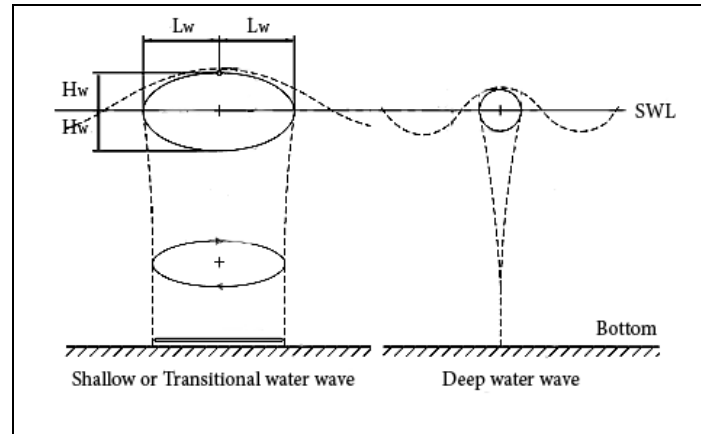


Figure 9: Subsurface water particle displacements (Coastal, 2006).

The most energetic portion of subsurface water is just below the SWL (Figure 9). Submerged WECs can be positioned to extract all (Figure 7) the energy from a wave or any fraction thereof by submerging the device at the required depth.

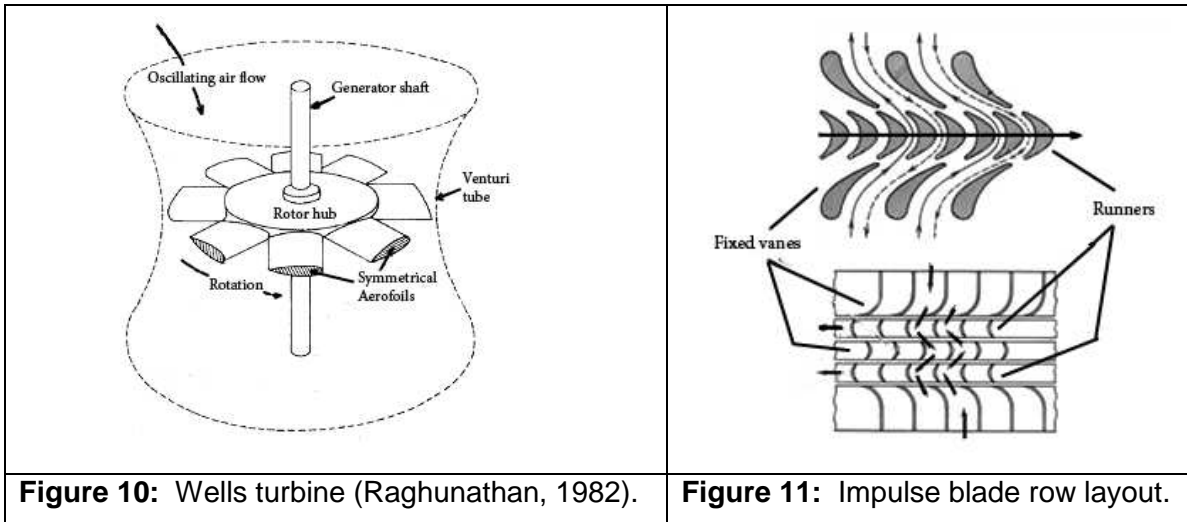
The traditional OWC device (Figure 7), situated on the shore, protruding from the SWL are of robust and simple design. The OWC is therefore ideally suited to generating energy from waves as its uncomplicated structure can be built to survive in the ocean.

2.3. Wave energy turbine design

Two classes of turbines typically used in wave energy conversion include the Wells turbine designed by Dr A. A. Wells (Raghunathan, 1982 and 1985) and the impulse turbine introduced by various authors (Kim, 1988 and Setoguchi, 2000). These turbines are mainly employed to extract energy from OWC devices.

An impulse turbine (Figure 11) is characterized by rotors that are symmetrical in the plain of rotation (equal inlet and outlet angles) and as a consequence there is no change

in pressure, no expansion and no change in flow velocity, and the work is done on the rotor only by turning the flow (Japikse, 1994).



The main characteristics of Wells turbines are that the rotor blade chord lines lie in the plane of turbine rotation, the flow through the turbine is bidirectional and that the turbine is not self starting. The rotor blades resemble a more classic aerofoil shape, often without IGVs (Inlet Guide Vanes), Figure 10.

The impulse turbine was originally designed to operate with self-pitch IGV control. IGVs moved in relation to wave frequency (Thakker, 2005). Setoguchi (2003) investigated the operation of a turbine with fixed guide vanes, as the pitching IGVs proved too costly in terms of maintenance, where the fixed IGV configuration was first reported in Maeda (1999). Thakker (2005) investigated the effect of 2D and 3D IGVs finding that 3D IGVs showed a marked improvement to overall efficiency (4.5% in the specific case investigated). Thakker (2005a) showed that down-stream guide vanes are less efficient than their upstream counterparts. He ascertained that there was an average of 21% pressure loss due to the down-stream guide vanes.

Bidirectional turbines tend to have lower efficiencies when compared to normal unidirectional flow turbines. Another issue regarding the performance of these turbines are the so called tip gap leakage losses; one of the most influential features that affect turbomachine design. Thakker (2005a) showed that tip gap losses can reduce the efficiency of the specific impulse turbine investigated by as much as 4%. Tagori (1987)

and Raghunathan (1995) found that Wells turbines are more sensitive to the tip gap effect than conventional turbines. He found that if the tip gap is decreased, stall is promoted, while cyclic efficiency is improved. It was also noted that a large tip clearance enabled the turbine to operate through a large range of flow rates before stalling.

2.4. Stellenbosch Wave Energy Converter

The SWEC was designed to attenuate power at wave heights approaching and exceeding 5m. This was done to ensure a minimal environmental footprint, to limit “spikes” in power production, damage to the SWEC structure and components and national grid.

WECs are typically designed for specific coastal regions; none besides SWEC are specifically suited to South African conditions. Research on the SWEC design done at the University of Stellenbosch (Retief, 1984) included model testing and theoretical modelling of SWEC arrays along proposed sites. The project did not move into the prototype building phase as a result of a lack of funding and political interest.

The SWEC is a near-shore WEC. With a collecting arm length of approximately 160m, each arm installed at a 45° angle (Appendix A) with respect to the predominant direction of energy flux (Retief, 1984). The SWEC systems (Retief, 1984) were envisaged to be deployed in arrays covering areas up to 39000m² (Figure 12) along a 40km stretch of coastline (Retief, 2008).

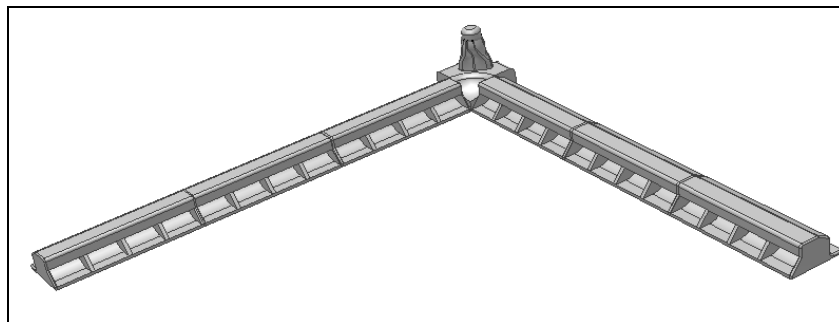


Figure 12: SWEC layout, with the “V” pointing toward the coast, (Autodesk, 2009).

The SWEC collecting arms (supported on the sea bed) are coupled in a “V” to a single air turbine (coupled to an electrical generator) mounted above water level in a tower at the apex of the “V” (Retief, 1984), Figure 12. Each collector arm consists of three

precast modules each containing four OWC chambers (Retief, 1984). In the OWC chambers, air is forced through rectifying valves into channels in the collecting arms and through a power generating unit in the tower.

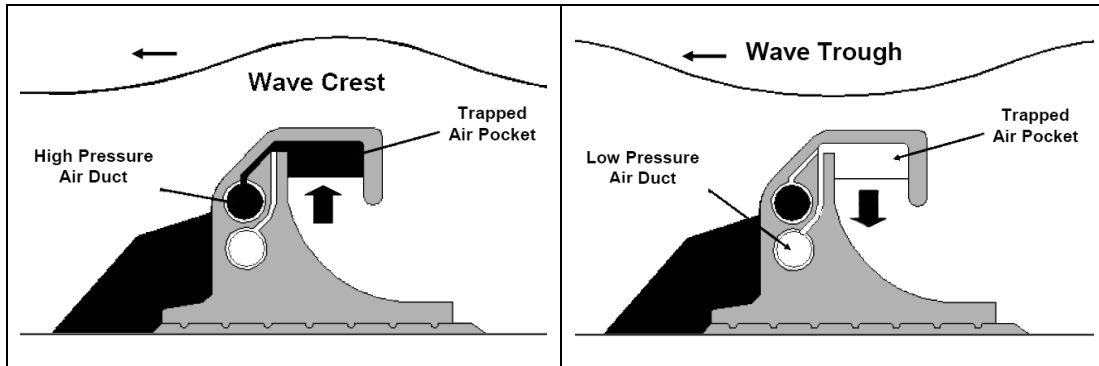


Figure 13: Operating principal of the SWEC HP and LP phases (Retief, 2006).

What makes SWEC a more viable option than traditional OWC devices is that it makes use of a unidirectional turbine which generally offers higher efficiencies than Wells or Impulse turbines. Not only are unidirectional turbines more efficient but the ability to include a diffuser in the design increases the pressure recovery. The major disadvantage of this concept is system maintenance as the device arms are totally submerged.

System submergence enables the SWEC to remove a fraction of the energy from a passing wave not inhibiting sediment transport to a great degree. A sediment transport study on a 1:60 3D model showed the seaward shift of the beach would stabilize within 10 and 20m (Retief, 1984). The device was designed to extract 30% of the energy from a passing wave (Retief, 2008) lowering the environmental impact. Retief (1984) saw North and South Bays south of Saldanha as the best location for the WEC with mean annual wave power of $\pm 30\text{kW/m}$. Each unit designed to deliver a rated power level of 5MW at the site (Retief, 1984).

2.5. Conclusion

The objectives of the literature survey were two-fold, firstly to give an overview of the environment in which SWEC operates and secondly to investigate the maturity of the SWEC technology.

3. System layout and turbine module schematic design

In this chapter the original design of the air flow system is discussed including OWC chambers, manifolds and ducting. A schematic design for the turbine module ducting is presented.

3.1. Introduction

The main objectives of the preliminary design of the air flow system were to minimize pressure losses (due to wall friction, pipe bending and flow diffusion) without the design becoming unreasonably large, impractical or complex and unserviceable.

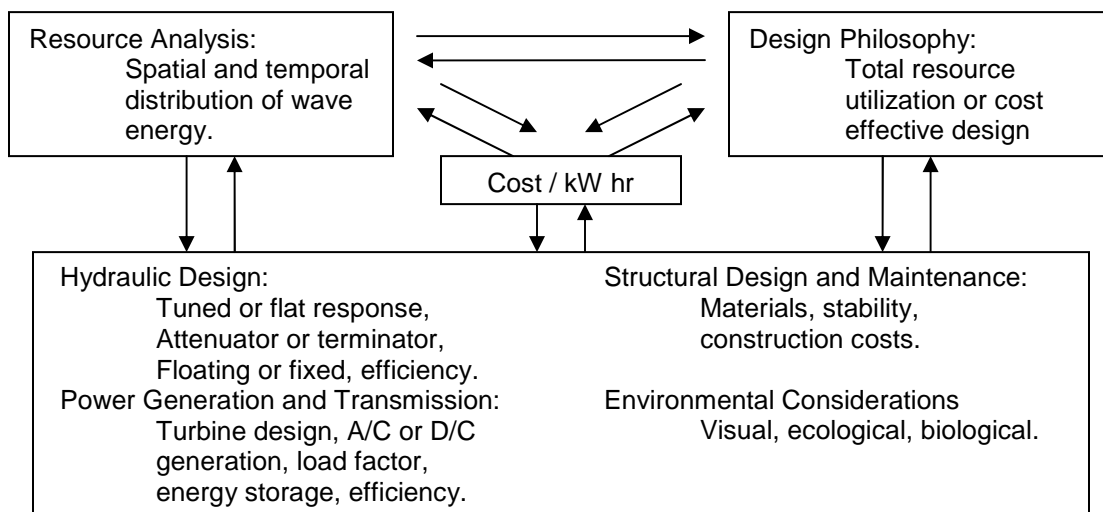


Figure 14: Project component diagram (Retief, 1982).

The SWEC structural design philosophy (Figure 14) was decided upon in the first round of design i.e., being designed for survivability in hostile sea conditions (Retief, 1982). The only undersigned sections include the turbine outlet (diffuser and diverging flow ducting into LP manifolds), turbine inlet (merging flow ducts into a plenum chamber and manipulation of HP manifolds) and valves (Figure 15). The scope of this project is such that the valve design is excluded and an idealized model assumed (Chapter 4).

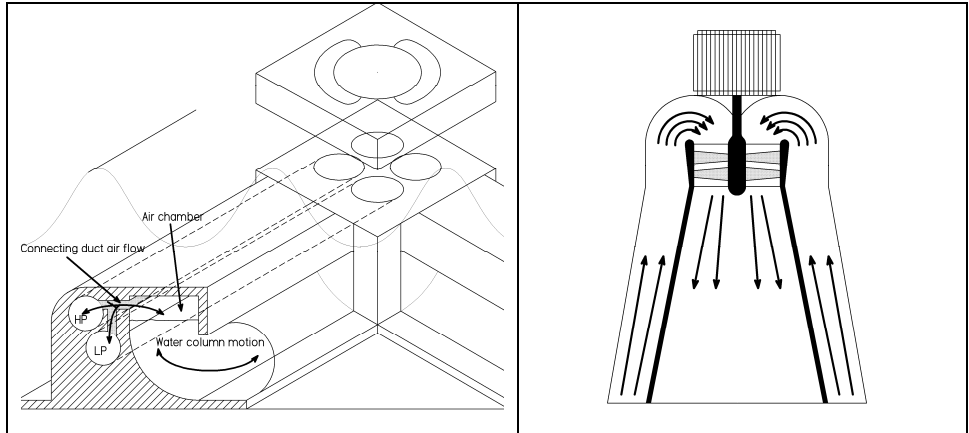


Figure 15: SWEC air flow system and turbine inlet and outlet (diffuser) ducting.

Although the original design process was well documented there are various discrepancies with regard to the dimensioning of the SWEC structure, Appendix A outlines the decision making process in determining the final set of dimensions.

3.1.1. SWEC structure

This section introduces the three major structural components of SWEC, namely the OWC chamber, HP and LP manifolds and the turbine housing.

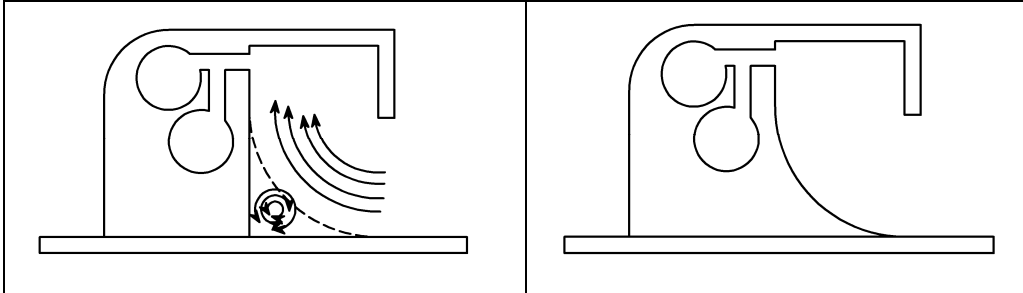


Figure 16: Flow vortices deflecting flow in the original design and "curved" inlet design.

The OWC chambers admit water flowing in and out of the OWC due to the forcing of fluctuating subsurface pressure. The chamber has a curved inlet as to facilitate the turning of inflowing water to the vertical (Figure 16). Scale model flume testing showed that both original and "curved" inlet design (chosen design) performed equally, Figure 16. Water moving into the originally designed chamber filled the chamber in such a way as to naturally deflect the motion of the OWC upwards (Retief, 2008). The curved inlet design added to overall weight and structural rigidity.

As the HP and LP ducts are the longest flow channels in SWEC, skin friction and pressure loss (as a result of flow junctions) are the most prominent mechanisms for loss. Methods to reduce losses are 1), increase duct cross sectional area lowering flow velocity and 2) lining ducts with smooth piping.

The turbine housing design was never attempted apart from a conceptual design suggesting the turbine be mounted horizontally, Retief (1984). In this paragraph the reader will be introduced to some of the layouts considered for the conceptual design, the final concept is refined later. Figure 15 alludes to the final concept. Concepts considered, (Figure 17) include horizontally and vertically mounted turbines, single turbines and turbines operating in tandem. In the following paragraphs three of the concepts are discussed, these concepts are chosen to highlight the various design alternatives considered. It is assumed that mounting a turbine/generator unit on shore as apposed to on the unit and piping air through the breaker zone is impractical. Reasons for this are that the survivability of any man made object in the surf zone is limited and additional losses system incurred as a result of the piping would make any associated gains negligible.

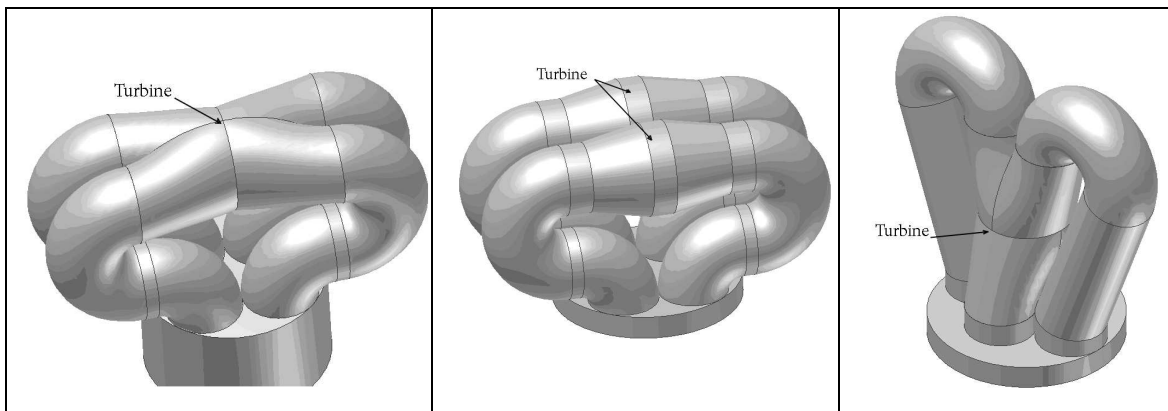


Figure 17: Turbine layout concepts from left, horizontal, tandem and vertical turbines.

The first concept shows a horizontally mounted turbine with ducts merging either side the machine, Figure 17. The resulting duct manipulation yield too little room for an inlet mixing chamber or a diffuser. The second concept is similar to the first except for the use of two turbines operating in tandem. The last concept is a turbine mounted vertically with the inlet ducts merging just above the turbine and outlet ducts forming a diffuser before separating.

3.2. SWEC detail layout

The final detailed layout of the SWEC system is presented in this section. It is important to note that only a schematic design of the turbine module and the duct manipulation to and from the turbine module is suggested.

3.2.1. OWC Chamber layout

The SWEC collector arms consist of three precast concrete modules each housing four OWC chambers (Figure 18). OWC chamber openings face the inside of the “V” allowing for energy reflected from opposing arms to be absorbed. The following paragraphs focus on the connecting duct design and valve positioning.

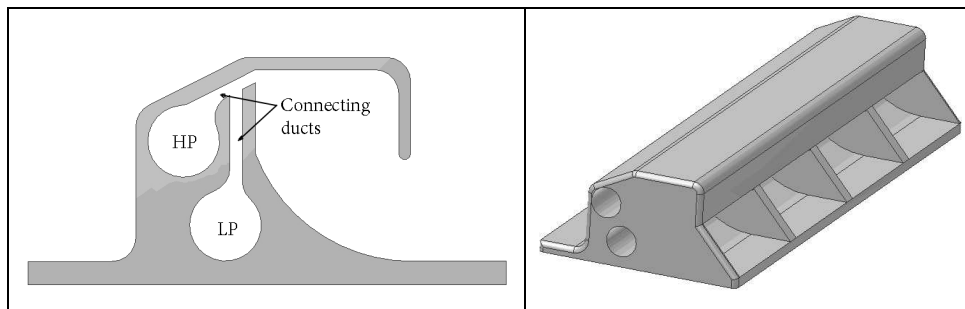


Figure 18: Cross-section through an OWC chamber and Module of four chambers.

Valves make the junction between connecting ducts (running the length of each chamber) and HP and LP manifolds. The duct opening in the OWC chamber is narrow in design, positioned against the roof of the OWC chamber and running the length of the chamber to ensure as large a possible cross-section with the aim of reducing losses. The juncture between connecting ducts and the HP and LP manifolds (Figure 18) is made gradual for the same reason.

3.2.2. High and low pressure manifold layout

The manifolds stretch along both collector arms and bend upward into the turbine housing (Figure 19). To reduce losses in the long straight sections the diameter is designed as large as possible without weakening the structural integrity or altering the shape of the modules (Appendix A). The manifolds will be lined with smooth PVC piping to reduce pipe wall friction and marine growth.

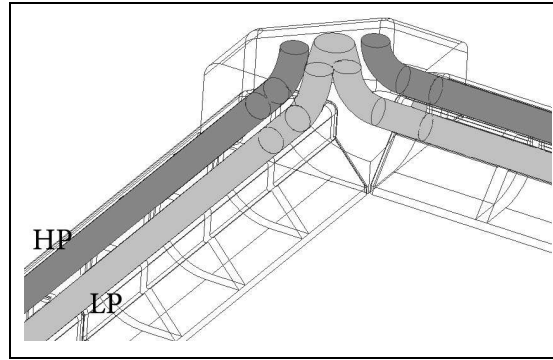


Figure 19: HP and LP manifolds shown in the modules and turbine base module.

The manifold bends are kept gradual to reduce losses (Idelchick 1986). The manifolds are aligned in the modules in such a way to ensure a generic module design of each arm (Figure 19).

3.3.3. Turbine housing schematic

The predominant governing factors in designing the layout of the turbine housing are to reduce the frontal area of the structure which faces oncoming waves (especially near the surface where wave action is greatest) and to manipulate flow to and from the turbine in an efficient manner. The eventual layout selected was a vertically mounted turbine (Figure 20). Inlet ducts wrap around the diffuser, narrowing toward the surface. A plenum chamber is used to merge the two HP duct flows, forming the inlet to the turbine.

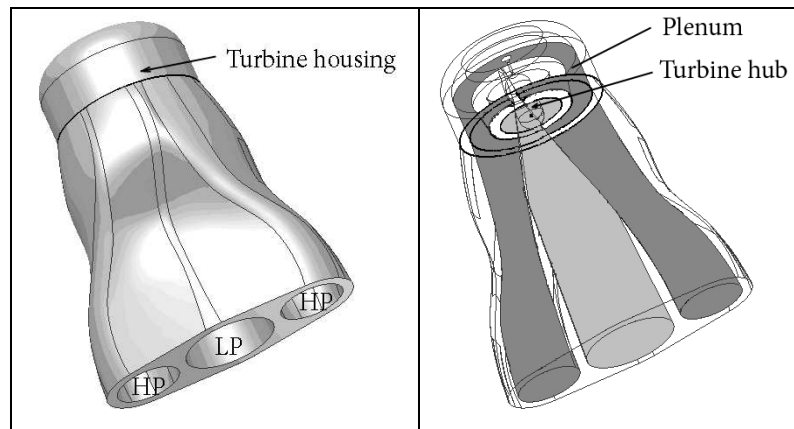


Figure 20: Final turbine module concept and transparent view showing ducting.

The module will be 12m high to ensure the turbine is situated above the SWL through all tide levels, to ensure ease of service and removal or replacement of the turbine and generator. The housing is divided into an inlet, outlet and turbine housing. The outlet

forms a diverging flow passage or diffuser. The turbine housing is designed to be removable for ease of maintenance, Figure 20.

The main concerns with this duct manipulation are to keep bends gradual and the cross sectional area constant, i.e., to not allow additional diffusion or contraction, hence accelerating or impeding of flow causing additional losses. The inlet duct shape is altered to wrap around the diffuser. The flows moving from the upward facing HP ducts are turned and combined in the plenum chamber before flowing through the turbine. To facilitate this turning the flow area is contracted slightly in the bend (Idelchick 1986).

The flow now moves into the diffuser in which the flow is slowed to achieve additional pressure recovery. Following the diffuser, flow is split into the two horizontal LP ducts supplying air to the OWC chambers. There is little scope for diffuser design, as the inlet and outlet dimensions are set by the turbine geometry and the existing LP duct design. For detailed diffuser analysis see chapter 5. Diffuser inlet area is equal to the turbine outlet area and the outlet area is equal to twice the LP manifold area: since the flow divides equally into the two LP manifolds.

Upon the commissioning of a SWEC unit air is pumped into the system through the turbine housing tower until the water in the OWC chambers is at the desired level. Control systems will be introduced to monitor the water levels in the individual OWC chambers during operation and if need be trigger the pumping of air into effected chambers. It is suggested that one pump is used to feed all OWC chambers and that the air flow is controlled by a series of valves.

3.4. Conclusion

As stated in Figure 14 and in the introductory paragraphs, the major concerns in the structural design are converter survivability in all sea states, hydrodynamic efficiency (efficient conversion of wave power into airflow), and an efficient airflow system (losses and service intervals to a minimum). All these are achieved through implementing a basic fluid flow design methodology. For instance cross-sectional areas remain constant except when the turning or diffusion of flow is taking place. Flow expansions and contractions are made gradual where possible. All design alterations are done without manipulating the overall SWEC shape.

4. Air flow system modelling and simulation

This section describes the simulation of the SWEC airflow system. Figure 21 describes in short how surface wave motion is linked to subsurface pressure and velocity fluctuations. The subsurface effects are the pumping forces which drive the turbine. A description of each of the five sections shown in Figure 21 is presented and the method to model it is explained. It is to be noted that the pressure definition used to calculate fluid properties is absolute.

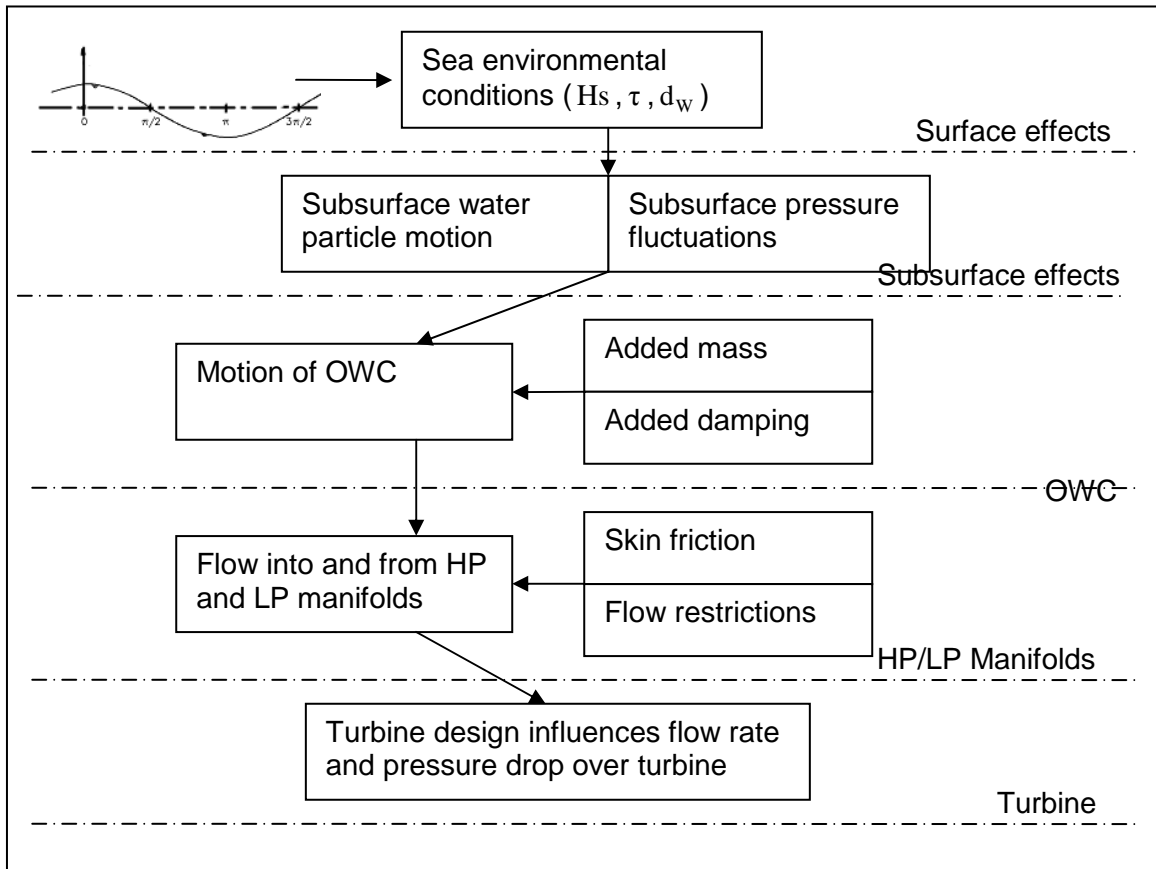


Figure 21: Effect of surface waves on the systems that drive SWEC and SWEC itself.

The work in this section is characterized by five distinct problems (Figure 21), i.e.; determining the driving force, calculation of added mass and added damping and the flow to and from the OWC chambers through one way valves into the HP and LP manifolds and through the turbine. What follows is a description of each of these problems and how these problems were overcome in the model.

4.1. Wave actuation force

Subsurface pressure fluctuations and water particle dynamics (to a lesser degree) drive the OWC. The OWC pumps air into and draws it from manifolds that feed a turbine. The potential and kinetic energy present in the sea surface brought about by the motion of waves about the SWL is the cause these subsurface mechanisms.

4.1.1. Wave profile

According to basic Airy wave theory a wave can be described as a sinusoidal (period, wave length and amplitude), Figure 22. The theory developed by Airy (1845) is easy to apply, giving reasonable approximations of wave characteristics for a wide range of parameters (Coastal, 2006). The more complete theoretical descriptions are modelled using a summation of successive approximations, each additional term in the series correcting preceding terms. Situations better described by these higher-order theories (Mei, 1991 and Dean, 1991) include breaking waves and wave action in shallow water.

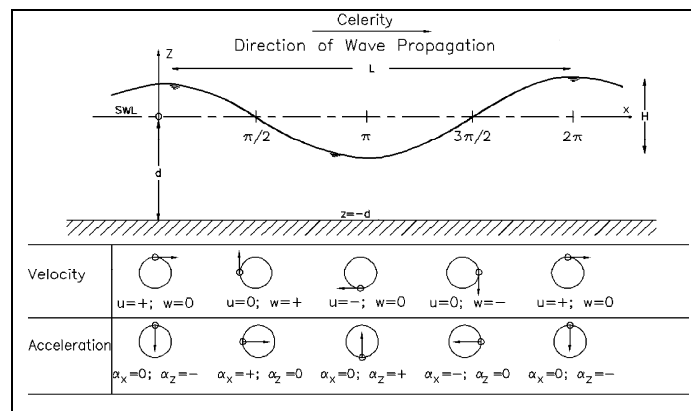


Figure 22: Wave profile definitions and subsurface particle dynamics (Coastal, 2006).

Assumptions made in developing the linear wave theory are:

- The fluid is homogeneous and incompressible.
- Surface tension is neglected.
- The Coriolis effect is neglected.
- The pressure on the free surface is uniform and constant.
- The fluid is ideal and inviscid.
- The waves being considered do not interact with any other water motions.
- The flow is irrotational (assuming shearing forces are negligible).

- The ocean floor is a horizontal, fixed, impermeable boundary implying vertical velocity components at floor level are zero.
- The wave amplitude is small and the waveform is constant through time and space.
- The waves are plane or long-crested or two dimensional (2D).

Equation 2 describes the surface wave profile and Equation 3 shows a relation between wave length and water depth for a given period. Since wave length is present on both sides of the equation successive substitution is used to solve for this parameter.

$$\eta_w = a \cos(kx - \omega t) = \frac{H_w}{2} \cos\left(\frac{2\pi x}{L_w} - \frac{2\pi t}{\tau}\right) = a \cos(\theta) \quad \text{Equation 2}$$

$$L_w = \frac{g\tau^2}{2\pi} \tanh\left(\frac{2\pi d}{L_w}\right) = \frac{g\tau}{\omega} \tanh(kd) \quad \text{Equation 3}$$

4.1.2. Subsurface mechanisms

Water depth can have a marked effect on wave profile and subsurface mechanisms, effecting the operation of the SWEC. Figure 9 shows the decay of particle orbitals in shallow and deep water. Shallow water orbitals take on an oblate form as water depth decreases. Table 1 presents the water depth classification given by Coastal (2006).

Table 1: Water depth classification (Coastal, 2006)

Classification	d/L	kd	$\tanh(kd)$
Deep	$1/2$ to ∞	π to ∞	≈ 1
Transitional	$1/20$ to $1/2$	$\pi/10$ to π	$\tanh(kd)$
Shallow	0 to $1/20$	0 to $\pi/10$	$\approx kd$

The SWEC is modelled in transitional water depth according to the above classification. Water depth ranges from 15 and 20m (Retief, 1984) with a predominant wave length of 148m (Equation 3).

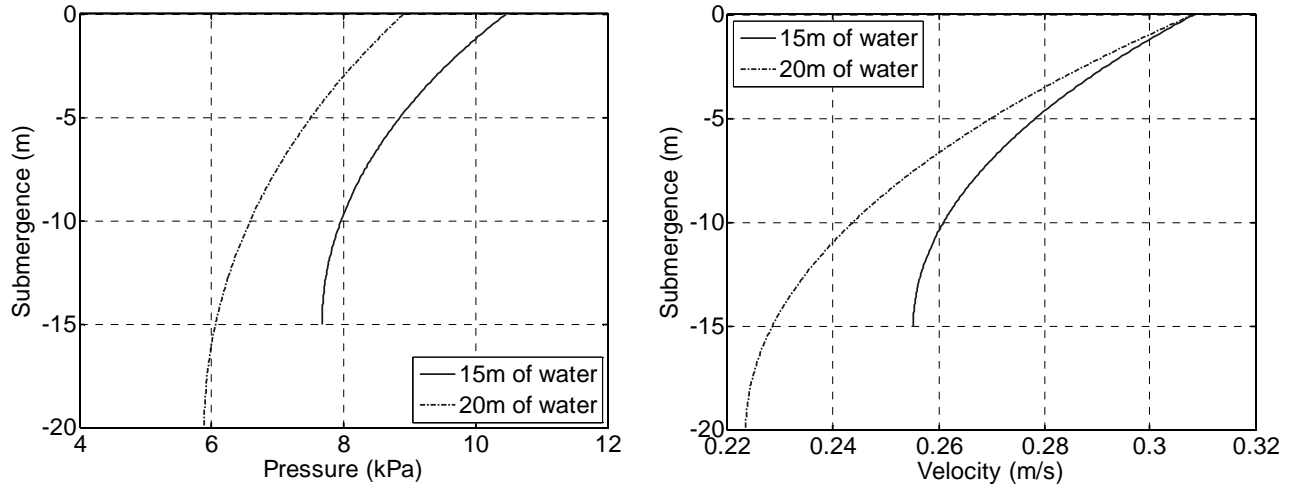


Figure 23: Subsurface pressure and velocity fluctuations.

Figure 23 shows the decay of velocity and pressure fluctuations with submergence in 15 and 20m water depth. Equation 4 describes the subsurface pressure using first order theory. Equation 5 and 6 define the horizontal and vertical particle velocity components, which add to the total pressure as “dynamic pressure” components (Coastal, 2006).

$$p_w = \frac{\rho_w g H \cosh\left[\frac{2\pi(z+d)}{L_w}\right]}{2 \cosh(2\pi d/L_w)} \cos(\theta) - \rho_w g z + p_a \quad \text{Equation 4}$$

$$u_w = \frac{g H T \cosh\left[\frac{2\pi(z+d)}{L_w}\right]}{2 L_w \cosh(2\pi d/L_w)} \cos(\theta) \quad \text{Equation 5}$$

$$w_w = \frac{g H T \sinh\left[\frac{2\pi(z+d)}{L_w}\right]}{2 L_w \cosh(2\pi d/L_w)} \sin(\theta) \quad \text{Equation 6}$$

A second order Stokes (Coastal, 2006) description of subsurface pressure (Equation 7) is used to provide a more accurate estimate of wave dynamics (Coastal, 2006).

$$p_w = \frac{\rho_w g H \cosh\left[\frac{2\pi(z+d)}{L_w}\right]}{2 \cosh(2\pi d/L_w)} \cos(\theta) - \rho_w g z + p_a + \frac{3 \rho_w g \pi H^2 \tanh(2\pi d/L_w)}{8 L_w \sinh^2(2\pi d/L_w)} \left(\frac{\cosh\left[\frac{4\pi(z+d)}{L_w}\right]}{\sinh^2(2\pi d/L_w)} - \frac{1}{3} \right) \cos(2\theta) - \frac{1 \rho_w g \pi H^2 \tanh(2\pi d/L_w)}{8 L_w \sinh^2(2\pi d/L_w)} \left(\cosh\left[\frac{4\pi(z+d)}{L_w}\right] - 1 \right) \quad \text{Equation 7}$$

The final two terms represent corrections made by the second order theory to the linear wave theory (Equation 7). The third and only steady term (apart from the atmospheric pressure term) corresponds to the correction for dynamic and kinematic components (Coastal, 2006). First order wave theories apply to waves symmetrical about the SWL

whose particle orbits are closed. Higher order theories apply to waves symmetrical about the vertical (Figure 3).

4.1.3. OWC dynamics added mass and damping

Traditionally, added mass and damping are associated with motion of ships, submarines and air ships through water and air respectively. Newman (1980) describes added mass as the effective mass of the fluid that surrounds the body and must be accelerated with it. The effect of these quantities only becomes apparent when the apparent density of the object moving through the fluid is comparable to that of the fluid. Added damping can be described as the effective damping resulting from the friction of the mass of fluid moving with the object through the surrounding fluid. This analogy can be extended to that of SWEC, the water column that surges up and down as a result of the wave action does not only accelerate the fluid in the column but also an undefined amount of fluid surrounding the opening of the chamber (Figure 24).

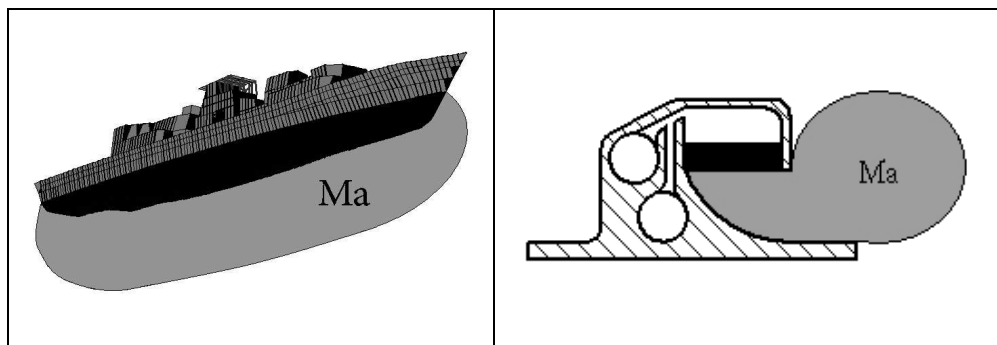


Figure 24: Representations of added mass on ships hull (Smith, 2003) and the OWC.

The added mass, damping and tuning of such OWC devices has been the subject of much study (Masami, 2005, Maeda, 1984 and 1984a, Malmo, 1985, 1986 and 1986a), with most of the studies being focused on the terminator type device. The devices are “tuned” to operate optimally (resonate) in certain predominant wave conditions. Storm conditions normally result in dangerous highly fluctuating airflows (in un-tuned devices) but in the tuned device the airflows would be damped out to tolerably safe levels. Masami, (2005) stated that this resonance occurs when the air chamber breadth is near to equal to multiples of the wave length. Although OWC seawater pumps use an alternative method of generating energy the main concepts still hold with that of the traditional OWC. Godoy-Diana (2007) states that the operation of such an OWC

seawater pump is greatly enhanced by maintaining the resonant condition with forcing wave frequency.

Most methods used to solve this problem include variations of the following. Maeda (1984) and Maeda (1984a) used a floating body approximation replacing the water column with a buoyant volume equal to that of the OWC volume. This method was proved valid for 2D problems when compared to a strict solution (Masuda, 1981). Evans (1978) simplifies the problem to a 2D water column surging between two thin vertical plates onto which waves impinge. A 3D problem is also solved by simplifying the problem to water surging through a vertically placed cylinder. In both cases the energy is extracted by using a float-spring-dashpot analogy. The free surface is replaced with a weightless piston assuming no spatial variation in the internal free surface.

Godoy-Diana (2007) took a method more closely resembling a dynamics problem by making the OWC seawater pump analogous to a spring mass damper system. Suzuki (2005) used the same floating body approximation as explained above as well as a method using air chamber flow rate and gauge pressure directly. System interaction is seen to be directly governed by flow rate through and pressure drop over the turbine. In recent years it has become increasingly viable to build large and complex numerical models using CFD to solve the problem where as before complex mathematical formulations were needed. Most of the methods discussed above assume linear surface wave theory and in all these cases reasonable results are achieved with both regular and irregular wave spectra (Kinoshita, 1985).

Many authors experimented with the addition of harbour walls, placing the OWC in a channel or in a reflecting wall to increase power output. Ambli (1982) showed that the addition of harbour walls to the front of an OWC structure ensures the device has a number of points of resonance within the OWCs incoming wave spectra hereby significantly increasing the OWCs energy production. Evans (1982) did work on the harbour concept presented by Ambli (1982) and came to similar conclusions as Ambli (1982) albeit with a much simplified numerical model. Count (1984) studied the effect of the addition of harbours using simple theory of long thin harbours and numerical methods used to describe the interaction of rigid bodies with waves. The results proved that the harbour concept was beneficial to energy production. Malmo (1985, 1986 and

1986a) researched the idea of the OWC positioned in a harbour, positioned in a reflecting wall with a harbour and a number of OWCs each with its own harbour all positioned in the same reflecting wall studying the influence of each OWC on surrounding devices.

The interest in the study of harbours and reflecting walls is of importance to the SWEC as the reflection of subsurface wave effects between arms may be present. It is assumed that the collector arms act as harbour walls which house OWC chambers.

4.2. Air flow system

The air flow, originating from the OWC chambers, forced through one way valves into a HP manifold, through a turbine, into the LP manifold and returning to OWC chambers through one way valves, (Figure 25) is modelled by solving the continuity (Equation 8), the momentum (Equation 9) and the energy equations (Equation 10). Assumptions were made to simplify the modelling process whilst not compromising the legitimacy of the solution.

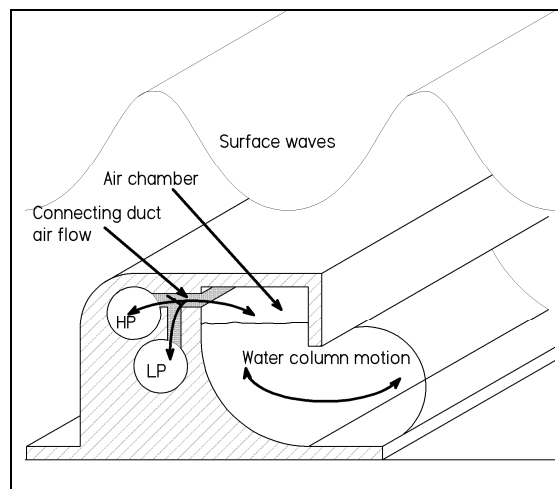


Figure 25: SWEC airflow system, turbine situated between HP and LP manifolds.

The continuity equation (Equation 8) is used to govern the conservation of mass ensuring mass flowing across boundaries remains in the system. The momentum equation (Equation 9) governs the dynamics of the OWC, balancing forces acting on the OWC boundaries and hydrostatic forces. The energy equation (Equation 10) governs temperature variation, flow velocity and losses throughout the air flow system.

$$\frac{d}{dt} \left(\int_{\forall} \rho d\forall \right) + \int_A \rho V dA = 0 \quad \text{Equation 8}$$

$$\sum F = \frac{d}{dt} \left(\int_{\forall} V \rho d\forall \right) + \int_A V \rho V dA \quad \text{Equation 9}$$

$$\frac{dQ}{dt} - \frac{dW_w}{dt} = \frac{d}{dt} \left[\int_{\forall} \left(\frac{V^2}{2} + gz + u_s \right) \rho d\forall \right] + \int_A \left(\frac{p}{\rho} + \frac{V^2}{2} + gz + u_s \right) \rho V dA \quad \text{Equation 10}$$

In this study however it is assumed that the system is isothermal and adiabatic. Equation 11, an adaptation of a relation governing the pressure in an adiabatic flow along a stream line (Crowe, 2001) shows that a 2% variation in temperature (due to the maximum pressure fluctuation resulting from a passing wave) can be expected. This variation is deemed negligible when regarding the size of the air flow system in relation to the turbine.

$$\frac{T_2}{T_1} = \left(\frac{p_2}{p_1} \frac{\rho_{01}}{\rho_{02}} \right)^{\gamma-1/\gamma} \quad \text{Equation 11}$$

The pipe flow equation used to govern flow through ducts is derived from the energy equation (Equation 13). The ideal gas law is assumed to be valid (Equation 12) and used to govern air pressure in each CV. Pressure is regulated by the influx or efflux of mass from a CV and volume change.

$$p_1 \forall_1 = m_1 R T_1 \quad \text{Equation 12}$$

4.2.1. Losses

The losses in the connecting ducts and in the HP and LP manifolds are introduced by implementing the pipe flow equation (Equation 13). The effect of losses is manifested in a reduction of total pressure. These losses include: pipe bends, expansion and contraction, pipe wall friction (so-called L/D losses), valves and merging and diverging duct flow. What follows is a description of how loss factors are determined for each flow regime.

$$p_1 + \frac{\rho_1 V_1^2}{2} + z_1 = p_o + \frac{\rho_o V_o^2}{2} + z_o + \rho_o g \sum h_L \quad \text{Equation 13}$$

Bends present in the air flow system include 90° bends where collector arms meet and where HP and LP duct flow moves into the turbine and out of the diffuser (Figure 26).

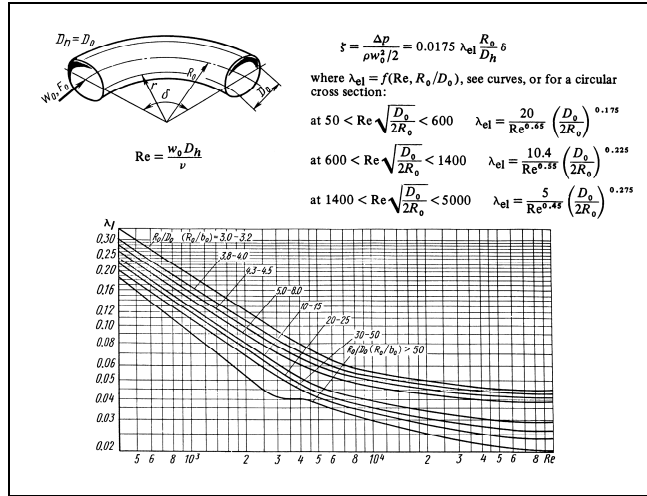


Figure 26: Loss factor for elbows or bends (Idelchick, 1986).

Contraction and expansion losses occur when flow moves to and from connecting ducts between the OWC chambers and HP and LP manifolds, (Figure 27).

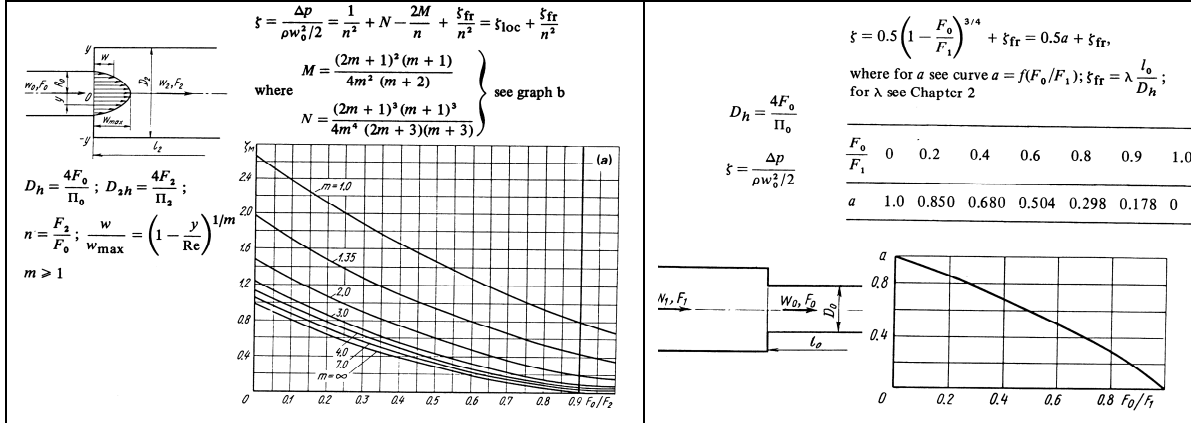


Figure 27: Expansion and contraction loss factors (Idelchick, 1986).

Wall friction losses are applicable to all flow through the system as the system is ducted. The major affected regime of flow being air moving in the HP and LP manifolds.

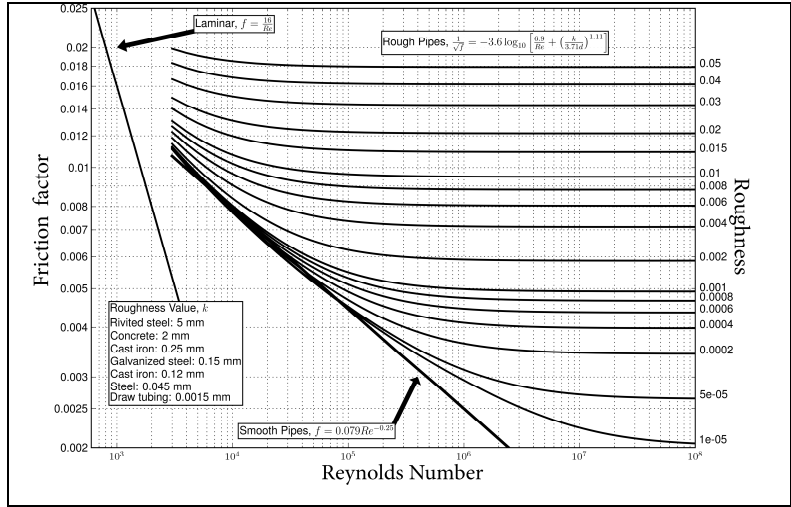


Figure 28: Moody diagram (Ingram, 2009).

The loss factor is relative to flow velocity, Equation 14 (Crowe, 2001) is used to approximate the factor.

$$f = \frac{0.25}{\left[\log_{10} \left(k_s / 3.7D + 5.74 / Re^{0.9} \right) \right]^2} \tag{Equation 14}$$

The valve losses are applicable to flow moving through top hinged flap valves used to regulate flow moving between OWC chambers, HP and LP manifolds are determined using Figure 29. As will be explained an initial pressure difference is assumed necessary to activate a valve following which a constant loss factor of 2.5 is assumed.

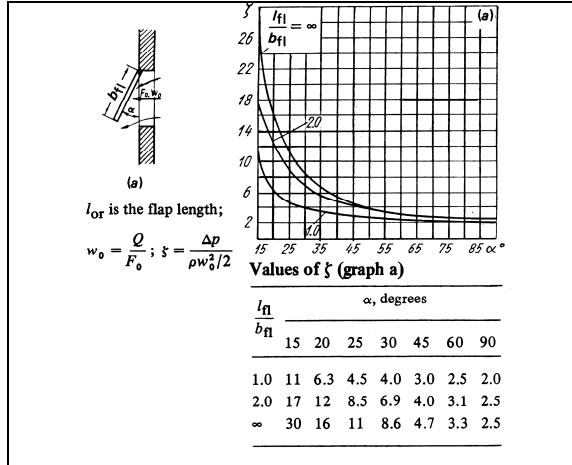


Figure 29: Flap valve loss factor (Idelchick, 1986).

The losses affecting merging flows occur at turbine inlet (plenum chamber). The flow diverges after the diffuser into the LP manifolds (Figure 30).

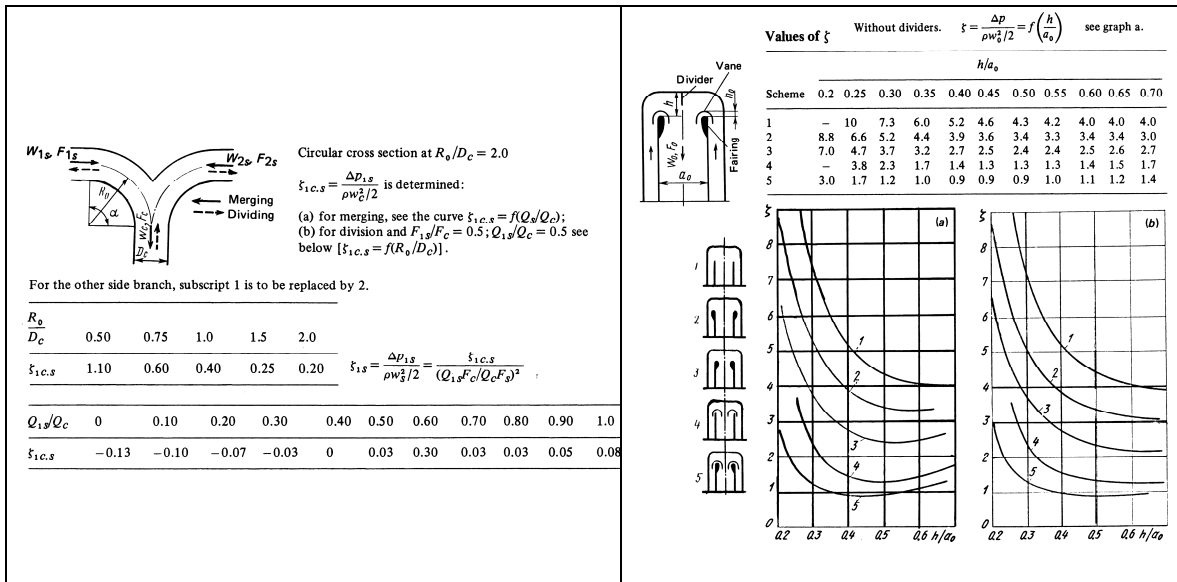


Figure 30: Merging, diverging and plenum chamber flow loss factors (Idelchick, 1986).

4.2.2. Turbine modelling.

The turbine governing Equation 15 (Fluri, 2008) expresses the relation between pressure ratio and mass flow through the turbine. The constant k_t governs this relation and hence determines the design of the turbine. See section 4.2.6 for determination of this constant.

$$\dot{m}_t = \frac{P_{Ti}}{\sqrt{T_{Ti}}} k_t \left[1 - (P_{To}/P_{Ti})^2 \right]^{1/2} \quad \text{Equation 15}$$

4.3. Modelling Air flow

The air flow system model is broken down into simple components (Figure 31). These components are assembled up to the point when the full converter is represented. The models will be explained in terms of operation, convention (direction of positive flow for example) and governing state equations. Full derivations of the relations are presented in Appendix B and for model validation see the attached CD. Simulink (Mathworks, 2008) is used to solve the differential equations describing the states of the systems. Simulink (2008) uses block diagrams to describe differential equations.

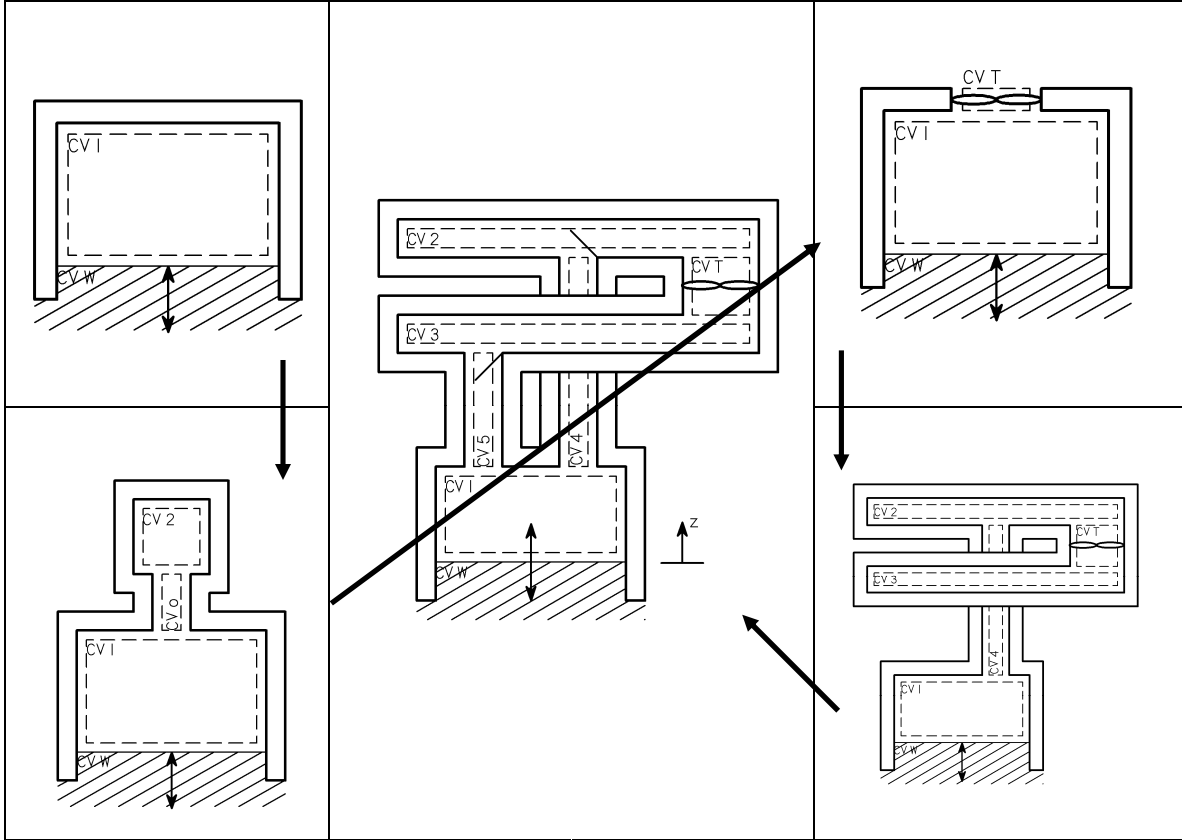


Figure 31: Modelling of a simple "piston" chamber to a full single chambered SWEC.

The block diagrams are presented in Appendix C whilst the state equations are shown here. As many of the state equations are defined the same as for the preceding modules some equations will not be repeated.

4.3.1. Closed chamber model

This model is used to ensure the subsurface pressure fluctuation is correctly applied (Equation 7).

$$\begin{aligned}
 \bar{p}_w = & \frac{1}{x_2 - x_1} \left[\rho_w g \frac{H}{2k} \frac{\cosh[2\pi(z+d)/L_w]}{\cosh(2\pi d/L_w)} \cos(kx - \omega t) - \rho_w g z x \right. \\
 & + \frac{3}{8} \rho_w g \frac{\pi H^2}{2k L_w} \frac{\tanh(2\pi d/L_w)}{\sinh^2(2\pi d/L_w)} \left[\frac{\cosh[4\pi(z+d)/L_w]}{\sinh^2(2\pi d/L_w)} - \frac{1}{3} \right] \cos(2kx - 2\omega t) \\
 & \left. - \frac{1}{8} \rho_w g \frac{\pi H^2}{L_w} \frac{\tanh(2\pi d/L_w)}{\sinh^2(2\pi d/L_w)} \left[\cosh \left[\frac{4\pi(z+d)}{L_w} \right] - 1 \right] x + p_a x \right]_{x_1}^{x_2}
 \end{aligned} \tag{Equation 16}$$

Equations 17, 18 and 19 represent the states of the system. Appendix C details correction of initial conditions.

$$\dot{p}_1 = \frac{p_1 \dot{z}}{(H_1 - z)} \quad \text{Equation 17}$$

$$\dot{z} = V \quad \text{Equation 18}$$

$$\dot{V} = \frac{1}{\rho_w z} \left[p_w - p_1 - \rho_w g z - \frac{4\mu_w (L_1 + B_1)}{A_1^2} \dot{z} \right] \quad \text{Equation 19}$$

4.3.2. Single chamber exhausting through a turbine

The turbine ellipse law equation is validated in this model (Equation 15). Mass is exchanged with the atmosphere and therefore it is important to ensure the conservation of this quantity, See attached CD. State equations include Equations 18, 19 and 20).

$$\dot{p}_1 = p_1 \left[\frac{\dot{z}}{(H_1 - z)} - \frac{\dot{m}_{t,i,o}}{m_1} \right] \quad \text{Equation 20}$$

4.3.3. Chamber exhausting to an auxiliary volume

The implementation of connecting duct losses is validated in this model. The pipe flow equation describes bidirectional mass flow and losses expedited by flow in both directions (Equation 21). The other state equations include Equation 18, 19, 20 and 22.

$$\dot{m}_{i,o} = \sqrt{\frac{2(p_1 - p_2)}{\rho_{i,o} \left[\frac{1}{A_{i,o} \rho_{i,o}} \right]^2 \left[1 + f L_{i,o} / D_{i,o} + K_C + K_E \right] - \rho_1 \left[\frac{1}{A_1 \rho_1} \right]^2}} \quad \text{Equation 21}$$

$$\dot{p}_2 = p_2 \left[\frac{\dot{m}_o}{m_2} \right] \quad \text{Equation 22}$$

4.3.4. Chamber exhausting through turbine to collecting chamber

This model is used as a step between the basic models and the final single chambered model. Mass is exchanged between all three volumes with mass passing through the connecting duct and a bidirectional turbine (Equation 15, 18, 19, 21, 20 and 23).

$$\dot{p}_2 = p_2 \left[\frac{(\dot{m}_o - \dot{m}_t)}{m_2} \right] \quad \text{Equation 23}$$

4.3.5. Full single chambered model.

This model is the single most complicated unit of the SWEC model. To assemble the full SWEC model it is necessary only to duplicate this model 24 times. The major complication of this model is the valve actuation methodology. Valve operation is actuated by positive pressure build up (Equation 25 and 26). An initial pressure build up

is assumed necessary to open the valve (of 100 Pa). Once the valve is open the loss coefficient is assumed, Figure 29. States of the model are Equation 15, 18, 19, 20, 23, 24, 25 and 26.

$$\dot{p}_3 = p_3 \left[\frac{(\dot{m}_{o,3} + \dot{m}_T)}{m_3} \right] \quad \text{Equation 24}$$

$$\dot{m}_{o,1} = \sqrt{\frac{2(p_1 - p_2)}{\rho_{i,o} \left[\frac{1}{A_{i,o}} \rho_{i,o} \right]^2 \left[1 + f \frac{L_{i,o}}{D_{i,o}} + K_C + K_E \right] - \rho_1 \left[\frac{1}{A_1 \rho_1} \right]^2}} \quad \text{Equation 25}$$

$$\dot{m}_{o,3} = \sqrt{\frac{2(p_3 - p_1)}{\rho_{i,o} \left[\frac{1}{A_{i,o}} \rho_{i,o} \right]^2 \left[1 + f \frac{L_{i,o}}{D_{i,o}} + K_C + K_E \right] - \rho_1 \left[\frac{1}{A_1 \rho_1} \right]^2}} \quad \text{Equation 26}$$

4.3.6. Full converter

As stated above, to assemble the full converter it is necessary to duplicate the previous models blocks 24 times in the correct sequence. It is necessary to specify a turbine constant (Equation 15) as it affects basic turbine operation and the initial inputs into the turbine design process. Added mass and damping affect the choice of the constant as well as having a direct influence on the dynamics of each OWC which determine operating conditions of the turbine (pressure drop and flow rate). The exact determination of these factors is beyond the scope of this study it was decided to conduct a sensitivity analysis to determine the effect of these quantities on the operation of SWEC and make an assumption as to the correct value of these constants. A turbine constant will be chosen to correspond to maximum power production at the design condition.

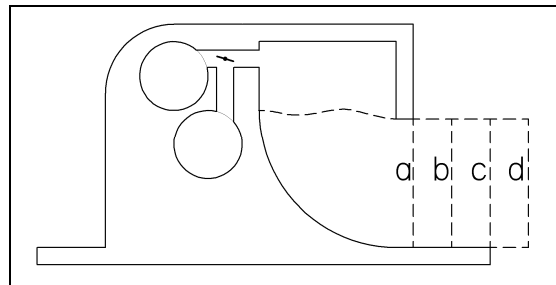


Figure 32: Added mass and added damping sensitivity analysis.

Figure 32 shows the mass added to the original (a) OWC, half the OWC volume (b), full volume (c) and one and a half the volume (d). The results of these analyses are presented in Figure 33. The added damping sensitivity is done in a similar manner.

The sensitivity analysis was concluded upon the model yielding results that resemble the originally experimentally determined values, for turbine flow rate and pressure drop of $250 \text{ m}^3/\text{s}$ and 7500 kPa respectively (Retief, 1984).

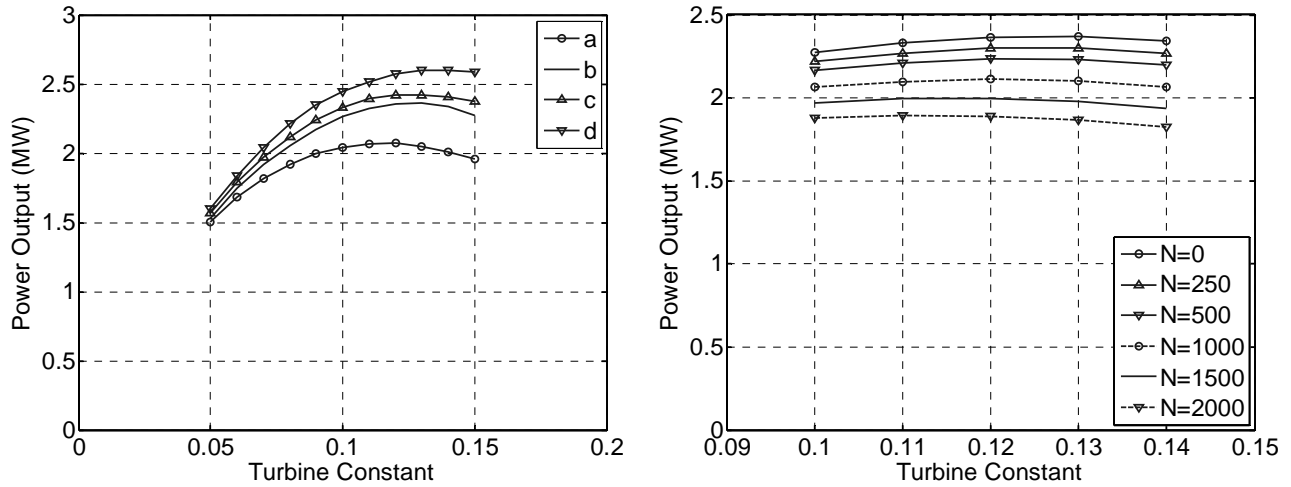


Figure 33: Added mass and added damping investigations.

Added mass and damping constants equivalent to the boundary marked b in Figure 32 and 1500 kg/s are assumed. These values are decided upon as the results do not show appreciable change over the range of the analysis (Figure 33).

The model results are presented for the design wave condition of 2 m Hs and 12.3 s period (Figure 34). Signals are “fairly” flat and periodical once fully developed. The “ripples” are believed to be a result of the collector arms being shorter than the projected wave length.

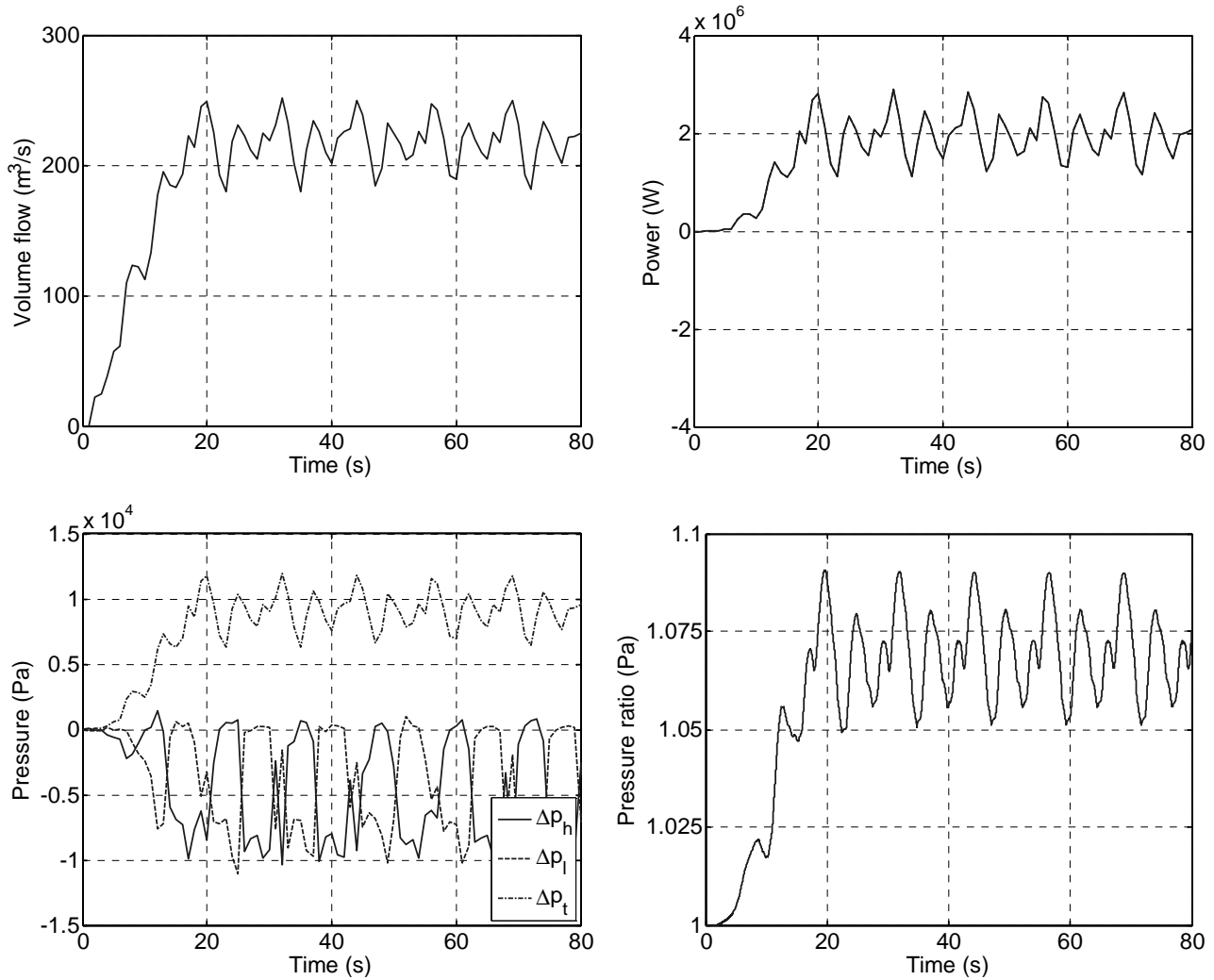


Figure 34: Turbine flow rate, output power, pressure signals and pressure ratio.

The negative portions of the signals in the pressure graph refer to the pressure forcing valves closed. The averages of the signals shown in Figure 34 are used as turbine design inputs (volume flow of 215m³/s and turbine pressure drop of 9200Pa). The flow variations (approximately 2 seconds from peak to trough) shown in Figure 34 are slow in comparison to the speed of the turbine (1500 rpm or 25 cycles per second, see chapter 5) therefore it is assumed that a steady state CFD modelling approach will be valid.

4.4. Air flow system modelling results

The results of the airflow system simulation are presented, discussed, problem boundaries are set and input values defined.

4.4.1. Objectives

The main objective of modelling the SWEC air flow system is to obtain inputs for the turbine design process. The model is used to establish the sensitivity of the SWEC to changes in water depth, submergence, wave height, approach angle, period and length.

4.4.2. Sea state and sea environment

The sea state and environment in which a SWEC converter is situated determines the effectiveness of the converter to absorb the energy of a passing wave. Table 2 shows the various conditions (sensitivity analysis) to which the SWEC model is exposed. Each of the variable conditions will be explained in the following paragraphs.

Table 2: SWEC design conditions (in bold) and variations used for sensitivity analysis.

Significant wave height	0.5, 1, 2 , 3, 4, 5 m
Water depth	15, 16, 17, 17.5 , 18, 19, 20 m
Submergence	2, 3, 4, 5, 5.5 , 6, 7 m
Wave approach angle	225, 230, 235, 240 , 245, 250, 255°
Wave Period	10, 11, 12, 12.3 , 13, 14 s
Wave length	115.6, 130.1, 144.4, 148.6 , 158.5, 172.4m

The significant wave height (H_s) is defined as the average height of the highest one-third of waves in a spectra this definition originated from oceanographer Walter Munk in an attempt to mathematically express wave height estimated by a “trained observer” (Kinsman 1965). This is the most widely used parameter describing wave height (Coastal, 2006). It is important to understand the statistical implications of this parameter, in that smaller and larger waves do exist in the same spectra (Equation 27).

$$H_s = \left(\frac{1}{N/3} \right) \sum_{i=1}^{N/3} H_i \quad \text{Equation 27}$$

Investigations into variations in wave condition and environment are important as such variations as shown in Table 2 would be experienced in the day to day operation of the

SWEC. The converter is designed to operate optimally under the most prevalent wave height condition (2m). The SWEC operation is characterised by a power curve being attenuated at around a wave height of 5m. This is to prevent damage to the system in extreme sea conditions and “spikes” in energy production (affecting the national grid). It is important that the SWEC be operational in calm and extreme wave conditions, Figure 35.

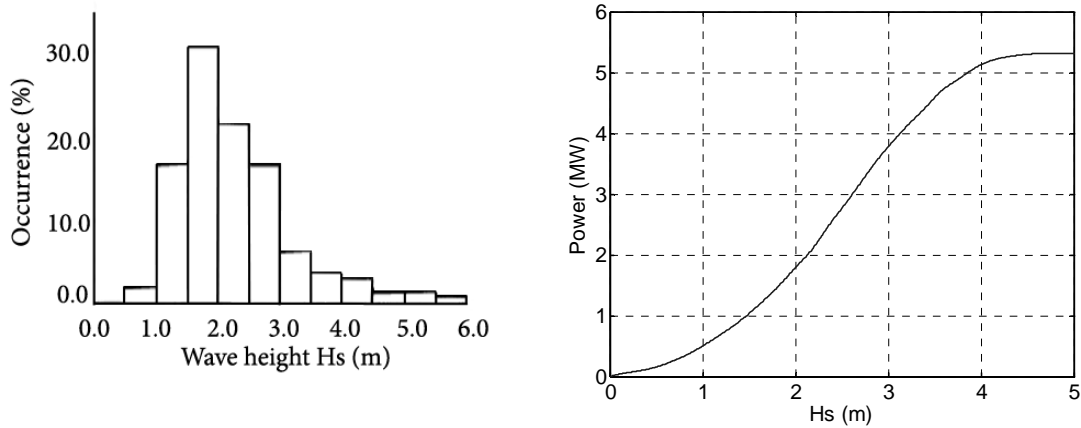


Figure 35: Wave height occurrence and SWEC power curve.

Design water depth is set at 17.5m. According to Retief (1982 and 1984) the SWEC arrays are situated 1.5km off shore in water of a depth of between 15 and 20m.

Converter submergence refers to the distance between the SWL and the level of the chamber opening. It is assumed that midway between high and low tides the submergence of the SWEC is 5.5m (Appendix A). It is necessary to conduct sensitivity as tidal fluctuations range between 1 to 1.5m (Retief, 2006).

At the proposed site the most prevalent wave approach angle is 240° (Retief 1984). SWEC is aligned with these waves varying up to 15° of the optimum, Figure 36.

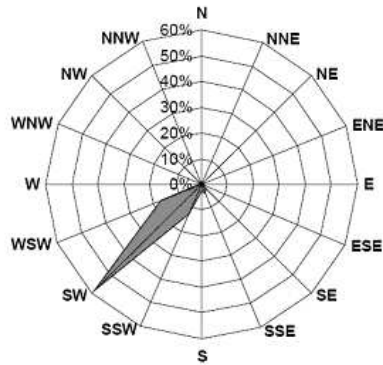


Figure 36: NCEP wave directional rose for the SW South African coast (Joubert, 2008).

The SWEC is designed to be insensitive with respect to this parameter ensuring constant conversion efficiency irrespective of small changes in wave direction.

Wave length and period are mutually dependent (Equation 3). Retief (2008) found that the most prevalent wave period for South African to be 12.3s, but this can be expected to vary from 10 to 14s (Joubert, 2008).

4.3.3. Results and discussions

The section will be extended to a model sensitivity analysis. The Model verification is done by means of mass and energy conservation, see attached CD. The OWC acts as a piston forcing air through the system. Air is drawn from the LP manifold on the down stroke and air is pumped into the HP manifold on the upstroke. It is important to understand the contribution of a single OWC. This is presented below.

The results are fully developed after approximately 24s as the influence of the ramping function has been made negligible (Appendix C). The subsurface pressure signal does not oscillate about the initial value equally; the sea floor in the transitional water depth regime causes the wave form to become cnoidal. This effect is transferred to the motion of the OWC (Figure 37).

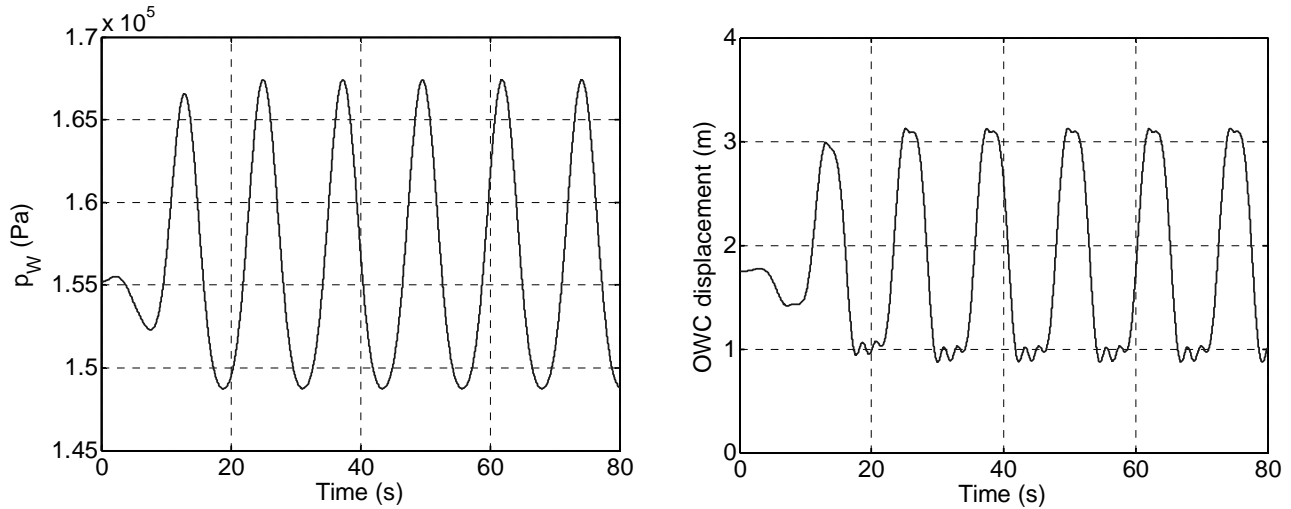


Figure 37: Subsurface pressure and OWC motion.

OWC chamber pressure oscillates (Figure 38) about the initial value in much the same way as the signals in Figure 37, the major exception being that sharp oscillations are introduced. These oscillations are believed to be as a result of the methodology used to govern valve operation (see section 4.3.5).

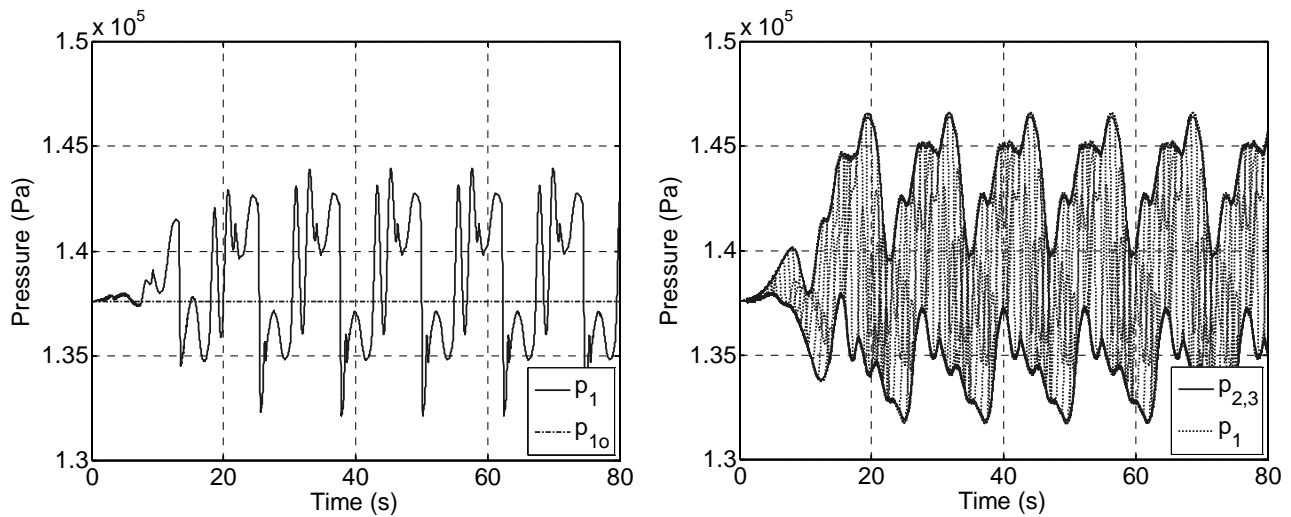


Figure 38: OWC chamber pressure and the effect of OWCs on manifold pressures.

The flow moving through LP and HP manifolds, turbine and diffuser is now analysed. The SWEC primary energy capturing devices is the OWC chamber. Figure 39 compares the contribution of an OWC to that of the whole system.

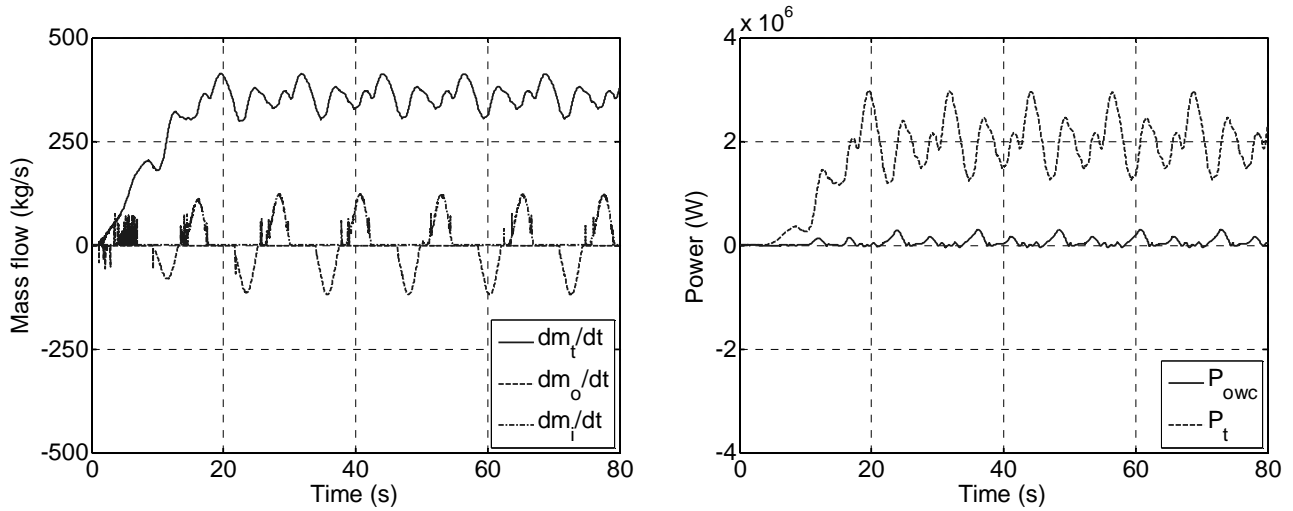


Figure 39: Turbine generated and OWC input power and Mass flow.

The contribution of an OWC chamber is shown in terms of mass flow and power input (Figure 39). The OWC forces flow into and from HP (dm_o/dt) and LP (dm_l/dt) manifolds. Mass flow through the turbine is shown to be unidirectional albeit rippled the mass flow through the turbine averages at 350kg/s. Turbine power signal oscillates about 1.9MW.

Retief (1984) used scale model studies to determine the effect of increased wave height on the system. These results are compared to model results to determine model accuracy (Figure 40).

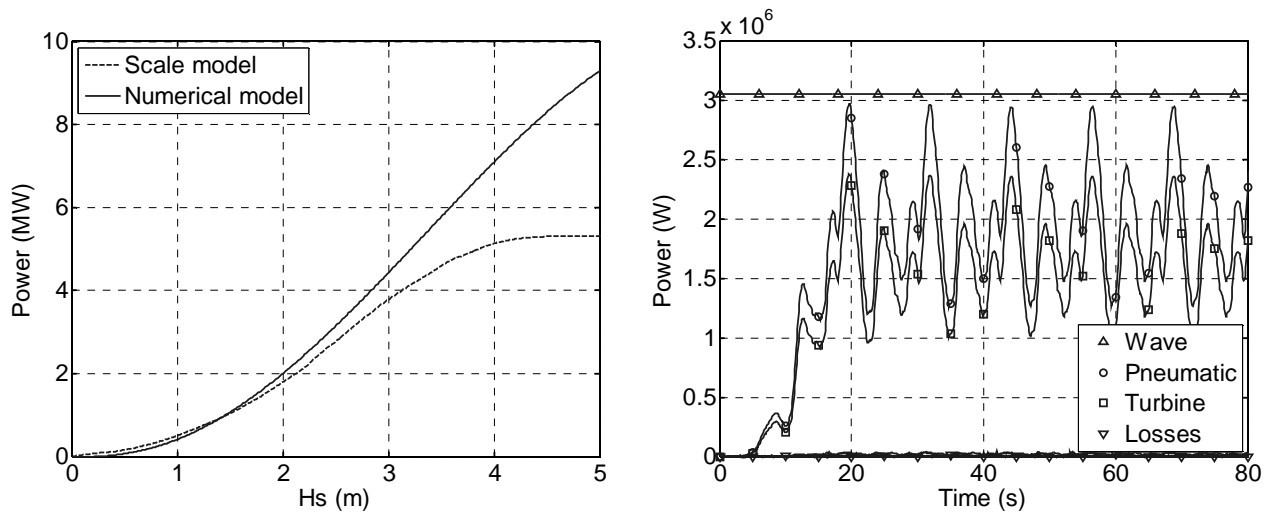


Figure 40: Scale model and numerical model results and the SWEC energy budget.

Figure 40 presents the SWEC energy budget for the 2m wave height design case and power available in the wave climate (approximately 3MW) power in the airflow (averaging out to 2MW), on the turbine shaft (averaging out to 1.9MW) and losses in the airflow system.

The numerical and scale model results compare well up to 3m wave height. From this point the numerical model overestimates power production, and attenuation is only visible from 4m onward. This is believed to be as a result of all or some of the following effects.

- Larger waves become cnoidal in shape. This is believed to lower the amount of energy available to capture as the wave peaks become narrower.
- The second order wave model used doesn't capture all the effects brought about by larger waves.
- Assumed added mass and damping constants become inaccurate at larger wave heights, this would become especially apparent in an irregular sea state (which is not modelled).
- It is possible that in the scale model testing scaling effects are neglected which only become apparent at full size. Such effects could include surface tension and inaccuracies in Froude scaling.

It is promising that the numerical model signal shows attenuation. With the added mass, damping and wave model problems solved the model may be accurate over larger range of wave conditions and become a useful design tool.

The design wave height is analysed by means of a sensitivity analysis, Table 2. Figure 41 shows the expected decrease in power production with an increase in water depth. As mentioned previously the sea floor has a lesser effect on subsurface mechanisms in deeper water.

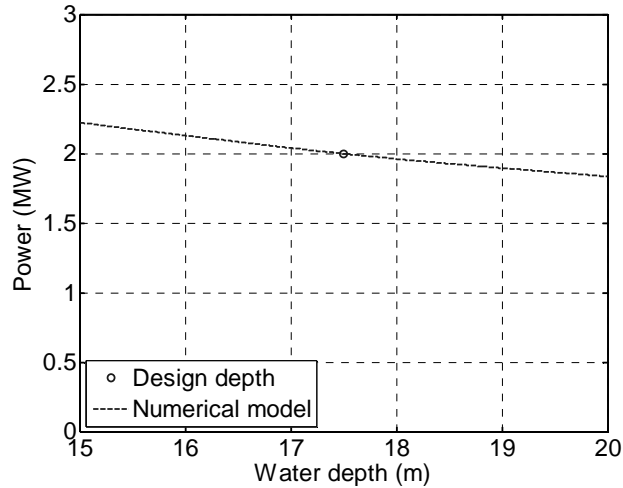


Figure 41: Water depth model sensitivity.

Figure 42 shows that absorbed energy decreases with increased device submergence. An exponential decay of subsurface pressure fluctuations is clearly visible.

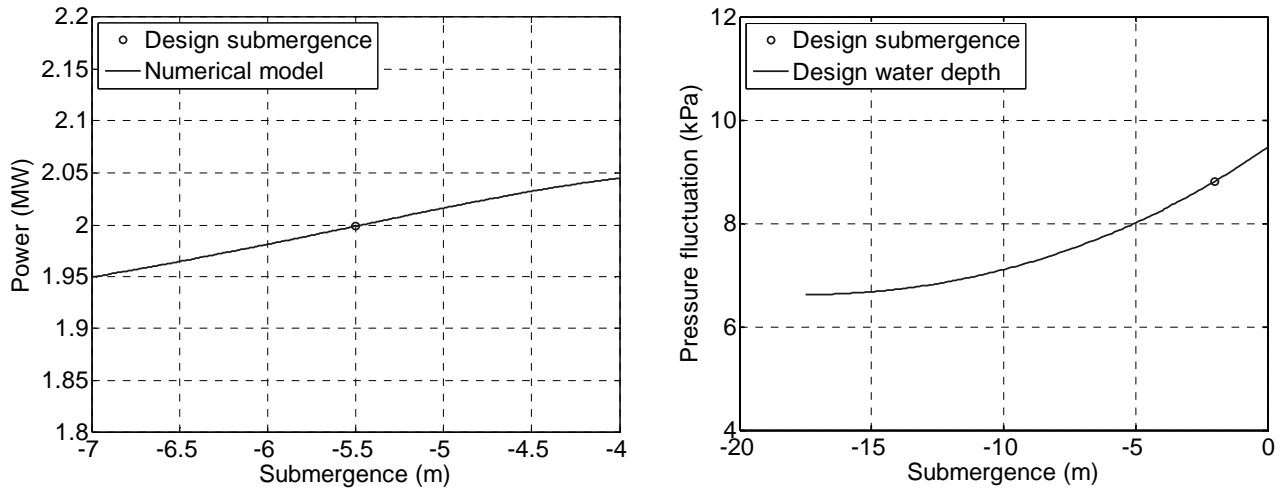


Figure 42: Model sensitivity to submergence and pressure fluctuations.

Figure 43 shows that the SWEC is insensitive to a change in wave approach angle but an initial decrease in generated power is evident up to 10° , the value increases from this point and this is not expected. The discrepancy is put down to inaccurate modelling of added mass and damping. This is understandable as these two terms are believed to be strong functions of device shape (as angle varies so does its shape with respect to oncoming waves).

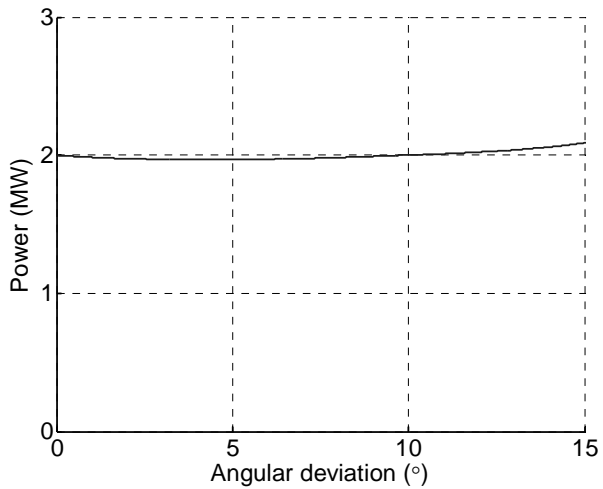


Figure 43: Model sensitivity to wave approach angle.

Wave length increases with period and although there is more power available in longer waves the SWEC is designed to absorb energy from waves the length of an arm or shorter. This characteristic of the SWEC is illustrated in Figure 44. It demonstrates the attenuation of power in extreme conditions.

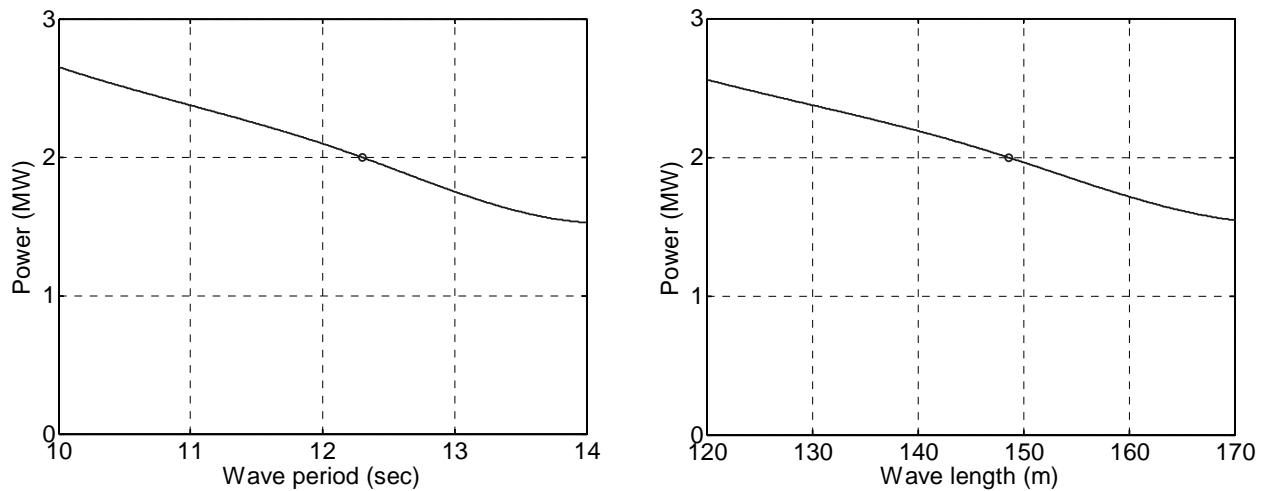


Figure 44: Model sensitivity to wave period and length.

4.4. Conclusion

The model results were presented and shortcomings highlighted in a sensitivity analysis. The average wave condition of 2m and 12.3s is accurately modelled with assumed added mass and damping constants.

The major shortcoming of the model is the variations in flow through the turbine; this is as a result of collector arm length being shorter than the average wave length. Extending the SWEC collector arm length to be equal average wave length would have the effect of smoothing the flow. Figure 45 shows the effect of an extended collector arm length (right) which yields a smooth turbine mass flow. The other shortcomings include sensitivity to wave approach angle beyond 10° off optimum and inaccurate prediction above 3m wave height. The reasons for these shortcomings are presented in the respective sections.

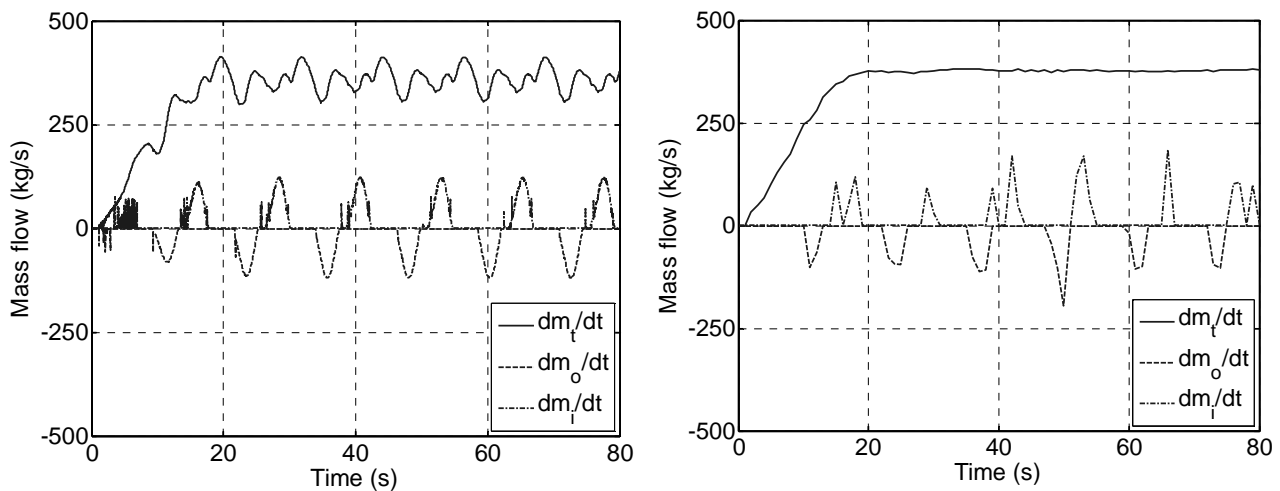


Figure 45: Current model and revised arm length model mass flow.

5. Turbine design

The design of a unidirectional turbine will be discussed in this chapter. The design is divided into three parts; each describing the process with an increased level of complexity. These sections can be described with the following 3D analogy: 1D design defines basic turbine specifications (layout, diameter, hub to tip ratio); 2D design incorporates calculation of flow angles, blade numbers, chord distribution and an initial estimate of total to total performance; 3D design includes blade profile design, stacking of blade profiles and hub and shroud design. In this chapter each design step will be introduced, alternative designs discussed and results presented and discussed.

5.1. 1D Preliminary aerodynamic design

1D design is achieved by calculating the non-dimensional quantities of dimensionless speed and diameter. Balje (1981) presents charts which relate these two quantities to an initial estimate of turbine total-to-static efficiency and layout (centrifugal, axial, radial inflow etc).

5.1.1. Introduction to 1D design

Turbine design is largely a trade-off between size (cost) and efficiency. Larger turbines, although having better performance (and lower diffuser losses) than smaller turbines of the same family, are more costly as a result of the extra material and the expensive generator needed to handle the higher torque load. According to Voutilainen (Fluri, 2008) generator size can generally be approximated to increase linearly with the torque load produced by the turbine and unit cost increases with the increase in generator size.

Designers usually opt for smaller faster moving turbines to lower turbine and generator costs. It is not only these primary costs that should be taken into account but also secondary logistical costs that may play a major role in the design, for instance it may be important to keep turbine diameter small enough to transport components fully assembled without them being classified as abnormal loads under the South African road transport legislation, (Gov, 2008).

5.1.2. Preliminary turbine sizing and performance

Equation 28 and 29 (Balje, 1981) are used to gauge turbine performance (total-to-static efficiency) for a given flow rate, pressure drop, tip and hub diameter. Although rough estimates of performance it is still a useful tool to determine size, speed and layout.

$$n_s = \frac{2^{5/4} U \sqrt{\pi \phi}}{C_o} \lambda \sqrt{\frac{1-\lambda^2}{1+\lambda^2}} \quad \text{Equation 28}$$

$$d_s = \sqrt{\frac{2^{1/2} C_o}{\phi \pi U}} \frac{1}{\lambda} \sqrt{\frac{1+\lambda^2}{1-\lambda^2}} \quad \text{Equation 29}$$

From this early stage to limit the number of design variables it was decided to set hub-to-tip ratio to 40%. The above relations will now be used to illustrate the effects of rotational speed and diameter on performance (Figure 46).

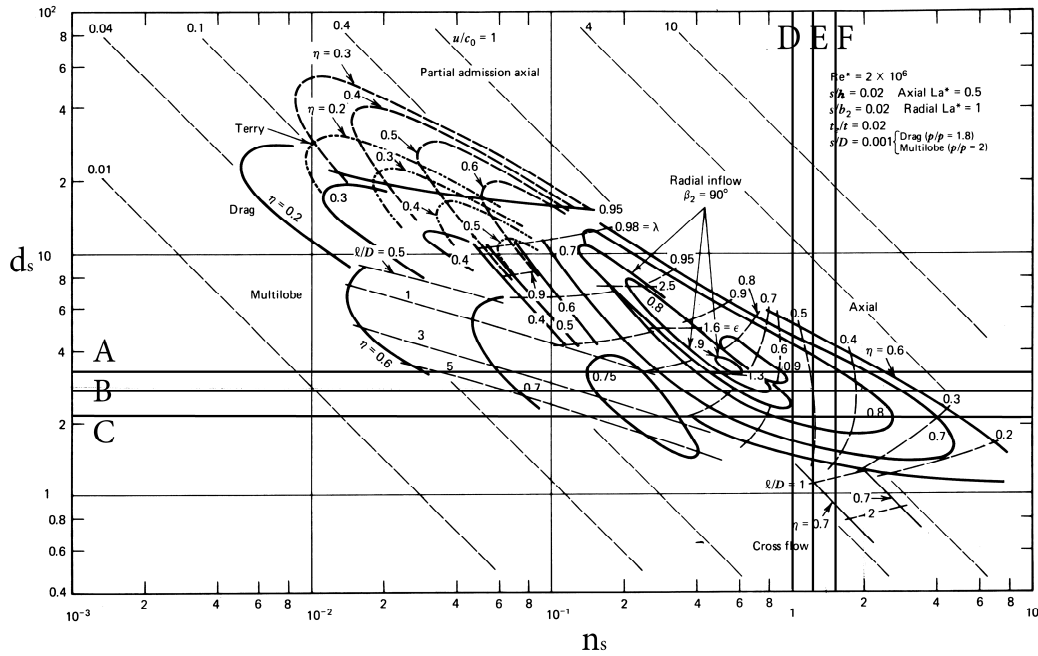


Figure 46: Dimensionless speed and diameter chart (Balje,1981).

Lines marked A, B and C (Figure 46) correspond to diameters 3, 2.5 and 2m and D, E and F correspond to rotational speeds of 1000, 1500 and 2000rpm respectively. The design space lies in the axial flow region. Although larger turbine designs have better performance, the 2.5m diameter option is the most attractive as it would negate afore mentioned logistical costs while having an acceptable level of performance. Slow rotational speed options yield the best performance but also result in large torque loads

the 1500rpm option is selected as the most viable. Figure 47 relates load and flow coefficient (Equation 37 and 38) to estimate total to total efficiency.

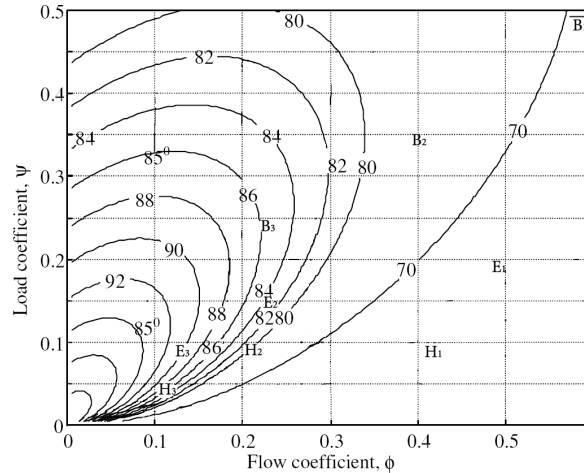


Figure 47: Blade loading vs. flow coefficient (Gannon, 2002).

Table 3 summarizes the design options (also seen in Figure 46) plotted on Figure 47. Figure 47 highlights five possible turbine options H_3 , H_2 , E_3 , E_2 and B_3 with respect to predicted performance. H_3 , E_3 and B_3 can be discarded as they are too large. This leaves H_2 and E_2 as viable options of which H_2 is discarded on the basis of having lower performance (it is in this case assumed that the drop in efficiency would be too large to make the smaller generator a viable option).

Table 3: Summary of design options plotted in Figure 47.

#	D	Ns	Φ	Ψ	#	D	Ns	Φ	Ψ	#	D	Ns	Φ	Ψ
B_1	2	1000	0.78	0.51	E_1	2	1500	0.52	0.22	H_1	2	2000	0.39	0.12
B_2	2.5	1000	0.40	0.32	E_2	2.5	1500	0.26	0.14	H_2	2.5	2000	0.20	0.80
B_3	3	1000	0.23	0.22	E_3	3	1500	0.15	0.10	H_3	3	2000	0.12	0.05

It is interesting to note that most blade loading vs. flow coefficient graphs available in literature do not show the zero intersection of both axes. A possible reason for this is that only the extremely large, slow moving and hence efficient turbines are situated close to the origin. Normal design practice is to “match” the operation of more commonly used gas turbines to the optimal compressor operation which drives it.

5.2. 2D design Flow vectors and angles

This section describes the algorithm used to calculate the distribution of flow angles and chord through the blade length and number blades.

Cohen (2001) stated that with steam turbine design it is common practice to design blades using mean flow conditions keeping blade angles constant. The effect of free vortex blading in high pressure ratio machines is negligible (with respect to improved efficiency). The use of this vortex distribution in low pressure ratio turbines can distinctly improve efficiency (Cohen, 2001). Cohen (2001) also states that the implementation of zero outlet swirl will improve efficiency. Aungier (2006) suggested the use of free vortex design as it is the most commonly used in designing axial flow turbines. Reaction can be described as the degree of expansion which occurs in the rotor with respect to that over the whole stage, in terms of static temperature drop (Equation 30).

$$\Lambda = \frac{(T_2 - T_3)}{(T_1 - T_3)} \quad \text{Equation 30}$$

Although the SWEC air flow system is assumed to operate isothermally, some design parameters are defined with temperature differences between stages (Equation 30). For normal axial turbine design the following simple expressions are derived.

$$C_p (T_1 - T_3) = C_p (T_{01} - T_{03}) = UC_a [\tan(\beta_2) + \tan(\beta_3)] \quad \text{Equation 31}$$

Relative to the rotor, the flow does no work and thus yields the following form of the steady flow energy equation.

$$W_R = C_p (T_2 - T_3) = \frac{1}{2} (V_3^2 - V_2^2) \quad \text{Equation 32}$$

$$= \frac{1}{2} C_a^2 [\sec^2(\beta_3) - \sec^2(\beta_2)] \quad \text{Equation 33}$$

$$= \frac{1}{2} C_a^2 [\tan^2(\beta_3) - \tan^2(\beta_2)] \quad \text{Equation 33}$$

Substituting Equations 31 and 33 into 30 yields an expression for reaction, Equation 34 .

$$\Lambda = \frac{C_a}{2U} [\tan(\beta_3) - \tan(\beta_2)] \quad \text{Equation 34}$$

Reaction ratios should be kept between zero (hub) and one (tip). Negative reaction implies an over expansion of air in the IGV followed by the recompression of air in the rotor (Cohen, 2001). This has a detrimental effect on turbine efficiency.

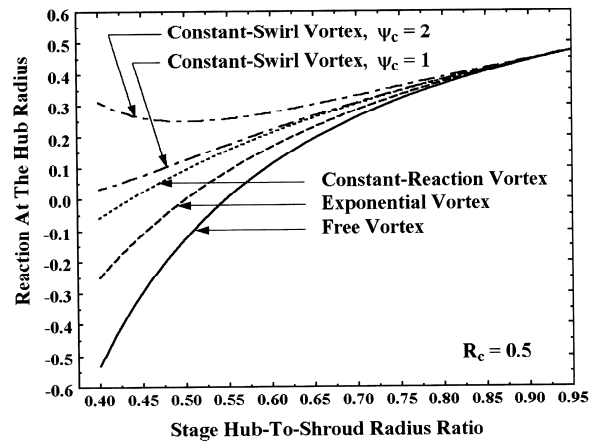


Figure 48: Effect of vortex type on hub reaction, 50% reaction stage (Aungier, 2006).

Figure 48 shows free vortex distribution yields the lowest reaction of all the vortex distributions. Vortex distribution is used to determine flow angles through the length of the blade. Vortex blading types are described below as follows:

- Free vortex: Assures constant angular momentum and meridional velocity (Equation 35) from root to tip. This type is most common for axial flow turbines.

$$C_{mer} = \sqrt{C_a^2 + C_r^2} \quad \text{Equation 35}$$

- Constant-swirl vortex: Assures constant rotor inlet tangential velocity from root to tip. Often chosen to be used in axial flow compressors (allows for untwisted IGVs) and occasionally in axial flow turbines.
- Exponential vortex: Popular for use in axial flow compressors as it assures untwisted IGVs.
- Constant-reaction vortex: Yields a constant reaction if meridional velocity across the rotor is constant or if the mean radius reaction is equal to unity.
- Constant nozzle-angle vortex: Recommended to axial flow turbines if a low-cost design is the main objective. The IGV are of constant cross-section

Considering the above information and the simplicity to implement this theory, free vortex distribution is chosen. It is shown in Figure 57 that negative reaction ratios are avoided. This is the major concern with using this theory, Figure 48. Figure 49 shows velocity triangle definitions.

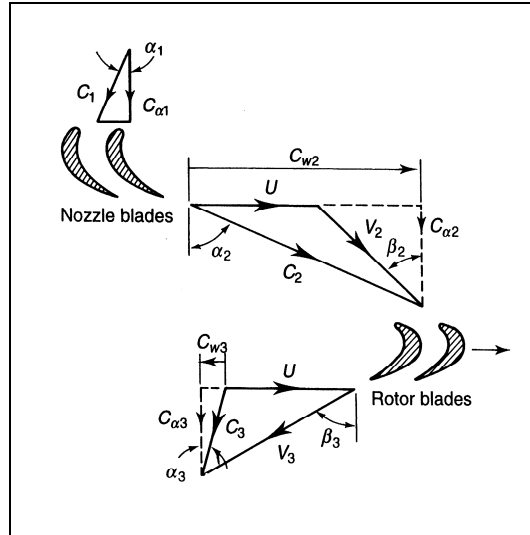


Figure 49: Flow velocity triangle convention (Cohen, 2001).

5.2.1. Turbine design input data

The main objective of the 2D design is to determine an optimal design. This design includes flow angles, number of blades and chord distributions. The algorithm uses the Zweifel criterion (Dixon, 1998) to determine an optimum space to chord ratio. Figure 50 explains the flow of the algorithm.

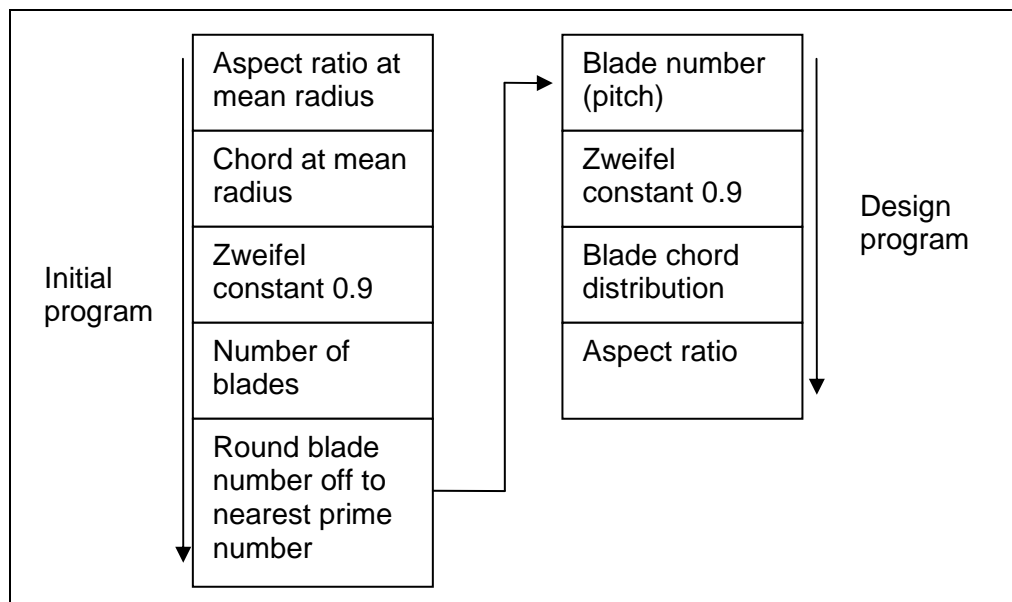


Figure 50: Design program flow with respect to chord and blade number selection.

To determine the number of blades in rotor and IGV rows it is necessary to assume either a blade pitch (blade number) or chord distribution. The Zweifel criterion is used to

calculate chord or blade numbers. The method followed in this study is to assume an aspect ratio of 3.5 at mean radius. Cohen (2001) recommends a ratio between 3 and 4 ensuring blade strength and limiting vibration problems. The Zweifel criterion is used to calculate the number of blades. The blade number is rounded of to the nearest prime number to lessen the effect of blade passing frequencies.

The code is now modified to accept blade numbers as an input, using Zweifel to calculate chord distribution (Figure 50). The design inputs are listed below.

- Inlet total temperature (T_{01}).
- Inlet total pressure (p_{01}).
- Total pressure drop (Δp) over turbine.
- Flow rate through turbine (\dot{Q}).

5.2.2. Flow angle program algorithm

A brief explanation of the algorithm is now presented. For a detailed explanation in the form of a sample calculation refer to the attached CD. An initial estimate of total-to-total efficiency is made and the total temperature drop over the turbine is calculated using Equation 36 (Cohen, 2001).

$$\Delta T_0 = \eta_{tt} \left[1 - (p_{03}/p_{02})^{(\gamma-1/\gamma)} \right] \quad \text{Equation 36}$$

NTGE (Cohen, 2001) practice is used to calculate the load coefficient (Equation 37) using the temperature drop. The flow coefficient is also calculated (Equation 38)

$$\psi = \frac{2C_p \Delta T_0}{U_m^2} \quad \text{Equation 37}$$

$$\phi = \frac{C_a}{U_m} \quad \text{Equation 38}$$

Flow vectors and angles are calculated with each station described in terms of the following equations. The stations are numbered as shown in Figure 49.

$$\alpha_1 = 0^\circ \quad \text{Equation 39}$$

$$C_1 = C_a \quad \text{Equation 40}$$

$$\alpha_2 = \text{atan} \left[\frac{1}{\phi} + \tan(\beta_2) \right] \quad \text{Equation 41}$$

$$\beta_2 = \text{atan} \left[\frac{\psi}{2\phi} - \tan(\beta_3) \right] \quad \text{Equation 42}$$

$$C_2 = \frac{\phi U}{\cos(\alpha_2)} \quad \text{Equation 44}$$

$$V_2 = \frac{\phi U}{\cos(-\beta_2)} \quad \text{Equation 45}$$

$$\alpha_3 = 0^\circ \quad \text{Equation 43}$$

$$\beta_3 = \text{atan} \left(\frac{U}{C_3} \right) \quad \text{Equation 44}$$

$$C_3 = C_a \quad \text{Equation 45}$$

$$V_3 = \sqrt{U^2 + C_3^2} \quad \text{Equation 46}$$

The Zweifel (Dixon, 1998) criterion for optimum space-cord ratio (ψ_T) is essentially the ratio of actual (Equation 47) to ideal (Equation 48) tangential blade loading, constant for minimum losses. Loadings are obtained from real and ideal pressure distributions on both pressure and suction blade surfaces.

$$Y = \rho s C_x (C_{\theta 2} + C_{\theta 1}) \quad \text{Equation 47}$$

$$Y_{id} = \frac{1}{2} \rho C_2^2 b \quad \text{Equation 48}$$

Ideal loading can only be realized if total inlet pressure acts on the whole pressure surface (P) of the blade and static outlet pressure acts on the blade suction surface (S), which is impossible, Figure 51.

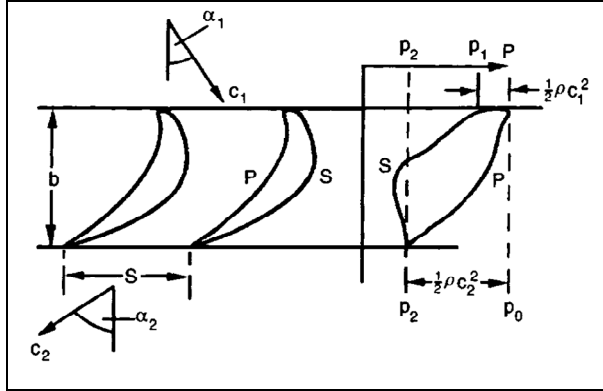


Figure 51: Pressure distribution around a turbine cascade blade (Dixon, 1998).

The Zweifel criterion can be expressed in terms of absolute ($\alpha_{1,2}$) or relative ($\beta_{1,2}$) flow angles for IGV or rotor, blade axial cord (b) and pitch (s), (Equation 49).

$$\psi_{T,R,S} = \frac{Y}{Y_{id}} = 2 \left(\frac{s}{b} \right) \cos^2(\alpha_2) \left[\tan(\beta, \alpha_1) + \tan(\beta, \alpha_2) \right] \quad \text{Equation 49}$$

Zweifel found that a value of 0.8 for ψ_T corresponded to the minimum loss case. Horlock (1966) showed that for outlet angles other than those from 60 to 70 the criterion does not give accurate estimates of space-cord ratio. Recent work suggests a value of 0.9 for the Zweifel constant (Aungier, 2006). The higher value for the Zweifel constant relates to higher blade loading and hence a less expensive turbine with fewer blades.

Performance prediction is theoretically analyzed using the Soderberg loss model (Lewis, 1996 and Dixon, 1998). Soderberg found that losses correlate with space-chord, aspect and thickness-chord ratios and Reynolds numbers (Dixon, 1998). Figure 52 shows the relation between loss coefficient and flow deflection.

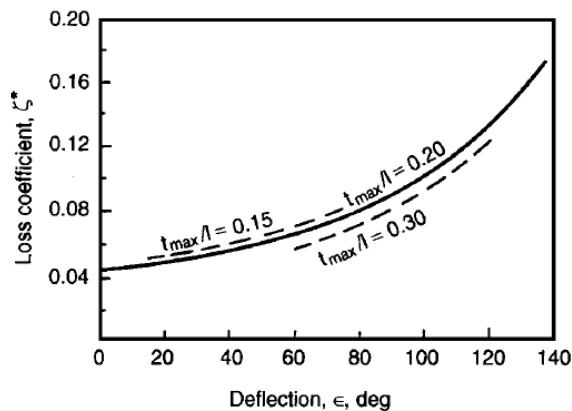


Figure 52 : Soderburg loss coefficient vs. fluid deflection (Dixon, 1998).

Total-to-total efficiency (Equation 50) is calculated using the Soderburg loss coefficients, Equation 51. For turbine flow Reynolds numbers of 10^5 and blade aspect ratios of 3 the nominal loss coefficient can be expressed as in Equation 51. Correction for aspect ratio and Reynolds number are done by implementing Equation 52 and 53.

$$\eta_{tt} = \left[1 + \left(\left(\zeta_S C_2^2 + \zeta_R V_2^2 + \zeta_D C_3^2 \right) / U^2 \psi \right) \right]^{-1} \quad \text{Equation 50}$$

$$\zeta_{R,S} = 0.025 \left[1 + \left(\varepsilon_{R,S} / 90 \right)^2 \right] \quad \text{Equation 51}$$

$$\zeta_{\text{secR},S} = 3.2 \left(\frac{b}{h} \right) \zeta_{R,S} \quad \text{Equation 52}$$

$$\zeta_{\text{corrR},S} = \left(10^5 / \text{Re} \right)^{1/4} \left(\zeta_{R,S} + \zeta_{\text{secR},S} \right) \quad \text{Equation 53}$$

Diffuser loss (ζ_D) is set to 0 or 1 if total-to-total or total-to-static efficiency are to be calculated (Von Backström, 2003) the definition for this factor is described (Equation 54).

$$\zeta_D = \frac{\Delta p_0}{\frac{1}{2} \rho C_3^2} \quad \text{Equation 54}$$

The diffuser is a component of a fluid flow system designed to reduce velocity and thereby increase static pressure. The trade off in designing diffusers is to assure maximum diffusion cross sectional area increase without flow separation. The design variables include diffuser length, inlet and outlet cross-sectional area.

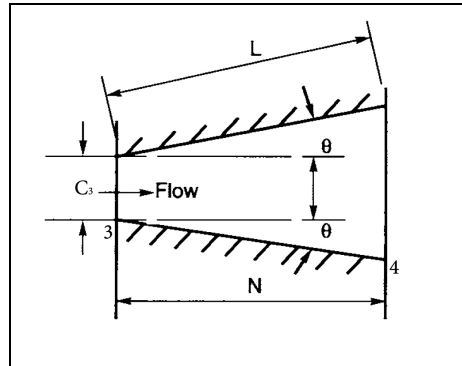


Figure 53: Conical diffuser geometry (Dixon, 1998).

Diffuser performance can be evaluated by two methods. Either by determining the actual change in enthalpy in relation to isentropic enthalpy change or by using the ratio of actual pressure rise coefficient (Equation 55) to isentropic pressure rise coefficient (Equation 57) (Dixon, 1998). The second method is used in this study.

$$C_p = \frac{2(p_3 - p_4)}{\rho C_3^2} = \frac{p_4 - p_3}{p_{03} - p_3} \quad \text{Equation 55}$$

$$AR = \frac{A_4}{A_3} \quad \text{Equation 56}$$

$$C_{p_{id}} = 1 - \left(\frac{C_4}{C_3} \right)^2 = 1 - \left(\frac{1}{AR} \right)^2 \quad \text{Equation 57}$$

Total pressure loss coefficient (Equation 54) is expanded and shown in Equation 58.

$$\zeta_D = \frac{p_{03} - p_{04}}{p_{03} - p_3} = \frac{p_{03} - p_{04}}{\frac{1}{2} \rho C_3^2} \quad \text{Equation 58}$$

Equation 58 can be expressed in terms of total and dynamic pressure components (from Bernoulli's equation). This approach may not hold as Bernoulli's equation is only valid along a stream line and there is no assurance that diffuser flow is uniform. Dynamic pressure components are therefore be written as area averages (Japikse, 1994).

$$C_p = \left[\left(p_{04} - \frac{1}{A_4} \int C_4^2 dA \right) - \left(p_{03} - \frac{1}{A_3} \int C_3^2 dA \right) \right] / \left(\frac{1}{A_3} \int C_3^2 dA \right) \quad \text{Equation 59}$$

$$= -\zeta_D + 1 - \left(\frac{1}{A_4} \int C_4^2 dA \right) / \left(\frac{1}{A_3} \int C_3^2 dA \right) \quad \text{Equation 60}$$

$$= -\zeta_D + 1 - \frac{\overline{C_4^2}}{\overline{C_3^2}} \quad \text{Equation 61}$$

From continuity we know that Equation 62 must be true.

$$\overline{C_4} A_4 = \overline{C_3} A_3 \quad \text{Equation 62}$$

If we assume that Equation 63 holds true then by substitution a simple relation for C_p and ζ_D is obtained, Equation 64 (Japikse, 1994).

$$(\overline{C})^2 = \overline{C^2} \quad \text{Equation 63}$$

$$C_p = -\zeta_D + 1 - \frac{1}{AR^2} \Rightarrow \zeta_D = C_{p_{id}} - C_p \quad \text{Equation 64}$$

Diffuser efficiency is defined as the ratio between real and ideal diffuser performance coefficients, Equation 65.

$$\eta_D = \frac{C_p}{C_{p_{id}}} \quad \text{Equation 65}$$

Sovran (1967) states that the uniformity and or steadiness in flow at diffuser exit are as important as flow velocity reduction (static pressure rise). Inlet flow blockage is the

major factor in the formation of these non-uniform flow states. Figure 54 shows possible occurrence of unsteadiness in diffuser exit flow.

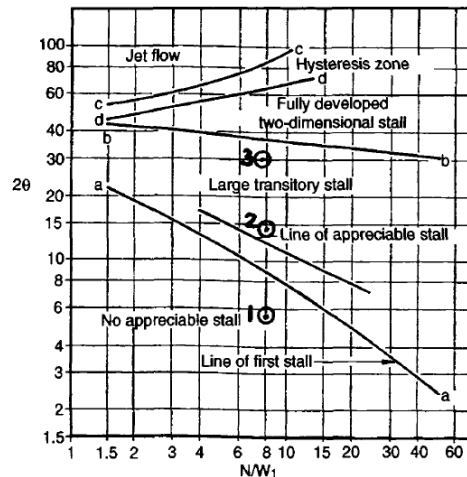


Figure 54: Flow regime chart for two dimensional diffusers (Sovran 1967).

Figure 54 originally correlated by Kline (1959) shows four flow types. “No appreciable stall” regime is steady and uniform. “Large transitory stall” is unsteady and non-uniform. “Fully-developed” and “jet flow” are reasonably steady but very non-uniform.

Sovran (1967) found that a thickening of the inlet boundary layer was the major contributor to drop in diffuser performance. Stated differently, rather than insufficient flow diffusion it is inefficient flow diffusion that is often the cause of poor performance (Dixon, 1998). Runstadler (1975) confirms this by stating blockage is the major factor and its influence supersedes all other factors, which include Mach number, Reynolds number, velocity profile and turbulence level. One could say diffusers are characterized by a boundary layer that grows toward the exit as a result of the adverse pressure gradient and flow tends to separate from the diffuser wall. The result of flow separation and the growing boundary layers is effectively to block the passage for flow (Equation 66).

$$B_3 = 1 - \frac{A_{3\text{eff}}}{A_3} \tag{Equation 66}$$

If flow characteristics of a diffuser are known i.e. the Reynolds number and blockage, the diffuser maps can be used to determine performance (Runstadler 1975). However maps are only valid for a low range of Reynolds number of around 10^5 or less. In this study

Reynolds numbers are of the order of 10^6 . With no experimental studies done on similar diffuser geometries determining blockage is impossible. Inlet blockage is expected to lie between 2 and 5% as the diffuser angle of divergence is mild. Figure 55 shows model sensitivity toward inlet blockage is negligible and a value 2% can safely be assumed.

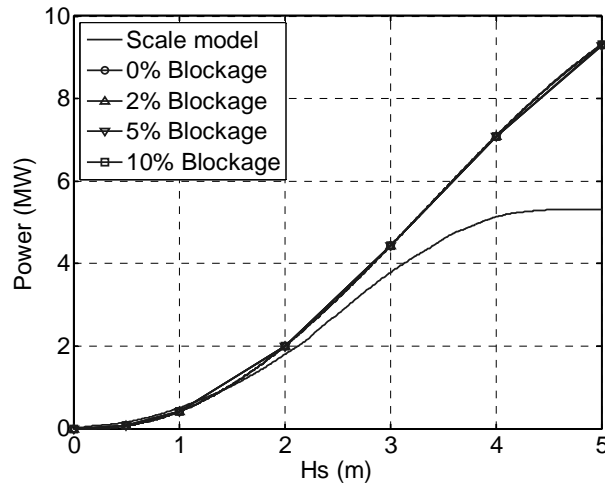


Figure 55: Model sensitivity to diffuser inlet blockage.

Sovran (1967) showed in a study on 2D, conical and annular un-curved diffusers that correlation can be drawn to determine performance of the diffusers as a function of blockage. Figure 56 shows the best fit for all diffuser geometries, correlating inlet blockage with effective outlet area ratio (from which outlet blockade can be calculated).

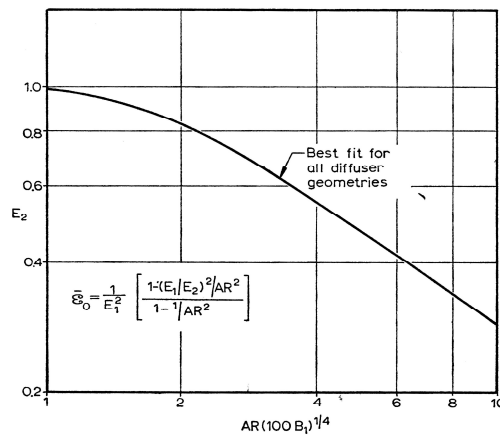


Figure 56: Effect of inlet boundary layer blockage on performance (Sovran, 1967).

The overall effectiveness (Equation 67) represents the ratio of actual to ideal pressure recovery coefficient (Equation 68).

$$\varepsilon_D = \frac{1}{E_3^2} \left[\frac{1 - (E_3/E_4)^2 / AR^2}{1 - 1/AR^2} \right] \quad \text{Equation 67}$$

$$\varepsilon_D = \frac{C_p}{C_{p_{id}}} \quad \text{Equation 68}$$

Free vortex theory is now used to distribute the flow angles through the length of the blades (Equations 69 through 72).

$$\tan \alpha_2 = \left(\frac{r_m}{r} \right)_S \tan(\alpha_{2m}) \quad \text{Equation 69}$$

$$\tan \beta_2 = \left(\frac{r_m}{r} \right)_S \tan(\alpha_{2m}) - \left(\frac{r_m}{r} \right)_S \frac{U_m}{C_{a2}} \quad \text{Equation 70}$$

$$\tan \alpha_3 = \left(\frac{r_m}{r} \right)_R \tan(\alpha_{3m}) \quad \text{Equation 71}$$

$$\tan \beta_3 = \left(\frac{r_m}{r} \right)_R \tan(\alpha_{3m}) - \left(\frac{r_m}{r} \right)_R \frac{U_m}{C_{a3}} \quad \text{Equation 72}$$

5.2.3. Results

Resulting from the 2D design is a turbine stage of 29 IGVs and 14 rotor blades with a predicted total-to-total efficiency of 90%.

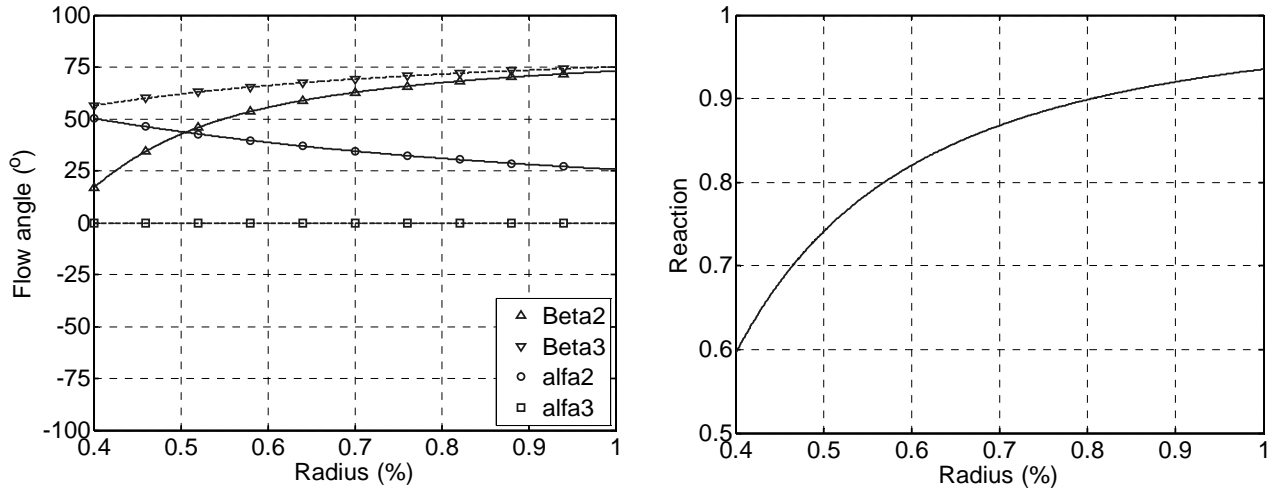


Figure 57: Flow angles and Reaction ratio.

Figure 57 shows flow angles close to the hub change rapidly which is indicative of highly twisted blades, becoming un-cambered toward the tip. Twisted blade roots stiffen blades and help to prevent vibration problems.

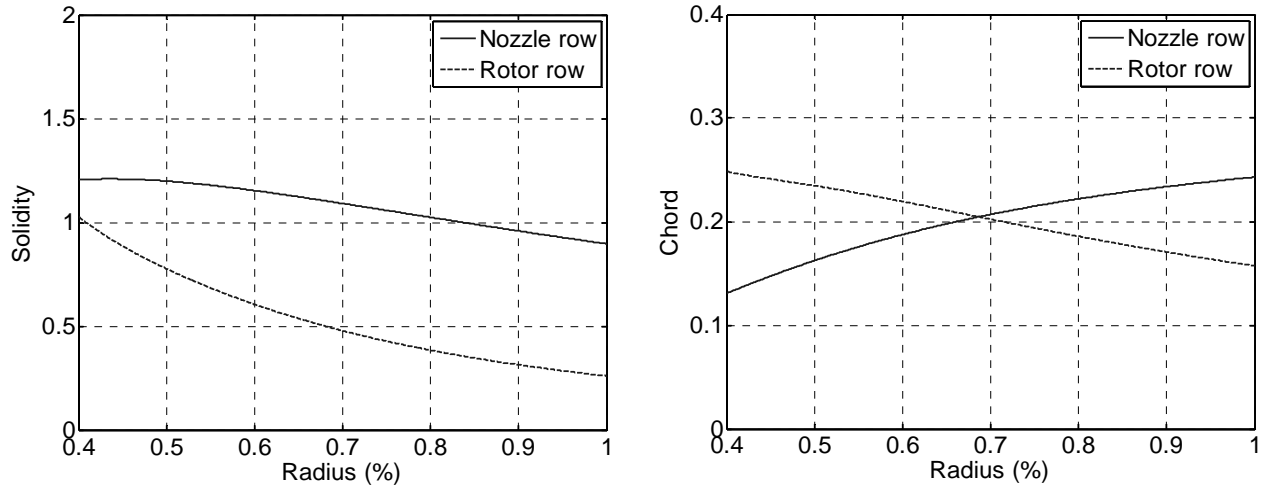


Figure 58: Turbine solidity and chord.

Figure 58 shows that the solidity of both the IGVs and rotor blade rows diminish towards the blade tip, with the IGV solidity dropping below unity above 80% span. The blocking of flow through the turbine (achieved by articulating the IGVs to their full extent) for either the purposes of maintenance or for halting power production in extreme sea conditions is believed to be adequate in this case. Stated differently the blockage caused by turning IGVs will adequately throttle the flow for the above mentioned purposes.

5.3. 3D turbine Design

3D design includes design of blade sections, definition of stacking laws for blade rows, orientation of blade rows and the design of hub and shroud surfaces.

5.3.1. Blade section design

Blades are divided into eight sections, four sections along the blade, two either side of the hub and two either side the shroud. The spacing is done in such a way as to describe the blade twist and to ensure a smooth and continuous surface up to the casings.

Blade profile design is achieved using Cascade which written by Lewis (1996) utilizes the panel method to calculate flow over an aerofoil, predicting exit angle for given thickness distribution, pitch-to-chord ratio, camber and stagger angle. NACA profiles designed primarily for use as aerofoils are an attractive alternative to turbine profiles (NGTE, T4 etc) as characteristics are well know and gains brought about by using turbine profiles are expected to be minimal when designing LP ratio turbines as is this case here.

Cascade (Lewis, 1996) completes a basic flow analysis yielding a prediction for blade surface pressure distribution. Although not the most accurate method, simplicity and rate at which new profiles can be generated makes it a useful tool in the design process.

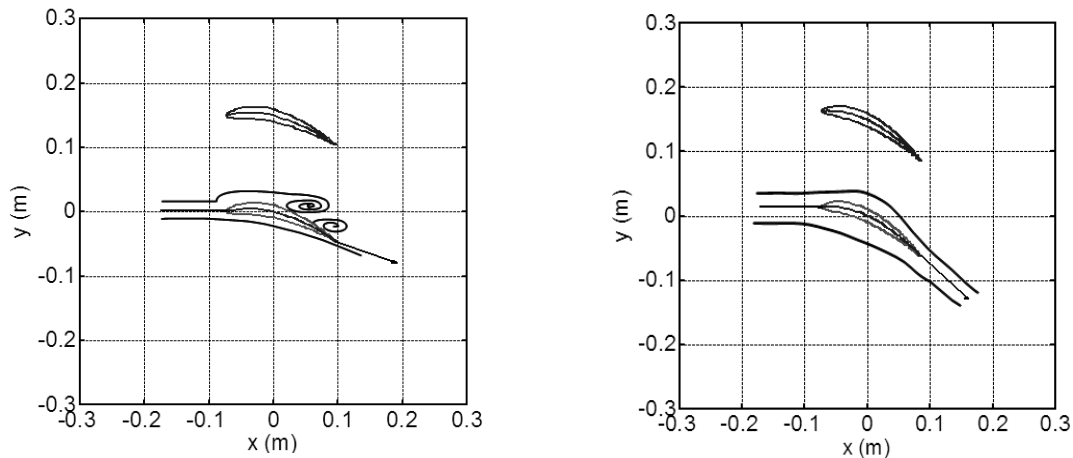


Figure 59: Stream lines over blade profiles illustrating correct profile design.

Stagger and camber angles are altered to deliver required flow deviation without causing separation or unnecessary obstruction. When altering these angles it is important to ensure flow moves smoothly over the profile nose and does not separate over the tail (Figure 59). A convergent blade channel is essential to enable efficient flow deflection.

5.3.2. Blade stacking law

Blades are articulated during operation, to throttle flow in extreme conditions or adapt to flow variations. Blades are stacked on the thickest portion of the profiles enabling the use of the strongest possible fastener. This lowers moment forces acting on this attachment device assuming the centre of gravity of the profiles lies close to this point.

IGV design is illustrated in Figure 60.

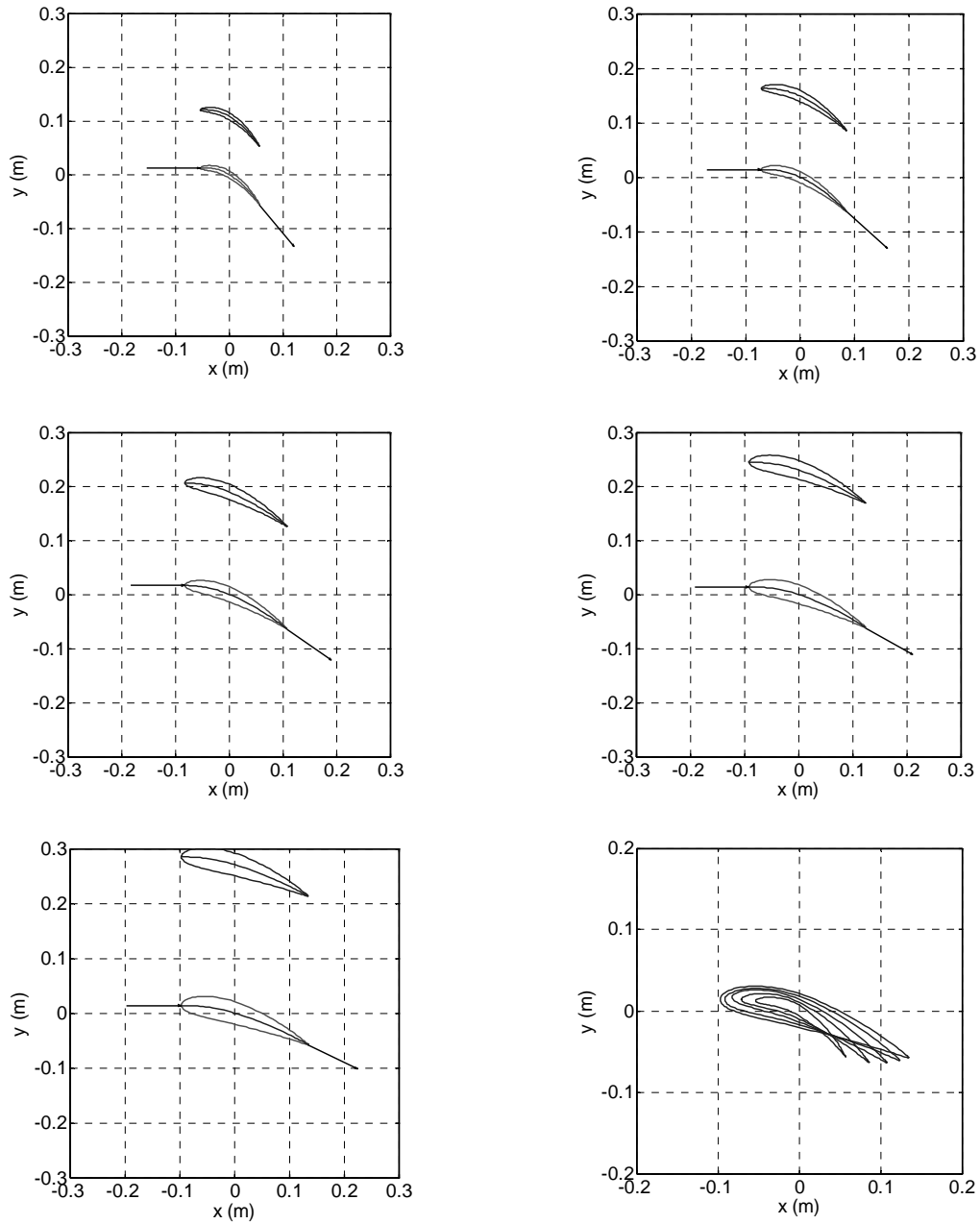


Figure 60: IGV inlet and outlet flow vectors at hub, quarter, half, three quarter and tip profiles and profile stacking.

Rotor blade design is illustrated in Figure 61.

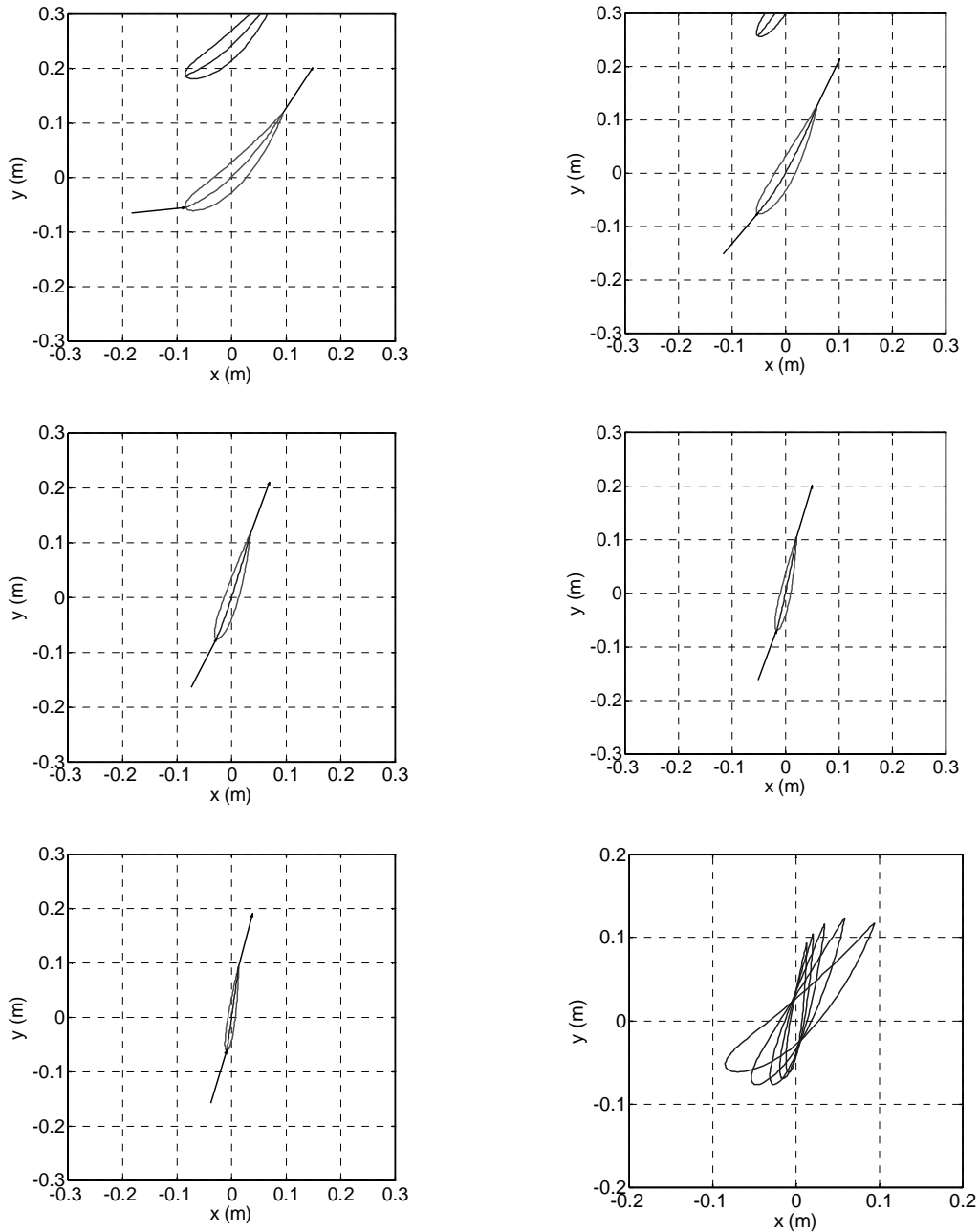


Figure 61: Rotor inlet and outlet flow vectors at hub, quarter, half, three quarter and tip profiles and profile stacking.

5.3.3. Blade taper

IGV and rotor blade thickness and chord, grow in the same direction. Taper helps limit vibration problems and increases the strength of the rotor hub. The less material at the

tip of the blade the lower the centrifugal forces acting on the blade. The only constraint on the thinnest portion of the IGV is that it is thick enough to be supported by the fastening device.

5.3.4. Tip clearance

The IGV is located flush on the hub and shroud. The rotor however is separated from the shroud by a tip gap. When designing a tip gap it is important to ensure there is no interference between blade and casing during operation and that resulting leakage losses do not affect the overall performance excessively. Sjolander (1997) suggests a tip gap of 1% of the span of the blade. Wei (2007) shows that total pressure loss coefficients at various exit Mach numbers for this case are almost equal, where marked differences were evident in cases of larger gaps. This indicates the 1% gap does not appreciably disturb the flow.

5.3.5. Blade spacing

Closely spaced rows ensuring compact design are preferred, but care is to be taken to prevent the wake of upstream blades affecting performance of downstream blades. Cohen (1987) suggests a gap $\frac{1}{4}$ of the blade width. In this design the gap is taken to be a $\frac{1}{4}$ of the mean IGV width (Figure 62).

5.3.6. 3D turbine assembly

The design of the hub and shroud surfaces and assembly of blade rows is presented here. The hub and shroud are to be made spherical in shape to allow the blades to be in contact with both surfaces regardless of stagger (Figure 62).

The hub ends sharply downstream of the turbine. The main reason for this is to reduce weight and cost of the turbine module and prevent growth of a boundary layer (increased blockage) in the centre of the diffuser.

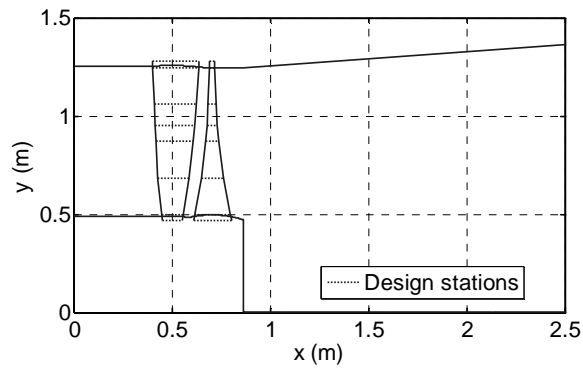


Figure 62: Spherical hub, shroud and diffuser, flow enters from the left through IGVs.

A known disadvantage of diffuser operation is that velocity profiles become progressively “peaky” in shape toward the exit, thus reducing the diffuser effectiveness. The blunt hub will have the effect of flattening the profile even though flow will separate from the hub.

5.4. Conclusion

In this chapter the design of a turbine is completed, initial size and operation estimates were refined into detailed blade, hub and shroud designs. The design was assembled in 3D and prepared for CFD numerical modelling.

6. Turbine numerical modelling

The CFD package NUMECA (Fine, 2008) is used to model the turbine. Unlike other CFD packages NUMECA is specifically designed for the purposes of design, modelling and optimisation of turbomachinery. The NUMECA environment integrates the following modules that are used in the various stages of the modelling process.

- Interactive Geometry modeller and Grid generation software (IGG™), based on structured multi-block techniques. Multi purpose meshing tool.
- 3D Automated Grid generation software (AutoGrid™), dedicated to turbomachinery applications. Used for the meshing of the blade passages.
- Flow solver (Euranus), able to simulate Euler and Navier-Stokes equations in the laminar, transitional and turbulent regimes.
- Post processing software (CFView™).
- Graphical User Interface (FINE™) which combines and links all modules.

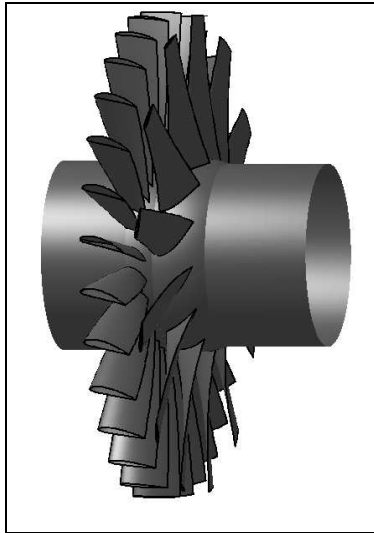


Figure 63: Turbine layout.

The main objectives in the modelling process are to investigate design condition operation, off design operation, effectiveness of the diffuser on overall performance and to investigate the onset of stall.

6.1. Introduction

The final step in the assembly of the numerical model of the turbine is done in the IGG and AutoGrid meshing tools. FINE is used to run simulations; firstly the turbine itself is modelled at design and off design conditions. Then the full turbine diffuser model is simulated; this is done to enable the designer to gage the effectiveness of the diffuser.

The chapter will be divided into the three main sections, pre-processing, numerical model setup and simulation and post processing results.

6.2. Pre-processing

Pre-processing includes the building of turbine geometry in grid generators IGG and AutoGrid. The meshing of blade passages and the diffuser are described. The diffuser and turbine are linked with a Full Non-Matching Boundary FNMB (Fine, 2008), where none of the cells on either interface share common vertexes.

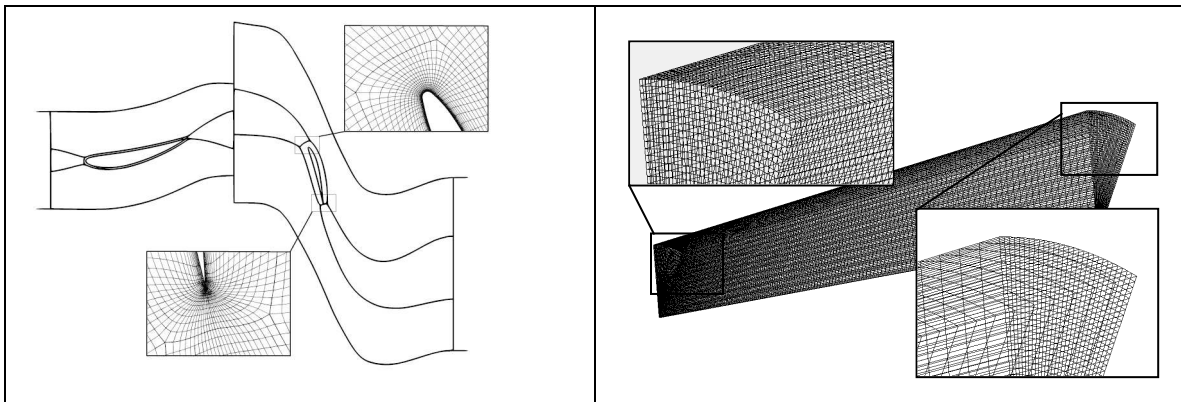


Figure 64: Meshing scheme of blade rows (Fluri, 2008) and of a sector of the diffuser.

It is important that grid quality is maintained throughout the computational domain, cell skewness, aspect and expansion ratio are kept within workable levels. The resolution of boundary layer is ensured by maintaining y^+ values below 10, a requirement of the Spalart-Allmaras turbulence model (Fine, 2008) used in this model.

6.2.1. Blade passage

The HOH meshing scheme is implemented over blade passages (Figure 64), an H block at the inlet, outlet, above and below the blade, the O block surrounds the blade to improve meshing ability round sharp bends and edges (Fine, 2008). These meshed

corridors are stacked through the length of the blade. The tip gap is meshed by meshing the space where the blade would have been had it extended all the way to the shroud.

6.2.2. Diffuser

The diffuser mesh is finer at inlet than the outlet to ensure that in-flow over the turbine hub is modelled accurately. An increased mesh size at the exit lowers cell count and computational cost (Figure 64). As mentioned the turbine and diffuser are linked by a FNMB.

6.3. Numerical model

This section describes the problem set up in NUMECA (Fine, 2008), including definition of fluid model, boundary and initial conditions and of the solution method. The model is set up to run at various flow conditions to investigate off design operation.

6.3.1. Flow configuration

Air (real gas) is defined as the fluid model and the solution assumed to be steady. The one-equation Spalart-Allmaras turbulence model and Abu-Ghannam and Shaw transitional model are activated as Fluri (2008) showed to work well in a similar turbine. The rotational and stationary boundaries are set.

6.3.2. Boundary conditions

Total quantities are imposed at model inlet boundaries (Fine, 2008), setting velocity direction at inlet and total pressure and temperature. At the outlet mass flow is imposed and an initial static pressure is set, Table 4.

Table 4: Boundary conditions for design condition (2m Hs).

Inlet total pressure (Pa)	143690
Inlet total temperature (K)	288.15
Inlet flow direction	Axial (no swirl)
Outlet mass flow (kg/s)	357.1
Outlet initial pressure (Pa)	132230

6.3.3. Numerical model

Fine (2008) is equipped with multigrid functionality, Figure 65. A multigrid level is defined by a three digit code; e.g. 111. Each digit has reference to a direction on the local coordinate system (x,y,z). The finest level being (000) and the coarsest grid level used in this study is (222). Successive model results can be used as initial solutions for finer meshed models. Convergence is achieved once residuals have decreased by five orders of magnitude and mass flow error is less than 0.1%.

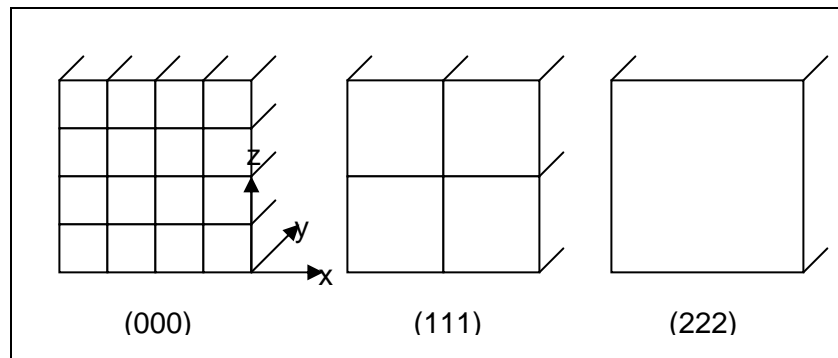


Figure 65: Multi grid functionality from fine (0 0 0) to course (2 2 2).

6.4. Post processing (results)

The design condition results will be presented and discussed. The effect of diffuser on turbine performance will then be presented followed by the off design simulation results.

6.4.1. Design condition

The validation of the turbine design is done by simulation of the design condition. This model is built without a diffuser so as to limit computational time.

The grid independence of the model is illustrated, showing the convergence of the three major velocity components at all three turbine stations. In each case the final converged solution is shown on the left.

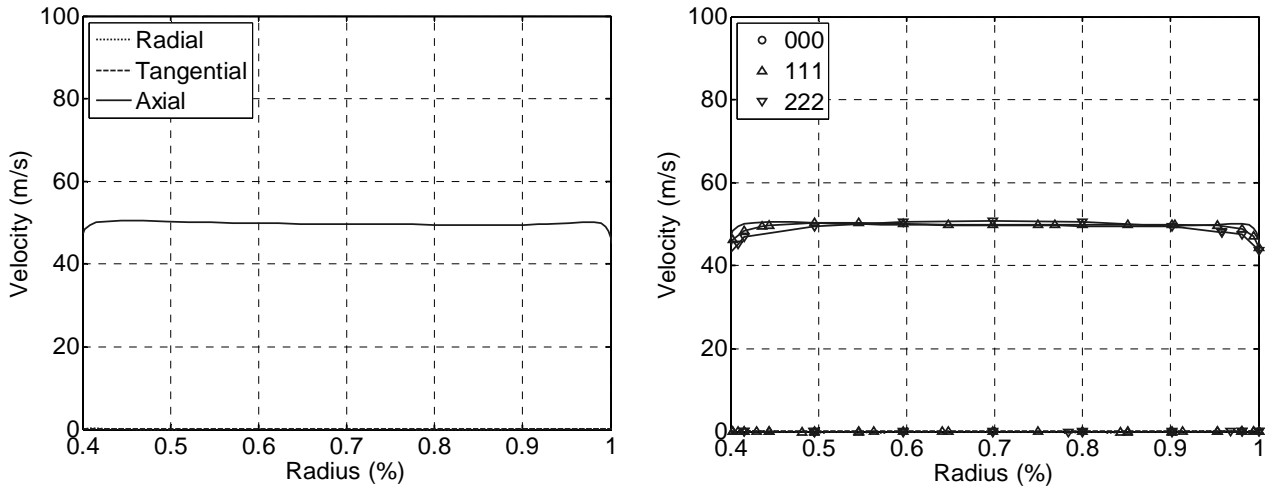


Figure 66: Turbine inlet flow magnitude.

The turbine is designed for axial inlet flow and the results reflect this well (Figure 66). The inlet flow is constant over the annulus apart from portions of the flow affected by the presence of a solid boundary (hub and shroud).

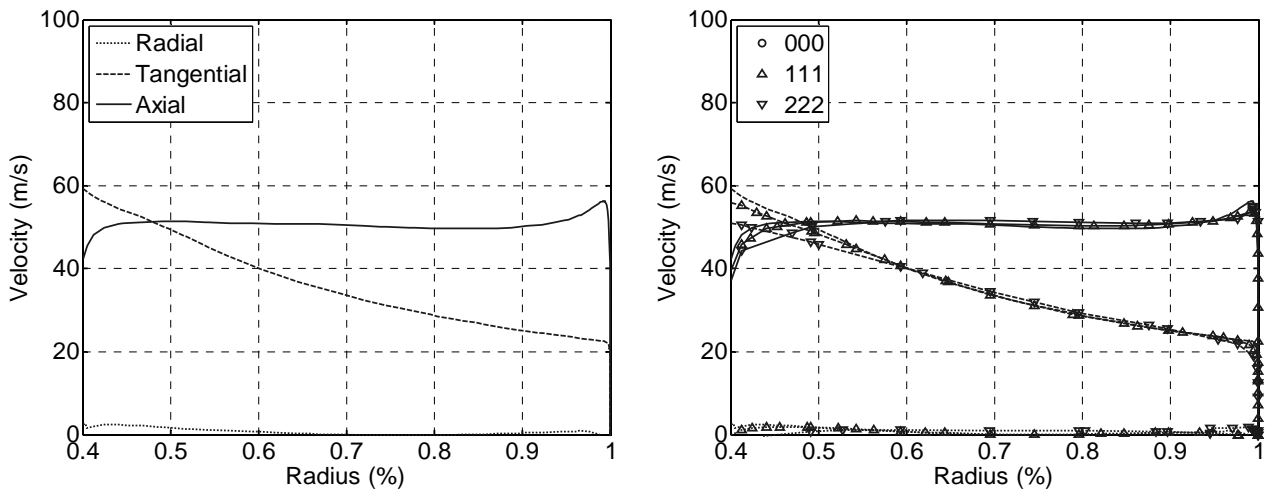


Figure 67: Rotor inlet flow velocity magnitude.

The axial flow is relatively constant but velocity increases at blade tip, a result of tip gap flow (Figure 67). The tangential flow component drops steadily from root to tip as a result of the decrease in IGV flow deflection. The radial component is as expected, negligible.

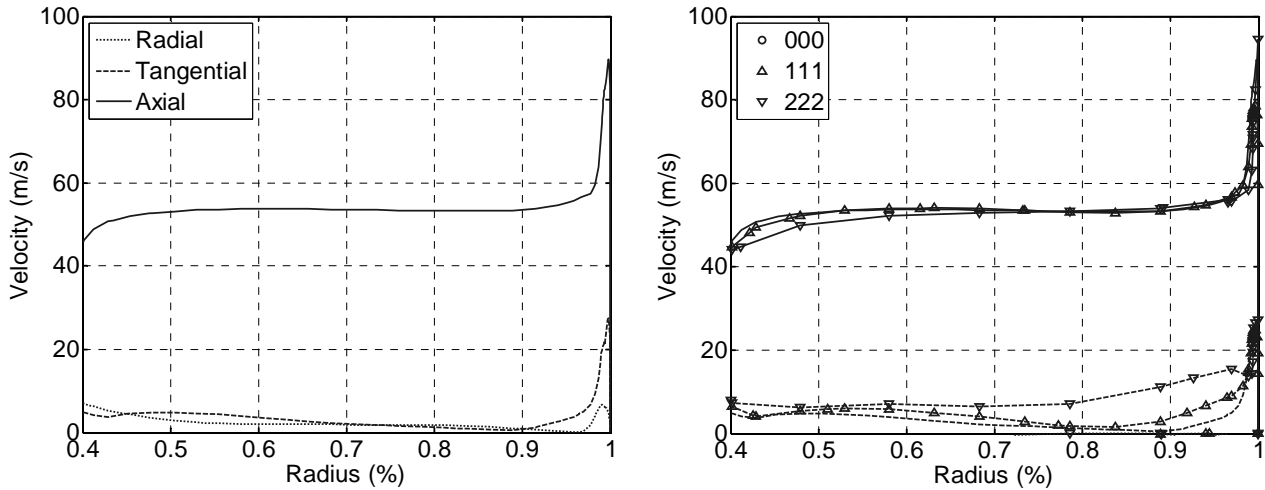


Figure 68: Turbine outlet flow velocity magnitude.

The axial flow characteristics can be explained in the same way as the first two stations (Figure 68). The tangential component is virtually zero, as a result of the design methodology ensuring axial outflow. All velocity components show a sharp increase at the tip as a result of the tip gap flow.

The flow angles calculated in the turbine design phase are used as secondary model validation method.

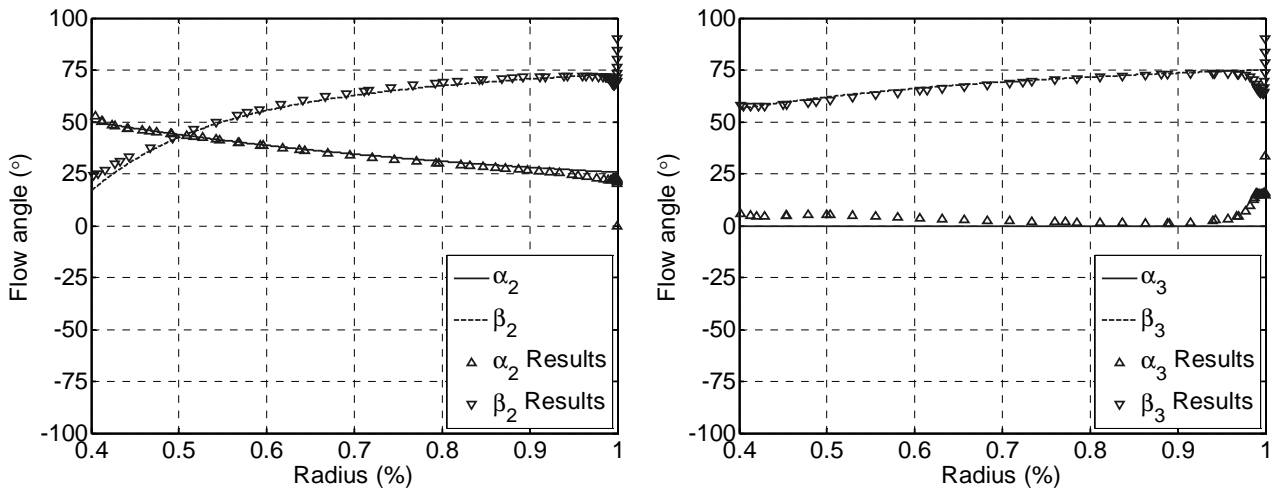


Figure 69: Turbine flow angles for station 2 and 3.

Throughout the blade span the numerical results follow the design well although flow angles deviate slightly close to hub and shroud. These deviations are believed to be as a result of wall effects and tip gap flow.

6.4.2. Off-design conditions

Off-design turbine performance is investigated as the SWEC will operate in an ever changing environment. Turbine performance is investigated for wave height variations.

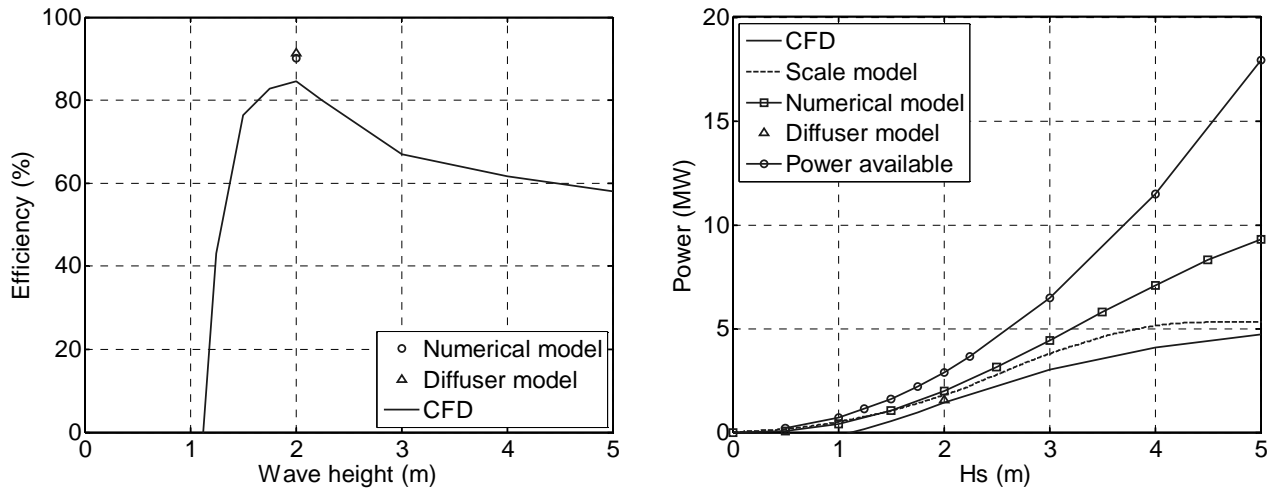


Figure 70: Turbine efficiency and power output.

The efficiency curve shown in Figure 70 indicates a dramatic drop off at wave heights less than 1.5m, so much so, that at these mild conditions negative efficiencies become evident. A drop off is less prevalent in wave conditions larger than 2m compared to the smaller wave conditions. The turbine is designed to rotate at constant speed. A variable speed approach would very likely have the effect of levelling off the efficiency curve to either side of the design wave height condition. Diffuser performance although discussed later can be seen to perform as predicted from the 2D model. The power curve tracks the initial estimates of power with reasonable accuracy (with only a 10 % error at a wave height of 2 m and 12 % at 3 m without diverging to a great degree in larger wave conditions). Also shown in the figure is the power available to the SWEC.

The turbine pressure drop shown in Figure 71 shows reasonable similarity to the values predicted during the 2D design phase as with the previous results. Flow rate is presented but as it is a boundary condition for CFD there is no comparison necessary.

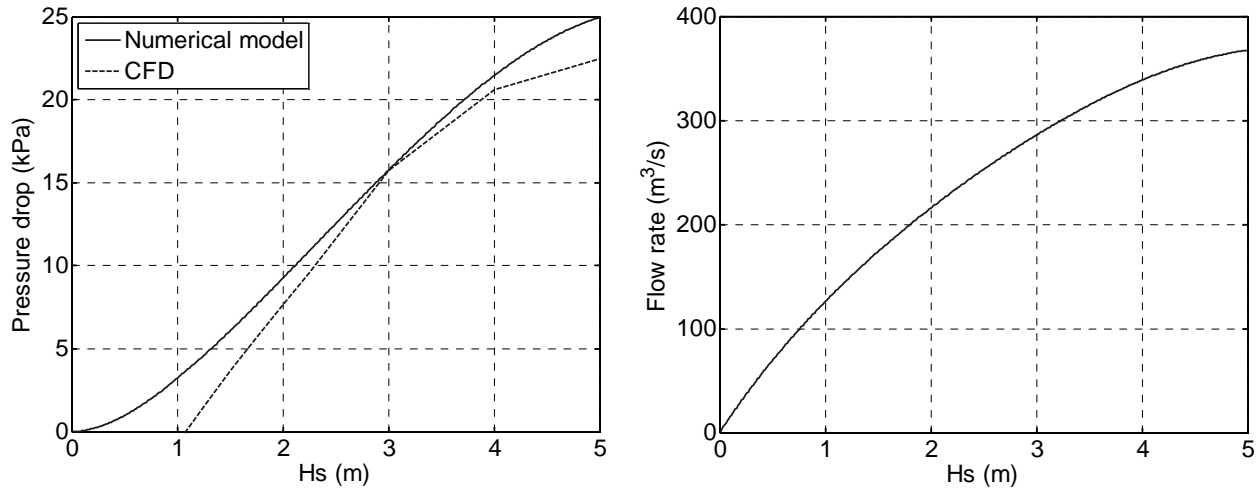


Figure 71: Turbine pressure drop and flow rate.

The blade profile performance is now investigated, being the primary device by which energy is extracted from the flow. It is important to ensure that the flow over the profiles is smooth and uniform. Figure 72 shows streamline plots of the design case and two extreme off design flow cases.

Blades perform well in 1m wave height condition (Figure 72). Only at the tip of the blade in the 2m condition do flow irregularities become apparent. The 4m wave condition shows that the majority of the blade is under a stalled flow condition. The flow at the blade root is still undisturbed as a result of the high solidity.

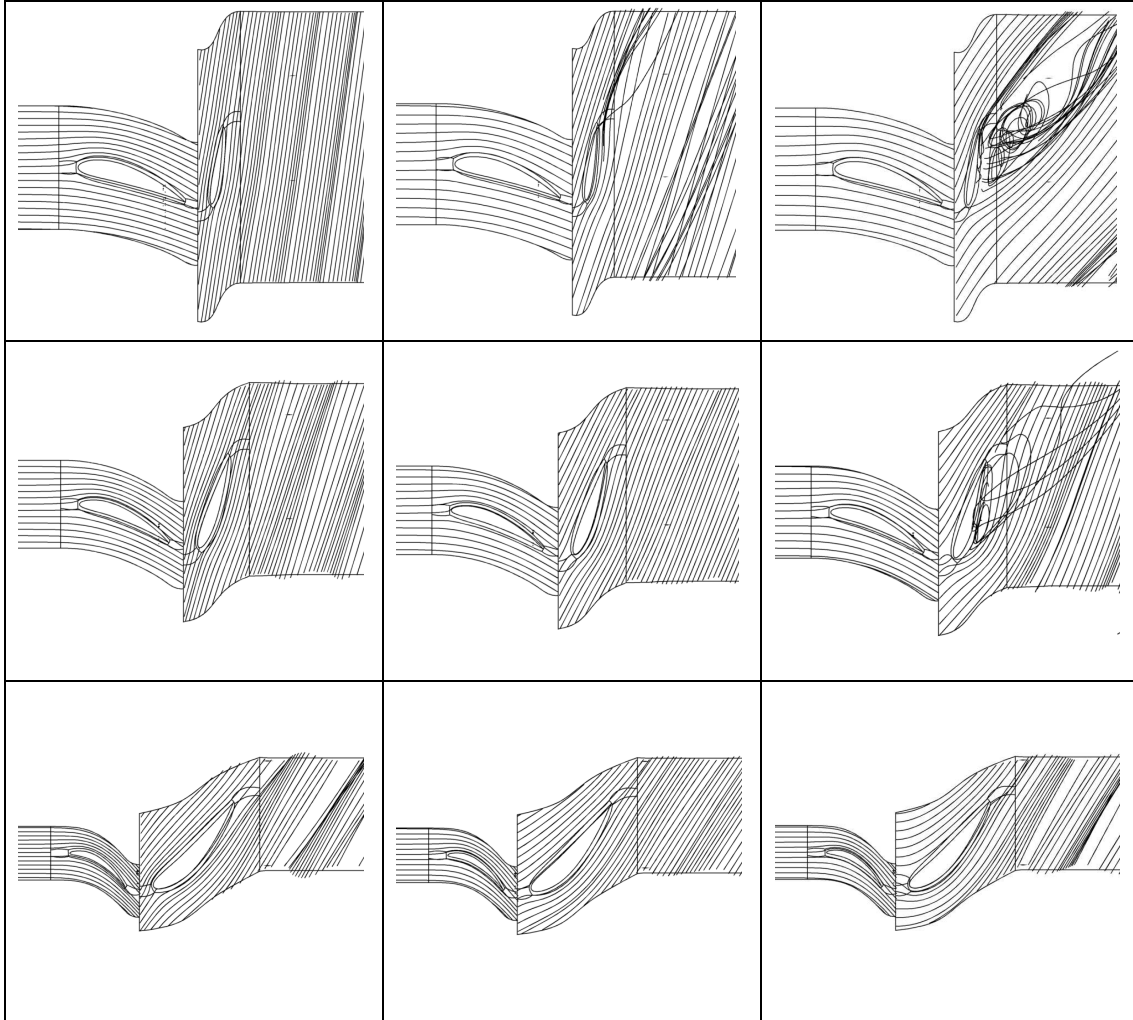


Figure 72: Profile section stream lines (95, 50 and 5% span, top to bottom), for 1, 2 and 4m Hs (left to right).

Figure 73 shows a meridian view of stream lines illustrating the effect of stall. The meridian view show that flow under a stalled condition tends to move toward shroud.

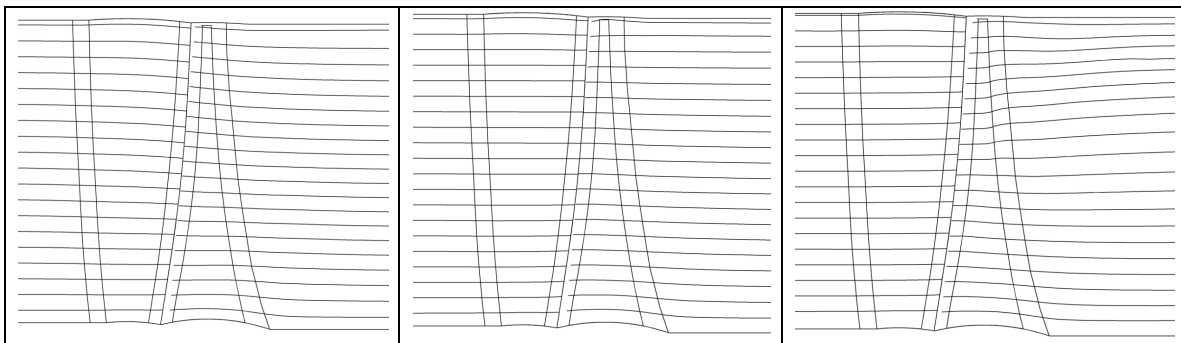


Figure 73: Meridian stream line plots for 1m, 2m, and 4m Hs conditions.

6.4.3. Diffuser performance

The main function of a diffuser is to recover static pressure whereby improving turbine performance. The efficiency is increased from 85% to 91% closely resembling the predicted performance of the 2D design algorithm, see Figure 70.

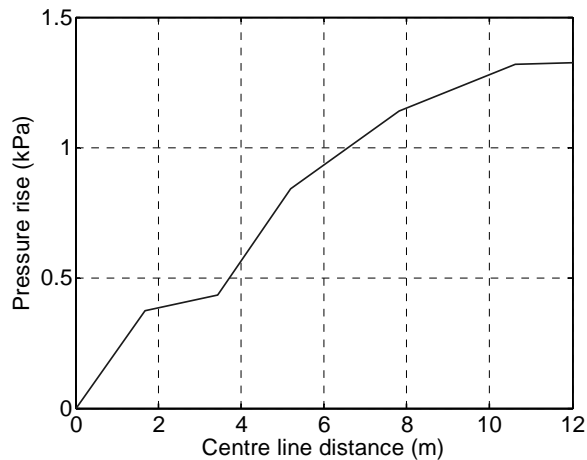


Figure 74: Static pressure recovery along the length of the diffuser.

Figure 74 shows that there is appreciable static pressure recovery through the diffuser. The deviation in pressure recovery curve at about 3.5m from the turbine is due to flow instabilities resulting from flow separation off the turbine hub.

6.4.4. Conversion efficiency

Figure 75 shows the conversion efficiency of wave power available to the SWEC to power available on the turbine shaft. The figure shows the expected drop in conversion efficiency at wave height exceeding 2m. The variable speed model (see the conclusions for further details on the recommended design) shows an improvement on the constant speed design. Figure 75 show overestimations of the 30% conversion efficiency quoted by Retief (2008) possible reasons for this include added mass and damping term inaccuracies, inaccuracies in wave model or scale model effects not apparent in experimentation becoming evident in full scale.

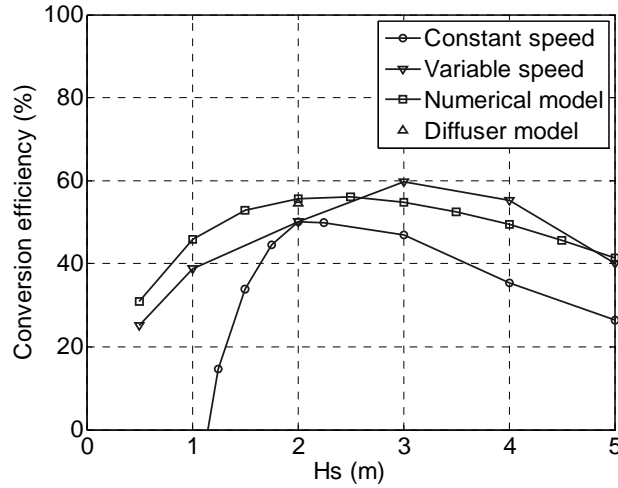


Figure 75: Predicted SWEC conversion efficiency.

6.5. Conclusion

CFD is a valuable tool in validating, highlighting areas of uncertainty and shortcomings of a design in an inexpensive manner. The design of the turbine is validated. Modelling of off-design conditions show the shortcomings of a constant speed approach, stall is evident at high flow rates and poor performance at low flow rates. Figure 76 shows improved performance with a variable speed approach. Speed is varied according a dimensionless group, Equation 73.

$$\frac{\dot{Q}_t}{NsD^3}$$

Equation 73

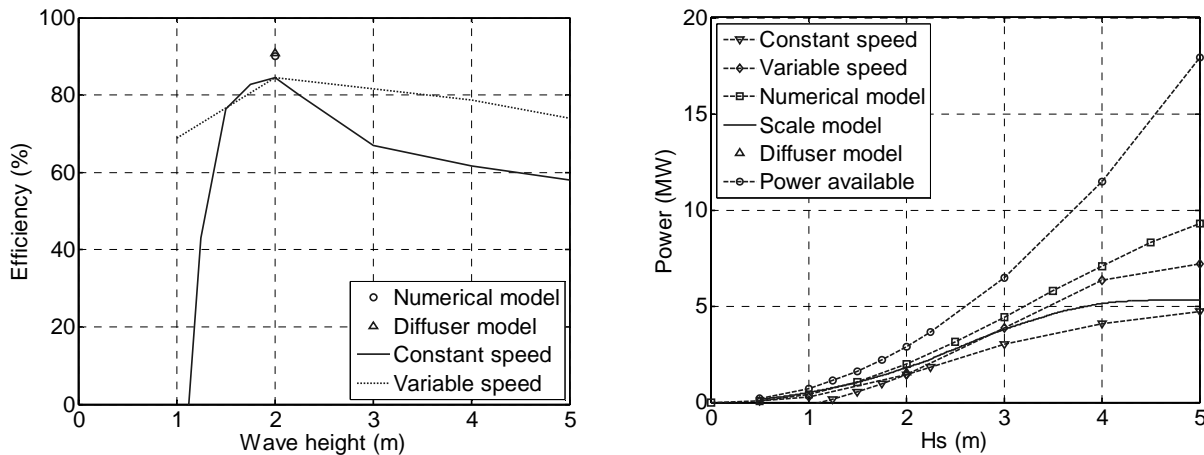


Figure 76: Turbine constant and variable speed performance variation.

7. Conclusions and recommendations

The completion of the project proves that a feasible turbine design is possible for operation in the SWEC. The airflow system numerical model predicted the SWEC's performance well for good estimates of added mass and damping.

The thesis focus areas include modelling of the airflow system and design and modelling of a turbine, the conclusions are divided accordingly. Major conclusions or recommendations will be stated, supported by a discussion and followed by further less important although not negligible statements.

7.1. Air flow system conclusions

The airflow system numerical simulation model predicted the SWEC performance well up to wave heights of 3m.

Model validity was proved by comparing results to experimental scale model results and by ensuring mass and energy conservation, as shown in the attached CD. The less accurate predictions of the model in larger wave conditions are believed to stem from inaccurate estimations of added mass and damping in these conditions. Nonetheless it is believed the model will be a valuable design tool, once accurate estimates for these terms have been determined for off-design conditions.

7.1.1. Sub-conclusions

The model is assembled in such a way that all structural dimensions can be varied. Added mass and damping terms can easily be modified once more accurate estimates become available or if the structure or orientation of the SWEC is changed.

7.2. Turbine design conclusions

The design is validated by modelling the turbine in CFD at the design condition. The turbine performed as expected producing power with efficiency of 90%.

Although the constant speed design performed well at the design condition, stall was predicted at higher flow rates and low efficiencies at lower flow rates. To combat these

design deficiencies a variable speed design was implemented and modelled, this had the effect of levelling off the turbine performance at off-design conditions.

7.2.1. Sub-conclusions

The diffuser performed as expected at design conditions, with a marked effect on turbine performance. Overall turbine efficiency is increased by 5%.

The hub design proved to be effective; the flow disturbances caused by the sharp end to the hub did not limit pressure recovery in the diffuser. It is believed that the hub design aids pressure recovery in the diffuser by flattening the flow velocity profile.

7.3. Air flow system recommendations

It is recommended that further system optimisation be done, for example if the collector arms were lengthened to equal the length of an average wave. This would smooth flow through the turbine and system ducting.

7.3.1. Sub-recommendations

The following should be done:

- A CFD study to investigate OWC dynamics under various wave conditions and orientations with respect to oncoming waves and to determine accurate estimates for added mass and damping terms in off design conditions.
- A CFD study modelling the full SWEC structure to determine the effect of interaction of the waves with the SWEC structure.
- A detailed investigation of the marine/wave environment in which SWEC will operate to determine an appropriate wave model.

7.4. Turbine design recommendations

Future work on the power conversion unit should include an experimental study on a scale model turbine, and an investigation of possible redesign of the turbine, implementing variable speed and blade stagger in either or both the IGV and rotor blade rows to improve off-design performance.

It has been shown that the implementation of a variable speed turbine design can greatly improve performance. It is believed that the implementation of variable or rotor blade stagger could stave off the onset of stall and thereby further improve performance.

7.4.1. Sub-recommendations

The following should be done:

- Further investigations should be made to optimise blade shape in order to lower profile losses and to investigate the effect of the tip gap on overall performance.
- The turbine module should undergo a full design process, proving structural integrity to survive while protruding the free surface.
- Generator design should be undertaken for optimal operation with a variable speed turbine which is subjected to continually varying flow conditions.

8. References

Airy, G. B. 1845. Tides and Waves, Encyc. Metrop., Article 192, pp 241-396.

Ambli, N, Bonke, K, Malmo, O, Reitan, A, 1982. The Kvaerner Multiresonant OWC. The Second International Symposium on Wave Energy Utilization, Trondheim, Norway.

Inventor by Autodesk <http://www.autodesk.co.za>.

Aungier. R. H, 2006, Turbine Aerodynamics Axial-Flow and Radial-Inflow Turbine Design and Analysis, ASME Press, New York, United States of America.

Balje, O. E., Turbomachines A guide to design, selection and theory, Wiley-Interscience, United States of America, 1981.

OERG., 1985, Stellenbosch Wave Energy Converter. Technical brochure presented at Hanover Trade Fair West Germany.

Brooke, J., Bhattacharyya, R., McCormick, M, E., Wave Energy Conversion, Elsevier Ocean Engineering Book Series Volume 6, ECOR.

Campbell, C, J., Oil Crisis, Multi – Science Publishing Co.

Cohen, R.H. Rogers, G.F.C. and Saravanamuttoo, H.I.H, 2001, Gas Turbine Theory, Fifth Edition, Prentice Hall, Essex, England.

Coastal engineering manual, 2006., United States Army Corp of Engineers.

Count, B, M, Evans, D, V, 1984. The influence of projecting sidewalls on the hydrodynamic performance of wave–energy Devices. Journal of fluid mechanics, Vol 145, pp 361-376.

Crowe, C, T, Elger, D, F, Roberson, J, A. 2001. Engineering Fluid Mechanics, Seventh Edition, Wiley and Sons, USA.

Cruz, J, 2008. Ocean Wave Energy Current Status and Future Perspectives, Springer, Bristol, United Kingdom.

Dean, R. G. and Dalrymple, R. A. 1991. Water Wave Mechanics for Engineers and Scientists, World Scientific Pub. Co., Teaneck, NJ.

OERG Design., 1983., SWEC Structural components.

OERG Design., 1983., SWEC Kostebesamings.

OERG Design., 1984., Design report.

Dixon, S.L. 1998, Fluid Mechanics and Thermodynamics of Turbo Machinery, Fourth Edition, Butterworths, England.

Evans, D, V, 1978. The Oscillating Water Column Wave–Energy Device. J. Inst. Maths Applics, 22, 423-433.

Evans, D, V, 1982. Wave-Power Absorber within a Resonant Harbor. The Second International Symposium on Wave Energy Utilization, Trondheim, Norway.

Falnes J (2005), presentation on wave energy for Noregs University.

Fine by NUMECA International, <http://www.numeca.com>

Fluri. T. F, 2008, Turbine Layout for and Optimisation of SolarChimney Power Conversion Units, PHd Thesis, University of Stellenbosch, South Africa.

Gannon, A.J. (2002). Solar Chimney Turbine Performance. Ph.D. thesis, University of Stellenbosch.

Godoy-Diana, R, Czitrom, S, P, R, 2007. On the tuning of a wave-energy driven oscillating-water-column seawater pump to polychromatic waves. Elsevier.

Gov, 2008, South African government guidelines for road transport legislation, 2008.

Hasselmann et al. 1973. Measurements of Wind-Wave Growth and Swell Decay during the Joint North Sea Wave Project (JONSWAP), Deutsche Hydrograph. Zeit., Ergänzungsheft Reihe A (80), No. 12.

Hasselmann, K. et al. 1976. "A Parametric Wave Prediction Model," Jour. Phys. Ocean., Vol 6, pp 200-228.

Horlock, J. H. 1966, Axial-flow Turbines, Butterworths. (1973 reprint with corrections), Huntington, New York: Krieger.

Idelchick, I, E, 1986, Handbook of Hydraulic Resistance, Second Edition, Revised and Augmented, Hemisphere Publishing Corporation, United States of America.

Japikse, D, Bains, N, C, 1994, Introduction to Turbomachinery, Oxford University Press, United States of America.

Joubert. J. R, 2008, An Investigation of the Wave Energy Resource on the South African Coast, Focusing on the Spatial Distribution of the South West Coast, Msc Thesis, University of Stellenbosch, South Africa.

Kim T, W. Kaneko K. Setoguchi T. Inoue M, 1988 Aerodynamic performance of an impulse turbine with self-pitch controlled guide vanes for wave power conversion. The Proceedings of first KSME-JSME Thermal and Fluid Engineering Conference 2, 133-137.

Kinishita, T, Masuda, K, Miyajima, S, Kato, W, 1985. Research of the System Simulation for a Fixed O.W.C Type Wave Energy Absorber. International Symposium on Ocean Space Utilization.

Kinsman, B. (1965). Wind Waves, Prentice-Hall, Englewood Cliffs, NJ.

Kline, S. J., Abbott, D. E., Fox, R. W. (1959). Optimum design of straight-walled diffusers. Trans. Am. SOC. Mech. Engrs., Series D, 81.

Lewis, R.I. 1996, Turbomachinery Performance Analysis, Arnold.

Maeda, H, Kinoshita, T, Masuda, K, Kato, W, 1984. Fundamental Research on Oscillating Water Column Wave Power Absorbers, OMAE Symposium.

Maeda, H, Masuda, K, Hayashi, H, 1984. Fundamental Research on Attenuator Type OWC Wave Energy Absorber, ECOR International Conference.

Maeda, H, Sanathakumar, S, Setoguchi, T, Takao, M, Kinoue, Y, Kaneko, K, 1999. Performance of an impulse turbine with fixed guide vanes for wave power conversion. Journal of Renewable Energy 17, 533-547.

Simulink by Mathworks, <http://www.mathworks.com>

Malmo, O, Reitan, A, 1985. Wave-power absorption by an oscillating water column in a channel, Journal of Fluid Mechanics, Vol 158, pp 153-175.

Malmo, O, Reitan, A, 1986. Wave-power absorption by an oscillating water column in a reflecting wall, Applied Ocean Research, Vol 8, No 1, pp 42-48.

Malmo, O, Reitan, A, 1986. Wave-power absorption by a finite row of oscillating water columns in a reflecting wall, Applied Ocean Research, Vol 8, No 2, pp 105-109.

Masami, S, Arakawa, C, 2005. Numerical Methods to Predict Characteristics of Oscillation Water Column for Terminator-type Wave Energy Converter, International Journal of Offshore and Polar Engineering, Vol 15, 4, 292-299.

Masuda, K, Maeda, H, Kato, W, 1981. Fundamental Study on the Air Turbine Type Wave Power Absorber, Work Shop Three Offshore Energy Resources Potential, ECOR, London.

Mei, C. C. 1991. The Applied Dynamics of Ocean Surface Waves, World Scientific Pub. Co., Teaneck, NJ.

Morrison., D., G., Geustyn., L., C., Zietsman., J., Horizontal forces on a submerged wave energy structure in shallow water, University of Stellenbosch, South Africa.

Müller., J., 1983., Besoek aan Howden SA BPK op 21 November 1983 I.V.M. Lugturbines. Ocean Engineering Research Group, Department of Civil Engineering, University of Stellenbosch, South Africa.

Newman, J. N, 1980. Marine Hydrodynamics, The MIT Press, Cambridge, Massachusetts, United States of America.

Pedersen., K. 2004. Excerpt from PRDW letter to Von Backström, T. W.

a) Pedersen., K. 2008. Technical drawing of SWEC Gravity Option (SWEC1).

Pierson, W. J., and Moskowitz, L. 1964, A Proposed Spectral Form for Fully-Developed Wind Sea Based on the Similarity Law of S. A. Kitaigorodskii, Journal of Geophysical Research, Vol 69, pp 5181-5203.

Raghunathan S, Tan, C, P, 1982, Aerodynamic Performance of the Wells Air Turbine. Journal of Energy, 7, 226-36.

Raghunathan S, 1985, Performance of the Wells self-rectifying turbine. Journal of Aeronautics, 89, 369-79.

Raghunathan S, 1995, The Wells air turbine for wave energy conversion. Prog Aerospace Sci, 31, 335-386.

Retief, G. de. F, Prestedge, G, K, Müller, F, P, J, 1982. A Proposal for wave energy conversion near Cape Town, 18th ICCE conference, Volme1: 245-260, Cape Town, South Africa.

Retief, G. de. F, Prestedge, G, K, Müller, F, P, J, 1983. Stellenbosch Wave Energy Converter (SWEC) Costs, Ocean Engineering Research Group, Department of Civil Engineering, University of Stellenbosch, South Africa.

Retief, G. de. F, Müller, F, P, J, Prestedge, G, K, Geustyn, L, C, Swart, D, H, 1984. Detailed design of a wave energy conversion plant, Ocean Engineering Research Group, Department of Civil Engineering, University of Stellenbosch, South Africa.

Retief, G. de. F, Müller, F, P, J, Geustyn, L, C, Morrison, D, G, 1985. The Stellenbosch Wave Energy Converter (SWEC), Ocean Engineering Research Group, Department of Civil Engineering, University of Stellenbosch, South Africa.

a) Retief, G. de. F, Müller, F, P, J, 1985. Wave Energy Development at the University of Stellenbosch, Ocean Engineering Research Group, Department of Civil Engineering, University of Stellenbosch, South Africa.

b) Retief, G. de. F, Prestedge, G, K, Müller, F, P, J, 1985, A Proposal for wave energy conversion near Cape Town. presented at Hanover Trade Fair West Germany, Cape Town, South Africa.

Retief, G. de. F, Müller, F, P, J, 1986. Wave energy potential of Southern Africa, Chapter 14, Wave Power.

Retief, G. 2006. Wave power in the Western Cape [Presentation].

Retief, G. 2008. Personal communication.

Runstadler, P, W., Dolan, F, X., Dean, R, C. (1975). Diffuser data book. Create Science and Technology, Hanover, New Hampshire.

Ross, D, 1995, Power from the waves, Oxford University Press, New York, United States of America.

Sayers, A, T. 1990. Hydraulic and Compressible Flow Turbomachines, University of Cape Town. South Africa.

Setoguchi, T, Kinoue, Y, Kaneko, K, Santhakumar, S, Inoue, M, 2000, Study on an Impulse Turbine for wave energy conversion. International Journal of Offshore and Polar Engineering, 10, 355-62.

Setoguchi, T, Kinoue, Y, Kim, T, H Kaneko, K, Inoue, M, 2003, Hysteresis of Wells turbine for wave energy power conversion. Journal of Renewable Energy 28, 2113-2127.
Sjolander, S. A. Overview of tip-clearance effects in axial turbines, VKI Lecture Series, 1997-01, 1997.

Smith, M, J, 2003, Improved Added Mass and Wet Modes Calculation for Naval Structures. Defence Research and Development Canada-Atlantic. Canada.

Sovran, G., Klomp, E. (1967). Experimentally determined optimum geometries for rectilinear diffusers with rectangular, conical and annular cross-sections. Fluid Mechanics of Internal Flow, Elsevier, 270-319.

Stodola, A. 1945. Steam and Gas Turbines. P. Smith.

Stokes, G. G. 1847. On the Theory of Oscillatory Waves, Trans. Camb. Phil. Soc., Vol 8, pp 441-455.

Stokes, G. G. 1880. Math. Phys. Papers, Vol 1, Camb. Univ. Press.

Suzuki, M, Arakawa, C, 2005, Numerical Methods to Predict Characteristics of Oscillating Water Column for Terminator-type Wave Energy Converter. International Journal of Offshore and Polar Engineering, Vol 15, No 4, 292-299.

Tagori, R, Arakawa, C, Suzuki, M, 1987, Estimation of prototype performance and optimum design of Wells turbine. Res Nat Energy SPEY, 20, 127-132.

Thakker, A, Dhanasekaran, T, S, Ryan, J, 2005, Experimental studies on the effect of guide vane shape on performance of impulse turbine for wave energy conversion. *Journal of Renewable Energy* 30, 2203-2219.

a) Thakker, A, Dhanasekaran, T, S, Ryan, J, 2005, Experimental and computational analysis on guide vane losses of impulse turbine for wave energy conversion. *Journal of Renewable Energy* 30, 1359-1372.

Thorpe. T, W, 1999, *Wave power: moving towards commercial Viability*, Broadway House, London.

Von Backström, T. W., Gannon, A. J., 2003. Solar chimney turbine characteristics. *ASME Journal of Solar Energy Engineering* 76, 235-241.

Voutilainen, V. (2004 November). Private communication with ABB Finland. Cited on page 65 in Fluri (2008)

Wei, L, Weiyang, Q, Dawei, S. Tip Clearance Flows in Turbine Cascades. *Chinese Journal of Aeronautics*, 21. 193-199.

Ingham, 2009,. www.dur.ac.uk.

Appendix A: SWEC dimensional discrepancies.

This appendix is aimed at defining the dimensions of the SWEC. During the design process numerous design options were evaluated. A summary of all the design documentation is presented. A final set of dimensions for SWEC is determined.

A1) System layout

Figure A1 describes all the basic dimensions of the modules and the orientation of the arms with respect to the shore.

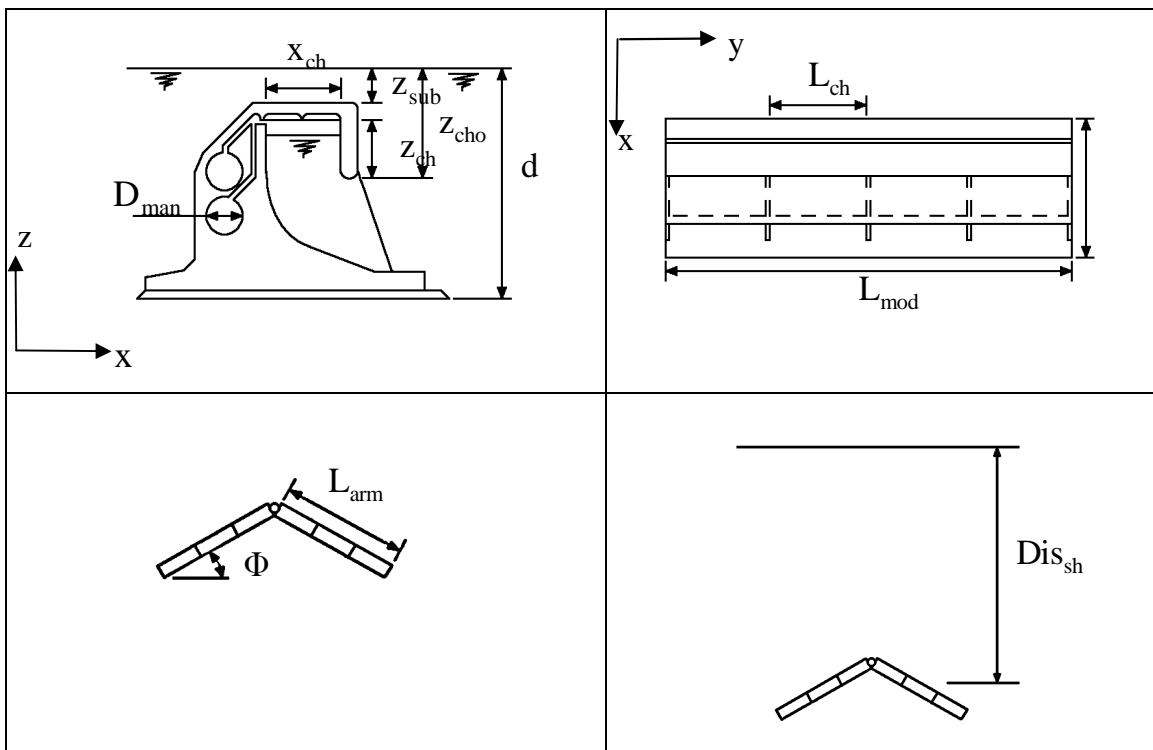


Figure A1: Cross-section through OWC chamber, Top view of a module, Top view of SWEC, SWEC orientation with respect to shoreline.

Where design documents show no reference to certain aspects of the design Retief (2008) was consulted.

A1.1. OWC chamber

Table A1: OWC Chamber dimensional discrepancies.

Dimension	Description	Value	Reference
D_{man}	HP and LP manifold duct diameter.	2.5m	Pedersen (2008a)
		2.5m	Retief (1984)
x_{ch}	Breadth (Inner) of an OWC chamber.	6m	Pedersen (2008a)
z_{sub}	Submergence.	2m	Retief (1985)
		2m	Retief (1986)
		2m	Retief (1985a)
		2m	Retief (1984)
		2.5-4.5m	Design (1984)
		2.5-4.5m	Design (1982)
z_{cho}	SWL line to Chamber opening.	5.5m	Pedersen (2008a)
z_{ch}	Height of an OWC chamber.	3.5m	Design (1984)
		3.5m	Pedersen, 2008a
d	Water depth.	14m	Retief (1985)
		15-20m	Retief (2006)
		15-20m	Retief (1985b)
		14m	Retief (1986)
		13m	Morrison (1985)
		14m	Brochure (1985)
		13m	Morrison (1985)
		14m	Retief (1985a)
		14m	Retief (1984)
		12.5-16m	Design (1984)
		15m	Müller (1983)
		12.5-16m	Design (1982)

A1.2. Module plan

Table A2: SWEC module dimensional discrepancies.

Dimension	Description	Value	Reference
L_{ch}	Length of a OWC chamber	12m	Pedersen (2008a)
		15m	Retief (1983)
L_{mod}	Length of a module	53m	Retief (1985)
		50	Retief (1985b)
		53m	Retief (1986)
		53m	Retief (1984)
		15m	Retief (1982)
		70m	Design (1982)
N_{ch}	Number of chambers in each precast	4	Retief (1984)

A1.3. Orientation of arms

The length of the arms and the angle at which they are set is important as this determines the way in which waves interact with the structure. The length of the arm has a great effect on the characteristics of the flow through the turbine.

Angle at which the arms are set determines the relative wave length which SWEC experiences. The smaller the angle the greater the relative wave length, hence the more power available to capture (power is proportional to wave length).

Table A3: Overall SWEC dimensional discrepancies.

Dimension	Description	Value	Reference		
Φ	Angle of arm to the oncoming swell.	45°	Retief (1985b)		
		45°	Retief, 1986)		
		45°	Retief (1985)		
		45°	Brochure (1985)		
		45°	Retief (1985a)		
		45°	Retief (1984)		
		45°	Retief (1983)		
		30°	Design (1983)		
		30°	Retief (1982)		
		L_{arm}	Length of arm.	300m	Retief (2006)
160m	Retief (1986)				
160m	Retief (1985)				
160m	Retief (1984)				
250-300m	Müller (1983)				
240m	Retief (1983)				
240m	Design (1983)				
300m	Retief (1982)				
N_{mod}	Number of modules per arm.			3	Retief (1984)
N_{ch}	Number of chambers in each arm			12	Pedersen (2008a)
		12	Retief (1984)		
		10	Design (1984)		
		16	Retief (1983)		

A1.4. Orientation of SWEC with respect to shore

Distance from shore determines the length of cabling needed to transmit power.

Table A4: Discrepancy in the position of SWEC off shore.

Dimension	Description	Value	Reference
Dis_{sh}	Energy converter distance to shore.	1.5km	Retief (1985)
		1.5km	Retief (1986)
		1.5km	Retief (1985)
		1.5km	Brochure (1985)
		1.5km	Retief (1985a)
		1.5km	Retief (1984)

A1.5. Original description of turbine

Although turbine design is an objective of the thesis, initial turbine specifications found are useful in developing constraints for the current design.

Table A5: Original turbine specifications.

Dimension	Description	Value	Reference
D_t	Turbine diameter.	3.5m	Retief (1985)
		3.5m	Retief (1986)
		3 m	Retief (1985)
		3.5m	Retief (1985a)
		3.5m	Retief (1984)
		4m	Retief (1983)
L_t	Turbine length	8m	Retief (1985)
		8m	Retief (1986)
		8m	Retief (1985a)
		8m	Retief (1984)
		1.3m	Retief (1983)
N_s	Turbine rotational speed	500rpm	Pedersen (2008)
Δp_t	Pressure drop over turbine	7.5kPa	Pedersen (2008)
Q_t	Flow through turbine	450m ³ /s	Pedersen (2008)
τ	Wave period	12.3s	Retief (1984)

A2. Final dimension set

Most frequently quoted dimensions were chosen and Retief (2008) was consulted on the less clearly defined quantities.

Table A6: Final SWEC dimension set

Dimension	Value
D_{man}	3m
x_{ch}	6m
z_{sub}	2m
z_{cho}	5.5m
z_{ch}	3m
d	15-20m
L_{ch}	12m
L_{mod}	53.33m
N_{ch}	4
Φ	45°
L_{arm}	160m
N_{mod}	3
N_{ch}	12
Dis_{sh}	1.5km

Appendix B: Derivation of SWEC state equations.

A description of the governing equations, formulated to describe flows in the SWEC is presented.

B1. Introduction

The equations derived in each section describe the flow in and through CVs which are linked, described and solved in block diagram format. The CVs are described below.

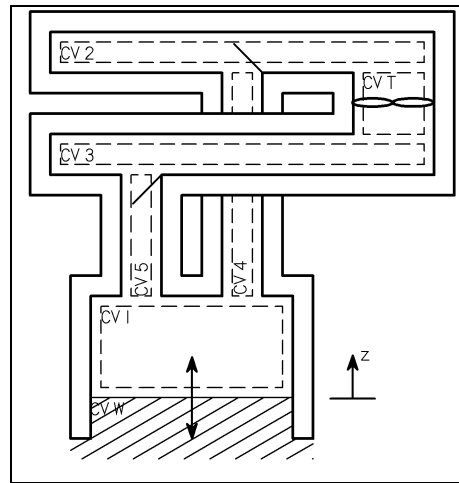


Figure B1: SWEC CV layout.

CV 1 is subject to pressure fluctuations as a result of the OWC motion. These fluctuations control flow through connecting ducts CV 4 and CV 5. CV 2 receives flow from CV 1 (via CV 4) and supplies air to the turbine (CV T). CV 3 supplying air to CV 1 (via CV 5). CV T represents the turbine flow. CV W describes the OWC motion. CV 4 facilitates only outflow and CV 5 inflow with respect to CV 1, Figure B1.

B2. Model layout

Figure B1 shows various CVs and their positions in relation to one another, the interaction between CVs and flow within them is explained by means of a set of state equations.

B2.1. CV 1:

CV 1 flow is described by augmentation of the continuity, ideal gas law and a pipe flow relations.

B2.1.1. Continuity equation

$$\frac{d}{dt} \int_{\forall_1} \rho_1 d\forall_1 + \int_{A_{i,o}} \rho_{i,o} V_{i,o} dA_{i,o} = 0 \quad \text{Equation C1}$$

Accumulation term:

$$\frac{d}{dt} \int_{\forall_1} \rho_1 d\forall_1 = \frac{d}{dt} \rho_1 \forall_1 \quad \text{Equation C2}$$

$$\frac{d}{dt} \rho_1 \forall_1 = \frac{dm_1}{dt} = \dot{m}_1 \quad \text{Equation C3}$$

Boundary flow term:

$$\int_{A_{i,o}} \rho_{i,o} V_{i,o} dA_{i,o} = \rho_{i,o} V_{i,o} A_{i,o} \quad \text{Equation C4}$$

$$\rho_{i,o} V_{i,o} A_{i,o} = \frac{dm_{i,o}}{dt} = \dot{m}_{i,o} \quad \text{Equation C5}$$

Formulation:

$$\dot{m}_1 = -\dot{m}_o \quad \text{Equation C6}$$

B2.1.2. Equation of state (ideal gas law):

$$P_1 \forall_1 = m_1 R T_1 \quad \text{Equation C7}$$

Taking the natural logarithm of both sides of the equation yields the following.

$$\ln P_1 + \ln \forall_1 = \ln m_1 + \ln R + \ln T_1 \quad \text{Equation C8}$$

Differentiating Equation C8 with respect to time yields a relation defining the rate of change of pressure with respect to change in mass and volume.

$$\frac{1}{P_1} \frac{dP_1}{dt} + \frac{1}{\forall_1} \frac{d\forall_1}{dt} = \frac{1}{m_1} \frac{dm_1}{dt} + \frac{1}{R} \frac{dR}{dt} + \frac{1}{T_1} \frac{dT_1}{dt} \quad \text{Equation C9}$$

$$\frac{dP_1}{dt} = P_1 \left[\frac{1}{m_1} \frac{dm_1}{dt} - \frac{1}{\forall_1} \frac{d\forall_1}{dt} \right] \quad \text{Equation C10}$$

$$\dot{P}_1 = P_1 \left[\frac{\dot{m}_1}{m_1} - \frac{\dot{\forall}_1}{\forall_1} \right] \quad \text{Equation C11}$$

Volume term:

$$\frac{\dot{\forall}_1}{\forall_1} = \frac{-\dot{z} A_1}{(H_1 - z) A_1} \quad \text{Equation C12}$$

Mass term:

$$\dot{m}_1 = -\dot{z}\rho_1 A_1 = -\dot{m}_o \quad \text{Equation C13}$$

$$\frac{\dot{m}_1}{m_1} = \frac{-\dot{z}\rho_1 A_1}{(H_1 - z)\rho_1 A_1} \quad \text{Equation C14}$$

Formulation:

$$\dot{P}_1 = \frac{P_1}{(H_1 - z)A_1} \left[\dot{z}A_1 - \frac{\dot{m}_o}{\rho_1} \right] \quad \text{Equation C15}$$

B2.1.3. Flow from CV 1 through CV4:

Pipe flow equation (Crowe, 2001) governs mass flow in and out CV 1. Outflow is defined as positive and inflow negative. Various mechanisms for loss are implemented.

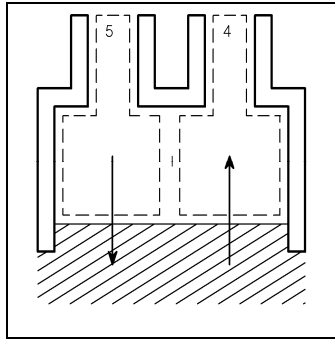


Figure B2: Pipe flow equation domain depending on OWC motion.

Pipe flow equation general format expressed with all terms:

$$P_1 + \frac{\rho_1 V_1^2}{2} + z_1 = P_{4,5} + \frac{\rho_{4,5} V_{4,5}^2}{2} + z_{4,5} + \rho_{4,5} g \sum h_L \quad \text{Equation C16}$$

Elevation terms are deemed insignificant relative to the other terms.

$$P_1 + \frac{\rho_1 V_1^2}{2} + \cancel{z_1} = P_{4,5} + \frac{\rho_{4,5} V_{4,5}^2}{2} + \cancel{z_{4,5}} + \rho_{4,5} g \left(f \frac{L_{4,5}}{D_{4,5}} \frac{V_{4,5}^2}{2g} + K_C \frac{V_{4,5}^2}{2g} + K_E \frac{V_{4,5}^2}{2g} \right) \quad \text{Equation C17}$$

$$V = \frac{\dot{m}}{A\rho} \quad \text{Equation C18}$$

$$P_1 + \frac{\rho_1}{2} \left[\frac{\dot{m}_1}{A_1 \rho_1} \right]^2 = P_{4,5} + \frac{\rho_{4,5}}{2} \left[\frac{\dot{m}_{4,5}}{A_{4,5} \rho_{4,5}} \right]^2 \left[1 + f \frac{L_{4,5}}{D_{4,5}} + K_C + K_E \right] \quad \text{Equation C19}$$

The following definitions are known from continuity and by the assumption that duct properties are equal to those of HP and LP manifolds to which they are connected.

$$\dot{m}_{4,5} = \dot{m}_{i,o} \quad \text{Equation C20}$$

$$\dot{m}_1 = -\dot{m}_{i,o} \quad \text{Equation C21}$$

$$A_{4,5} \rho_{4,5} = A_{i,o} \rho_{i,o} \quad \text{Equation C22}$$

$$P_{4,5} = P_{i,o} \quad \text{Equation C23}$$

The pipe flow equation becomes:

$$P_1 + \frac{\rho_1}{2} \left[\frac{-\dot{m}_{i,o}}{A_1 \rho_1} \right]^2 = P_{i,o} + \frac{\rho_{i,o}}{2} \left[\frac{\dot{m}_{i,o}}{A_{i,o} \rho_{i,o}} \right]^2 \left[1 + f \frac{L_{i,o}}{D_{i,o}} + K_C + K_E \right] \quad \text{Equation C24}$$

$$P_1 - P_{i,o} = \frac{\rho_{i,o}}{2} \left[\frac{\dot{m}_{i,o}}{A_{i,o} \rho_{i,o}} \right]^2 \left[1 + f \frac{L_{i,o}}{D_{i,o}} + K_C + K_E \right] - \frac{\rho_1}{2} \left[\frac{\dot{m}_{i,o}}{A_1 \rho_1} \right]^2 \quad \text{Equation C25}$$

$$\dot{m}_{i,o} = \sqrt{2(P_1 - P_{i,o}) / \left(\rho_{i,o} \left[1/A_{i,o} \rho_{i,o} \right]^2 \left[1 + f L_{i,o}/D_{i,o} + K_C + K_E \right] - \rho_1 \left[1/A_1 \rho_1 \right]^2 \right)} \quad \text{Equation C26}$$

B2.2. CV 2:

Flow through CV 2 is described by augmenting the continuity and ideal gas laws.

B2.2.1. Continuity equation

$$\frac{d}{dt} \int_{\forall_2} \rho_2 d\forall_2 + \int_{A_{i,o}} \rho_{i,o} V_{i,o} dA_{i,o} = 0 \quad \text{Equation C27}$$

Accumulation term:

$$\frac{d}{dt} \int_{\forall_2} \rho_2 d\forall_2 = \frac{d}{dt} \rho_2 \forall_2 \quad \text{Equation C28}$$

$$\frac{d}{dt} \rho_2 \forall_2 = \frac{dm_2}{dt} = \dot{m}_2 \quad \text{Equation C29}$$

Boundary flow term:

$$\int_{A_{i,o}} \rho_{i,o} V_{i,o} dA_{i,o} = \rho_{ti} V_{ti} A_{ti} - \rho_i V_i A_i \quad \text{Equation C30}$$

$$\rho_{ti} V_{ti} A_{ti} - \rho_i V_i A_i = \frac{dm_{ti}}{dt} - \frac{dm_i}{dt} = \dot{m}_{ti} - \dot{m}_i \quad \text{Equation C31}$$

Formulation:

$$\dot{m}_2 = \dot{m}_o - \dot{m}_{ti} \quad \text{Equation C32}$$

B2.2.2. Equation of state (ideal gas law):

$$P_2 \nabla_2 = m_2 R T_2 \quad \text{Equation C33}$$

Taking the natural logarithm of both sides of the equation yields the following.

$$\ln P_2 + \ln \nabla_2 = \ln m_2 + \ln R + \ln T_2 \quad \text{Equation C34}$$

Differentiating Equation C34 with respect to time yields a relation defining the rate of change of pressure with respect to change in mass.

$$\frac{1}{P_2} \frac{dP_2}{dt} + \frac{1}{\nabla_2} \frac{d\nabla_2}{dt} = \frac{1}{m_2} \frac{dm_2}{dt} + \frac{1}{R} \frac{dR}{dt} + \frac{1}{T_2} \frac{dT_2}{dt} \quad \text{Equation C35}$$

$$\frac{dP_2}{dt} = P_2 \left[\frac{1}{m_2} \frac{dm_2}{dt} \right] \quad \text{Equation C36}$$

$$\dot{P}_2 = P_2 \left[\frac{\dot{m}_2}{m_2} \right] \quad \text{Equation C37}$$

Mass term:

$$\dot{m}_2 = \dot{m}_o - \dot{m}_{ti} \quad \text{Equation C38}$$

$$\frac{\dot{m}_2}{m_2} = \frac{\dot{m}_o - \dot{m}_{ti}}{\rho_2 \nabla_2} \quad \text{Equation C39}$$

Formulation:

$$\dot{P}_2 = P_2 \left[\frac{(\dot{m}_o - \dot{m}_{ti})}{\rho_2 \nabla_2} \right] \quad \text{Equation C40}$$

B2.3. CV 3:

Flow in, leaving or entering CV 3 described by augmenting the continuity and ideal gas laws. Subscript i and o represent flow entering (CV T) and leaving (CV 5).

B2.3.1. Continuity equation

$$\frac{d}{dt} \int_{\nabla_3} \rho_3 d\nabla_3 + \int_{A_{i,o}} \rho_{i,o} V_{i,o} dA_{i,o} = 0 \quad \text{Equation C41}$$

Accumulation term:

$$\frac{d}{dt} \int_{V_3} \rho_3 dV_3 = \frac{d}{dt} \rho_3 V_3 \quad \text{Equation C42}$$

$$\frac{d}{dt} \rho_3 V_3 = \frac{dm_3}{dt} = \dot{m}_3 \quad \text{Equation C43}$$

Boundary flow term:

$$\int_{A_{i,o}} \rho_{i,o} V_{i,o} dA_{i,o} = \rho_o V_o A_o - \rho_{to} V_{to} A_{to} \quad \text{Equation C44}$$

$$\rho_o V_o A_o - \rho_{to} V_{to} A_{to} = \frac{dm_o}{dt} - \frac{dm_{to}}{dt} = \dot{m}_o - \dot{m}_{to} \quad \text{Equation C45}$$

Formulation:

$$\dot{m}_3 = -\dot{m}_o + \dot{m}_{to} \quad \text{Equation C46}$$

B2.3.2. Equation of state (ideal gas law):

$$P_3 V_3 = m_3 R T_3 \quad \text{Equation C47}$$

Taking the natural logarithm of both sides of the equation yields the following.

$$\ln P_3 + \ln V_3 = \ln m_3 + \ln R + \ln T_3 \quad \text{Equation C48}$$

Differentiating Equation C48 with respect to time yields a relation defining the rate of change of pressure with respect to change in mass.

$$\frac{1}{P_3} \frac{dP_3}{dt} + \frac{1}{V_3} \frac{dV_3}{dt} = \frac{1}{m_3} \frac{dm_3}{dt} + \frac{1}{R} \frac{dR}{dt} + \frac{1}{T_3} \frac{dT_3}{dt} \quad \text{Equation C49}$$

$$\frac{dP_3}{dt} = P_3 \left[\frac{1}{m_3} \frac{dm_3}{dt} \right] \quad \text{Equation C50}$$

$$\dot{P}_3 = P_3 \left[\frac{\dot{m}_3}{m_3} \right] \quad \text{Equation C51}$$

Mass term:

$$\dot{m}_3 = \dot{m}_{to} - \dot{m}_o \quad \text{Equation C52}$$

$$\frac{\dot{m}_3}{m_3} = \frac{\dot{m}_{to} - \dot{m}_o}{\rho_3 V_3} \quad \text{Equation C53}$$

Formulation:

$$\dot{P}_3 = P_3 \left[\frac{\dot{m}_{to} - \dot{m}_o}{\rho_3 \nabla_3} \right] \quad \text{Equation C54}$$

B2.4. CV T

The operation of the turbine is governed by the ellipse law first presented by Stodola (1945) and according to Dixon (1998) reads as in Equation C55.

$$\dot{m}_t \sqrt{T_{ti}} / P_{ti} = k_t \left[1 - (P_{to}/P_{ti})^2 \right]^{1/2} \quad \text{Equation C55}$$

This relates mass flow through a turbine to the total pressure ratio. The constant k_t defines this relation and indirectly the design of the turbine. The relation is augmented to calculate turbine mass flow.

$$\dot{m}_t = k_t \frac{P_{ti}}{\sqrt{T_{ti}}} \left[1 - (P_{to}/P_{ti})^2 \right]^{1/2} \quad \text{Equation C56}$$

B2.5. CV W

OWC motion forces air into and draws it from ducting supplying the turbine, Figure B3. Continuity and momentum equation are augmented to describe the motion of the OWC.

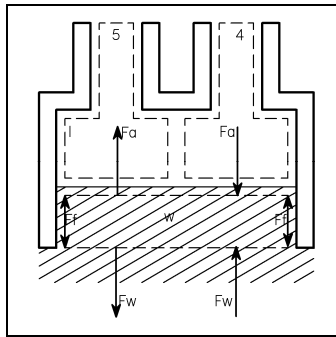


Figure B3: FBD of an OWC of a single SWEC chamber.

B2.5.1. Continuity equation:

$$\frac{d}{dt} \int_{\nabla_w} \rho_w d\nabla_w + \int_{A_{wi,o}} \rho_{wi,o} V_{wi,o} dA_{wi,o} = 0 \quad \text{Equation C57}$$

Accumulation term:

$$\frac{d}{dt} \int_{\nabla_w} \rho_w d\nabla_w = \frac{d}{dt} \rho_w \nabla_w \quad \text{Equation C58}$$

$$\frac{d}{dt} \rho_w \nabla_w = \frac{dm_w}{dt} = \dot{m}_w \quad \text{Equation C59}$$

Boundary flow term:

$$\int_{A_{wi,o}} \rho_{wi,o} V_{wi,o} dA_{wi,o} = -\rho_{wi,o} V_{wi,o} A_{wi,o} \quad \text{Equation C60}$$

$$\rho_{wi,o} V_{wi,o} A_{wi,o} = \frac{dm_{wi,o}}{dt} = \dot{m}_{wi,o} \quad \text{Equation C61}$$

Formulation:

$$\dot{m}_w = -\dot{m}_{wi,o} \quad \text{Equation C62}$$

B2.5.2. Momentum equation:

$$\sum F_z = \frac{d}{dt} \int_{\nabla_w} V_w \rho_w d\nabla_w + \int_{A_{wi,o}} V_{wi,o} \rho_{wi,o} V_{wi,o} dA_{wi,o} \quad \text{Equation C63}$$

Accumulation term:

$$\frac{d}{dt} \int_{\nabla_w} V_w \rho_w d\nabla_w = \frac{d}{dt} V_w \rho_w \nabla_w \quad \text{Equation C64}$$

$$\frac{d}{dt} V_w \rho_w \nabla_w = \frac{d}{dt} V_w m_w \quad \text{Equation C65}$$

$$\frac{d}{dt} V_w m_w = V_w \frac{dm_w}{dt} + m_w \frac{dV_w}{dt} = V_w \dot{m}_w + m_w \dot{V}_w \quad \text{Equation C66}$$

Boundary flow term:

$$\int_{A_{wi,o}} V_{wi,o} \rho_{wi,o} V_{wi,o} dA_{wi,o} = -V_{wi,o} \rho_{wi,o} V_{wi,o} A_{wi,o} \quad \text{Equation C67}$$

$$-V_{wi,o} \rho_{wi,o} V_{wi,o} A_{wi,o} = -V_{wi,o} \frac{dm_{wi,o}}{dt} = -V_{wi,o} \dot{m}_{wi,o} \quad \text{Equation C68}$$

Force terms:

$$\sum F_z = F_w - F_a - F_B - F_f \quad \text{Equation C69}$$

Expanding force terms yields the following:

$$F_w = p_w A_{wi,o} \quad \text{Equation C70}$$

$$F_a = p_1 A_1 \quad \text{Equation C71}$$

$$F_B = \rho_w g (H_w + z) A_1 \quad \text{Equation C72}$$

$$F_f = \rho_w \frac{f_1}{4} \frac{V_w^2}{2} \quad \text{Equation C73}$$

Friction force

Flow in the OWC is assumed laminar. The following relation is valid (Crowe, 2001).

$$f_1 = \frac{64}{\text{Re}} \quad \text{Equation C74}$$

The term can be expanded can then be expanded.

$$\frac{64}{\text{Re}} = \frac{64\mu_w}{\rho_w V_w D_{hl}} \quad \text{Equation C75}$$

$$D_{hl} = \frac{4A_1}{\text{Per}} = \frac{4L_1 Br_1}{2L_1 + 2Br_1} = \frac{2L_1 Br_1}{L_1 + Br_1} \quad \text{Equation C76}$$

Substituting the Equations C74, C75 and C76 yield an expression for the friction factor.

$$f_1 = \frac{64\mu_w (L_1 + Br_1)}{2\rho_w V_w L_1 Br_1} = \frac{32\mu_w (L_1 + Br_1)}{\rho_w V_w L_1 Br_1} \quad \text{Equation C77}$$

The friction force term becomes:

$$F_f = \rho_w \frac{32\mu_w (L_1 + Br_1)}{4\rho_w V_w L_1 Br_1} \frac{V_w^2}{2} = \frac{4\mu_w (L_1 + Br_1)}{L_1 Br_1} V_w \quad \text{Equation C78}$$

Formulation:

$$p_w A_{wi,o} - p_1 A_1 - \rho_w g (H_w + z) A_1 - \frac{4\mu_w (L_1 + Br_1)}{L_1 Br_1} V_w = V_w \dot{m}_w + m_w \dot{V}_w - V_{wi,o} \dot{m}_{wi,o} \quad \text{Equation C79}$$

$$V_w = V_{wi,o} \quad \text{Equation C80}$$

CV W velocity is assumed to be velocity of the OWC centre of gravity and equal to velocity of the water entering the CV.

$$p_w A_{wi,o} - p_1 A_1 - \rho_w g (H_w + z) A_1 - \frac{4m_w (L_1 + Br_1)}{L_1 Br_1} V_{wi,o} = m_{wi,o} \dot{V}_{wi,o} \quad \text{Equation C81}$$

$$\dot{V}_{wi,o} = \frac{1}{m_{wi,o}} \left[p_w A_{wi,o} - p_1 A_1 - \rho_w g (H_w + z) A_1 - \frac{4\mu_w (L_1 + Br_1)}{L_1 Br_1} V_{wi,o} \right] \quad \text{Equation C82}$$

Simplifying the expression, remembering all cross-sectional areas are equal:

$$\ddot{z}_{wi,o} = \frac{1}{\rho_w A_1 (H_w + z)} \left[p_w A_1 - p_1 A_1 - \rho_w g (H_w + z) A_1 - \frac{4\mu_w (L_1 + Br_1)}{L_1 Br_1} \dot{z}_{wi,o} \right] \quad \text{Equation C83}$$

$$\ddot{z}_{wi,o} = \frac{1}{r_w (H_w + z)} \left[p_w - p_1 - r_w g (H_w + z) - \frac{1}{A_1} \left(\frac{4m_w (L_1 + Br_1)}{L_1 Br_1} \right) \dot{z}_{wi,o} \right] \quad \text{Equation C84}$$

Since equation C84 excludes added mass and damping terms, they are included below.

$$\ddot{z}_{wi,o} = \frac{1}{\rho_w (H_w + z) + M_a / A_1} \left[p_w - p_1 - \rho_w g (H_w + z) - \frac{1}{A_1} \left(\frac{4\mu_w (L_1 + Br_1)}{L_1 Br_1} + N \right) \dot{z}_{wi,o} \right] \quad \text{Equation C85}$$

B2.5.3. Driving force:

The fluctuation of subsurface pressure drives air flow through the SEWC. The function is integrated over the projected length of a chamber (length with respect to incident wave direction) averaging over the length OWC opening (Equation C86).

$$\begin{aligned} \bar{p}_w = \frac{1}{x_2 - x_1} \int_{x_1}^{x_2} & \left[\frac{\rho_w g H \cosh(2\pi(z_{sub} + d)/L_w)}{2 \cosh(2\pi d/L_w)} \cos(\theta) - \rho_w g z_{sub} + p_a \right. \\ & + \frac{3}{8} \frac{\rho_w g \pi H^2 \tanh(2\pi d/L_w)}{L_w \sinh^2(2\pi d/L_w)} \left(\frac{\cosh(4\pi(z_{sub} + d)/L_w)}{\sinh^2(2\pi d/L_w)} - \frac{1}{3} \right) \cos(2\theta) \\ & \left. - \frac{1}{8} \frac{\rho_w g \pi H^2 \tanh(2\pi d/L_w)}{L_w \sinh^2(2\pi d/L_w)} \left(\cosh \frac{4\pi(z_{sub} + d)}{L_w} - 1 \right) \right] dx \end{aligned} \quad \text{Equation C86}$$

The result of the integration is presented bellow, Equation C87.

$$\begin{aligned} \bar{p}_w = \frac{1}{x_2 - x_1} & \left[\rho_w g \frac{H}{2k} \frac{\cosh(2\pi(z_{sub} + d)/L_w)}{\cosh(2\pi d/L_w)} \sin(\omega t - kx) - \rho_w g z_{sub} x \right. \\ & + \frac{3}{8} \rho_w g \frac{\pi H^2}{2k L_w} \frac{\tanh(2\pi d/L_w)}{\sinh^2(2\pi d/L_w)} \left(\frac{\cosh[4\pi(z_{sub} + d)/L_w]}{\sinh^2(2\pi d/L_w)} - \frac{1}{3} \right) \sin(2\omega t - 2kx) \\ & \left. - \frac{1}{8} \rho_w g \frac{\pi H^2}{L_w} \frac{\tanh(2\pi d/L_w)}{\sinh^2(2\pi d/L_w)} \left(\cosh \left(\frac{4\pi(z_{sub} + d)}{L_w} \right) - 1 \right) x + p_a x \right]_{x_1}^{x_2} \end{aligned} \quad \text{Equation C87}$$

B3. Model assembly

The model is connected through the flow of mass from between CVs. The accumulation of mass and losses influence the system pressure fluctuations.

Appendix C: Simulink modelling process.

Block diagrams used in the modelling process described in chapter 4 are presented.

C1. Introduction

State equations are expressed in block diagrams and solved numerically using a Runge-Kutta numerical integration technique.

C2. Block diagrams

A detailed description of the states equations and models which they describe is found in chapter 4.

C2.1. Closed chamber model

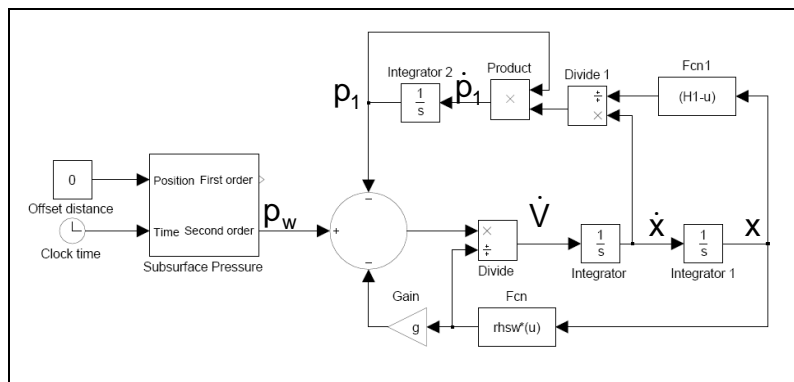


Figure C1: Closed chamber Simulink model.

The subsurface pressure block shown in Figure C1 (Figure C2) produces pressure signals of either first or second order for inputs of time and distance from the origin of the wave form.

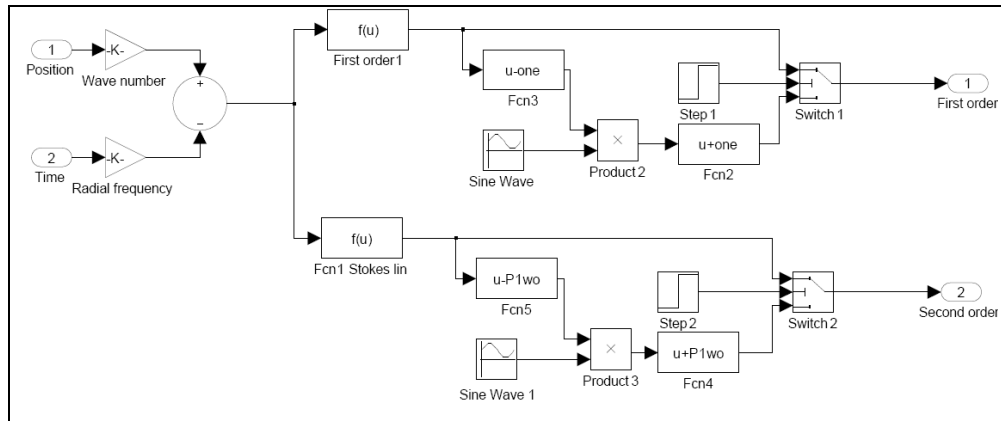


Figure C2: Subsurface pressure block set.

To reduce the effect of mismatched initial and boundary conditions subsurface pressure signal amplitude is increased in the form of a sinusoidal ramp, Figure C3.

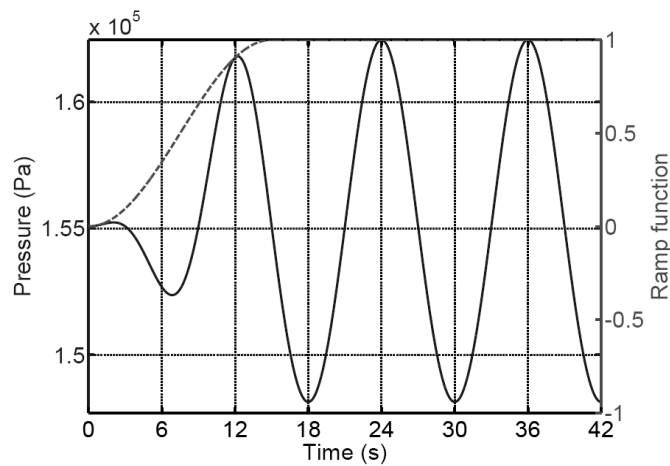


Figure C3: Subsurface pressure ramping function.

Many block sets in preceding models are interchangeable with models of lower complexity, making the modelling process easier and less prone to error.

C2.2. Single chamber exhausting through a turbine

Figure C4 shows the use of generic block sets, subsurface pressure and OWC.

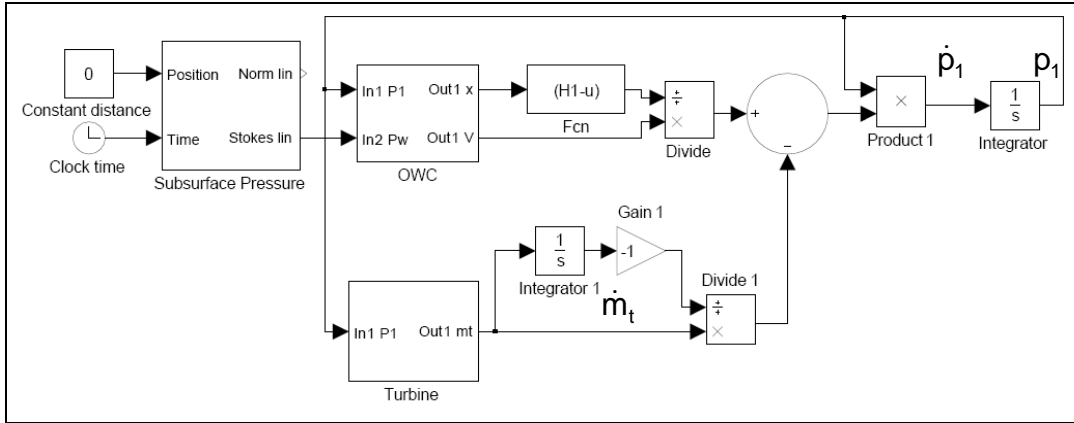


Figure C4: Bidirectional turbine block diagram.

Ellipse law is implemented in the turbine subsystem (Figure C5) for bidirectional flow.

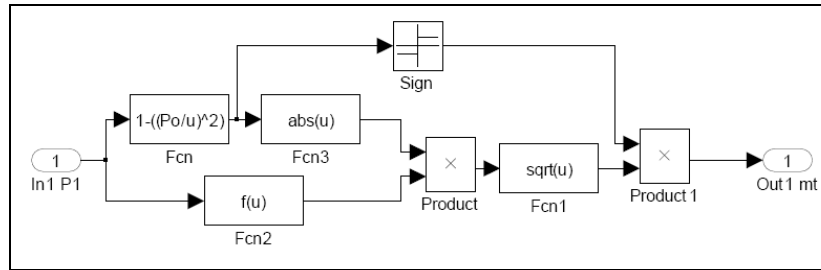


Figure C5: Turbine subsystem.

C2.3. Chamber exhausting to an auxiliary volume

New subsystems calculating flow through the connecting duct and pressure in the auxiliary volume are introduced (Figure C6).

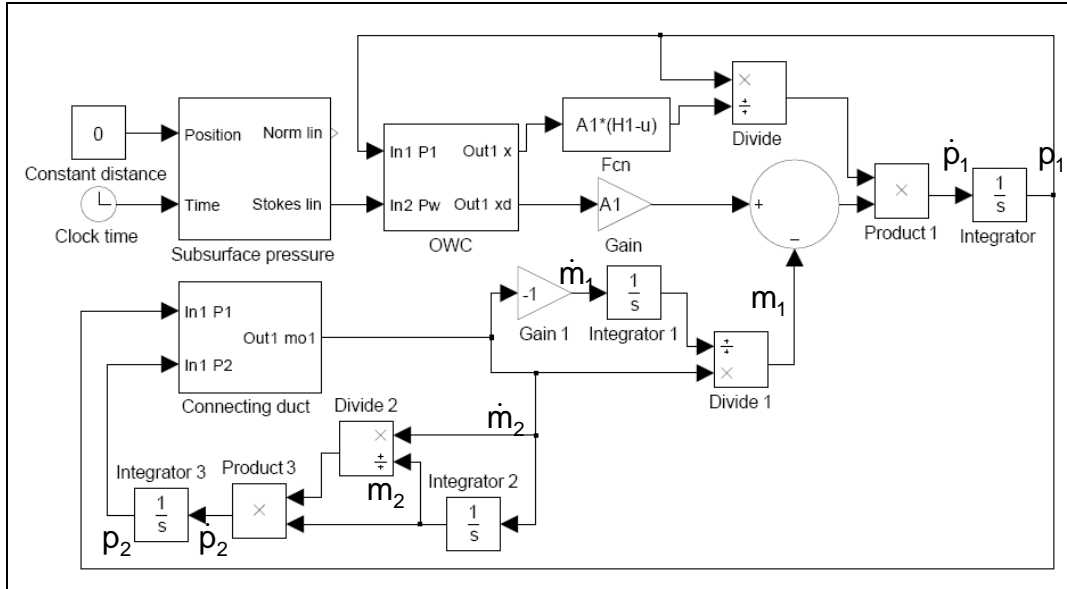


Figure C6: Chamber connected to an auxiliary duct.

The connecting duct flow is implemented in a subsystem, Figure C7.

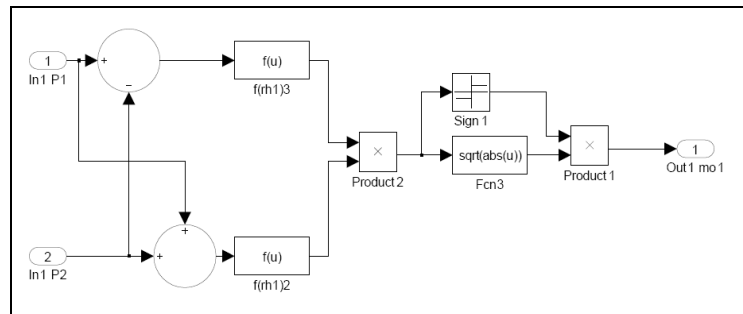


Figure C7: Connecting duct subsystem.

Function blocks following summation blocks contain the loss coefficients implemented in the pipe flow equation (Figure C7).

C2.4. Chamber exhausting through turbine to collecting chamber

All block arrangements have been explained and dealt with previously.

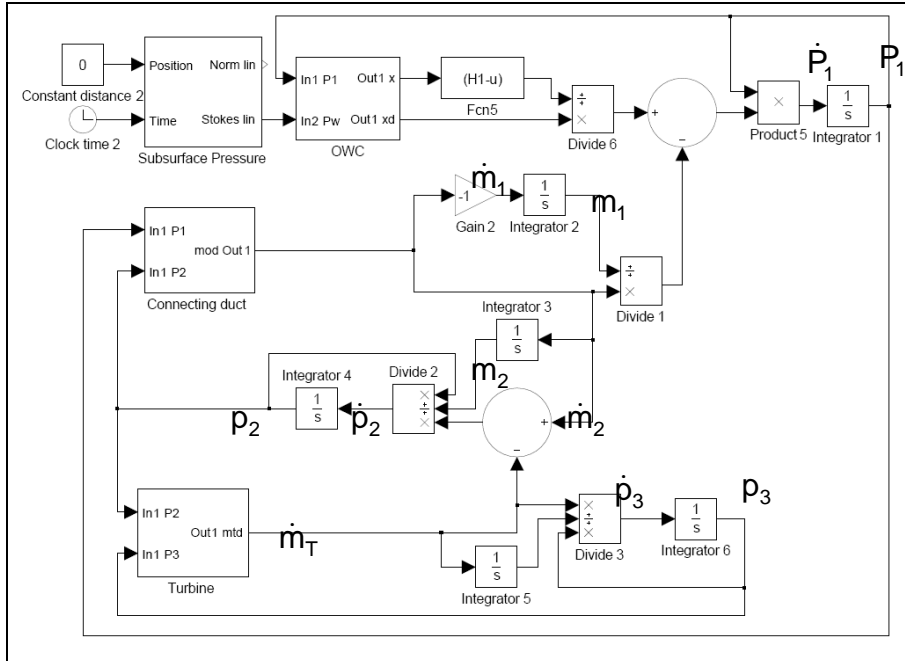


Figure C8: OWC chamber connected to an auxiliary volume and a turbine.

C2.5. Full single chambered model.

Model is now organized into subsystems (Figure C9), which make full system assembly it easier. It is necessary only to duplicate blocks to the left of the Pressure CV 2 block.

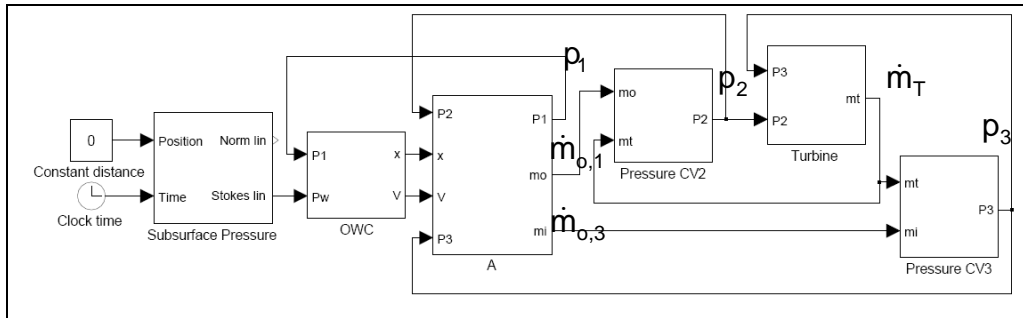


Figure C9: Full single chambered model.

Subsystem A (Figure C10) is a collection of blocks describing the flow in CV 1.

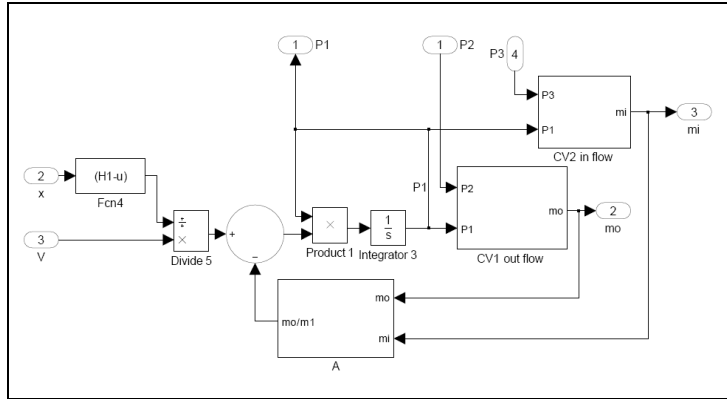


Figure C10: Subsystem A.

C2.6. Full converter

Full converter is assembled by duplicating the first three blocks of Figure C9 and offsetting the distance by which the chambers are spaced.

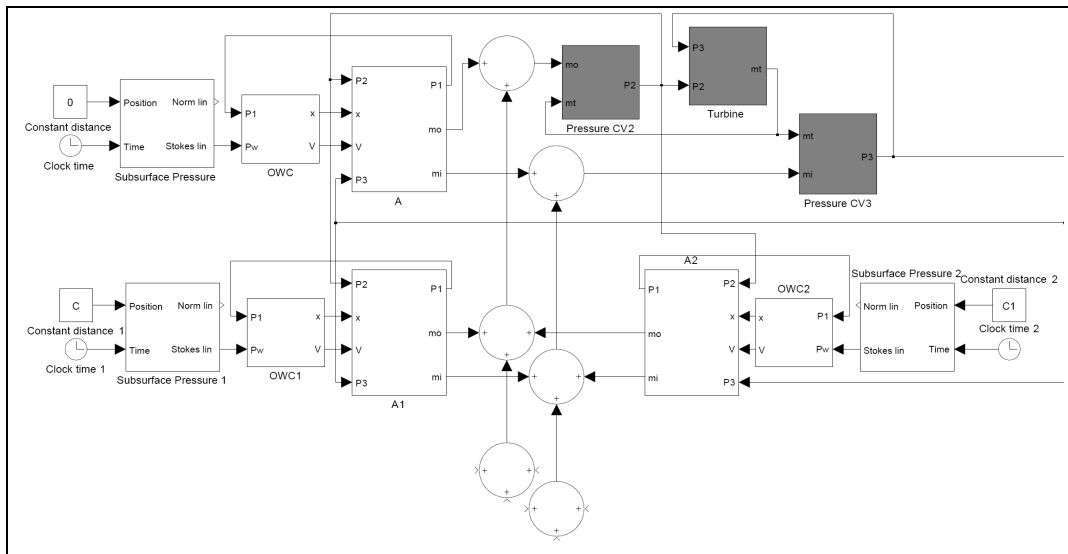


Figure C11: Coupling of single OWC systems into the full SWEC system.

C3) Conclusion

All state equations are now represented in the block diagram shown in Figure C11 in the simplest possible manner.

Attached CD

Wave energy and power

The derivation is summarized from Coastal (2006) for the sake of explanation and completeness. Linear wave theory is assumed.

1. Wave energy

Energy entrained in a moving mass can be described by summing kinetic and potential energy components.

1.1. Kinetic energy

Kinetic energy is associated with the motion of the water particles and is defined per unit wave crest length in by Equation 1.

$$\bar{E}n_k = \int_x^{x+L_w} \int_{-d}^n \rho_w \frac{u^2 + w^2}{2} dz dx \quad \text{Equation 1}$$

$$\bar{E}n_k = \frac{1}{16} \rho_w g H_w^2 L_w \quad \text{Equation 2}$$

1.2. Potential energy

Potential energy is associated with the mass of water in a wave lying either above or below the SWL and expressed mathematically in Equation 3

$$\bar{E}n_p = \int_x^{x+L_w} \rho_w g \left[\frac{(n+d)^2}{2} - \frac{d^2}{2} \right] dx \quad \text{Equation 3}$$

$$\bar{E}n_p = \frac{1}{16} \rho_w g H_w^2 L_w \quad \text{Equation 4}$$

Airy (1845) showed that if potential energy is calculated relative to the SWL and that if waves propagate in the same direction, both components are equal. The total energy is the sum of both components (Equation 5).

$$E_n = E_{n_k} + E_{n_p} = \frac{1}{8} \rho_w g H_w^2 L_w \quad \text{Equation 5}$$

Average energy per unit length is expressed in Equation 6.

$$\bar{E}n = \frac{E_n}{L_w} = \frac{1}{8} \rho_w g H_w^2 \quad \text{Equation 6}$$

2. Wave power

Coastal (2006) states that the energy transmitted in waves are defined as the rate at which energy is transmitted along the wave length and water depth (to witch its influence perceptible). Power transmitted in shallow water is defined by Equations 7 and 8.

$$\bar{P} = \frac{1}{\tau} \int_t^{t+\tau} \int_{-d}^n p u d z d t \quad \text{Equation 7}$$

$$\bar{P} = n C \bar{E} n = C_g \bar{E} n \quad \text{Equation 8}$$

The constant n (Coastal, 2006) in Equation 8 is defined in Equation 9.

$$n = \frac{1}{2} \left[1 + \frac{4\pi d / L_w}{\sinh(4\pi d / L_w)} \right] \quad \text{Equation 9}$$

Equation 10 expresses power transmitted in deep water (Coastal, 2006).

$$\bar{P} = \frac{1}{2} \bar{E} n C_w = \frac{1}{2} \bar{E} n \frac{L_w}{\tau} \quad \text{Equation 10}$$

In deep water wave length can be specified as in Equation 11.

$$L_w = \frac{g \tau^2}{2\pi} \quad \text{Equation 11}$$

Substituting Equation 11 into 10 yields Equation 12.

$$\bar{P} = \frac{1}{2} \bar{E} n C_w = \frac{g}{4\pi} \bar{E} n \tau \quad \text{Equation 12}$$

From Equation 6 we know the mathematical definition energy. Equation 13 describes the average power in a sea state with identical waves.

$$\bar{P} = \frac{1}{2} \bar{E} n C_w = \frac{\rho_w g^2}{32\pi} H_w^2 \tau \quad \text{Equation 13}$$

3. Statistical estimation of wave energy in a random sea

In an actual sea no two waves will be of equal height, length and period.

$$\bar{P} = \kappa H_w^2 \tau \quad \text{Equation 14}$$

It is standard practice of wave spectra to collect the fraction in Equation 13 and a wave spectrum constant into one (Equation 14). JONSWAP being the most widely used wave spectrum (Brooke, 2003) uses κ equal to 0.57.

Verification SWEC numerical model.

The model is verified by ensuring mass and energy conservation at every time step.

1. Introduction

The verification is explained by presenting a simple model so as the reader can be familiarized with the process, then the final model is then presented.

2. Validation models

Both models have already been investigated, therefore no block diagrams or state equations will be presented, Figure 1.

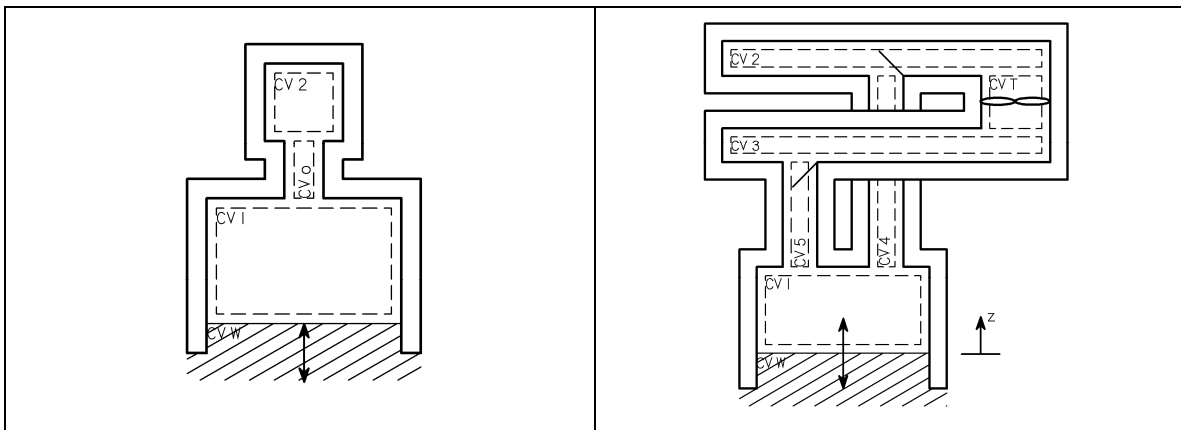


Figure 1: Models used for explanation.

The initial model includes an auxiliary volume and connecting duct. The final model is a single chambered version of the full system, it has all components (loss mechanisms) present in the full system for this reason its validity proves the system validity.

3. Results and model validation

Model results are presented below. All the models run for 42 seconds as this period is sufficient to present all the recurring dynamics in the systems. The definition of net power and work is the sum of all power and work done on or by the system.

3.1. Model 1: OWC exhausting to an auxiliary volume

Figure 2 shows no net gain or loss of mass or energy the system. The system is closed and one can see that most work done on the system by OWC is removed by the OWC.

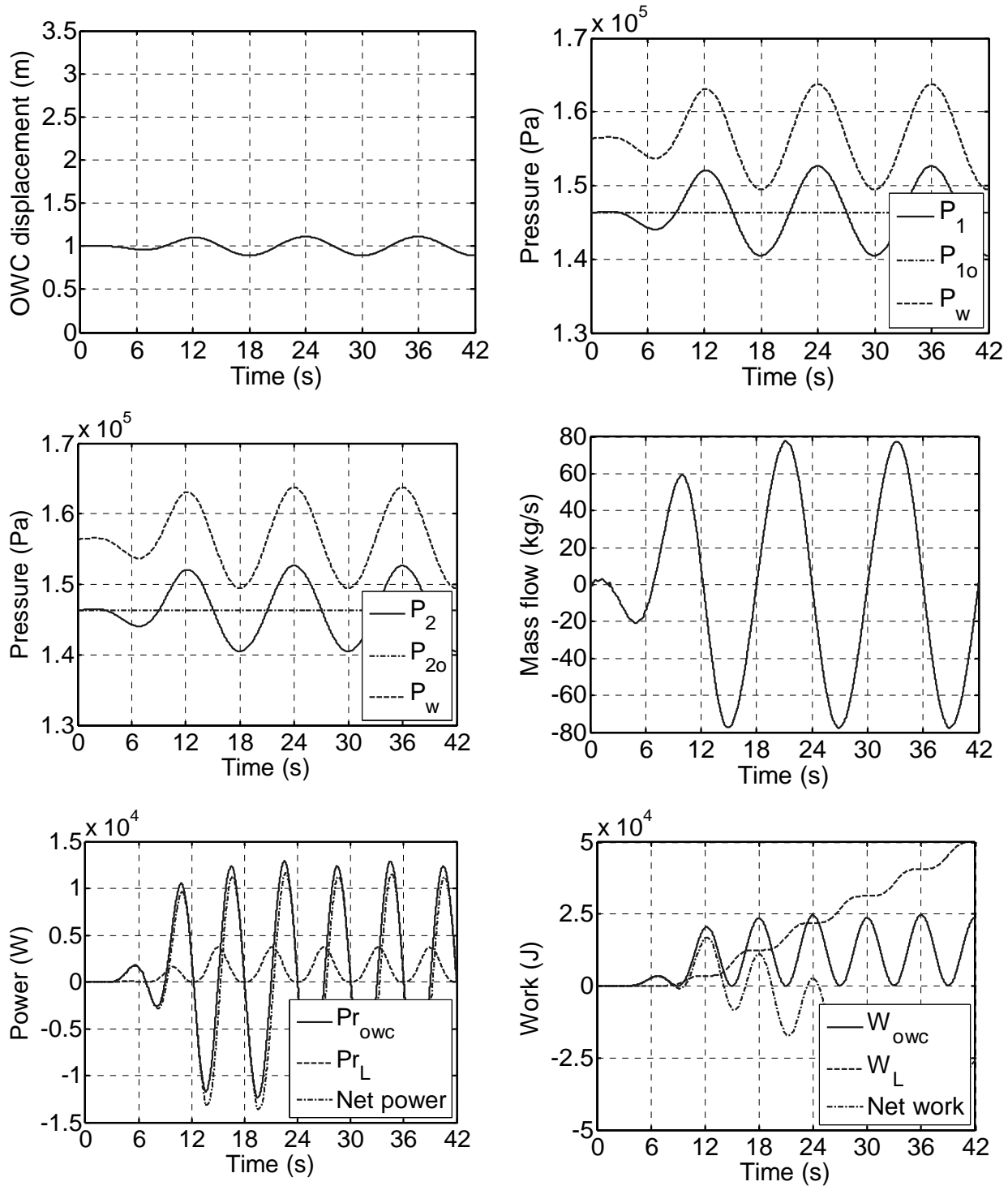


Figure 2: OWC displacement, pressure fluctuations, mass flow, power and work produced and dissipated in the system.

3.2. Model 2: OWC chamber connected to turbine via manifolds

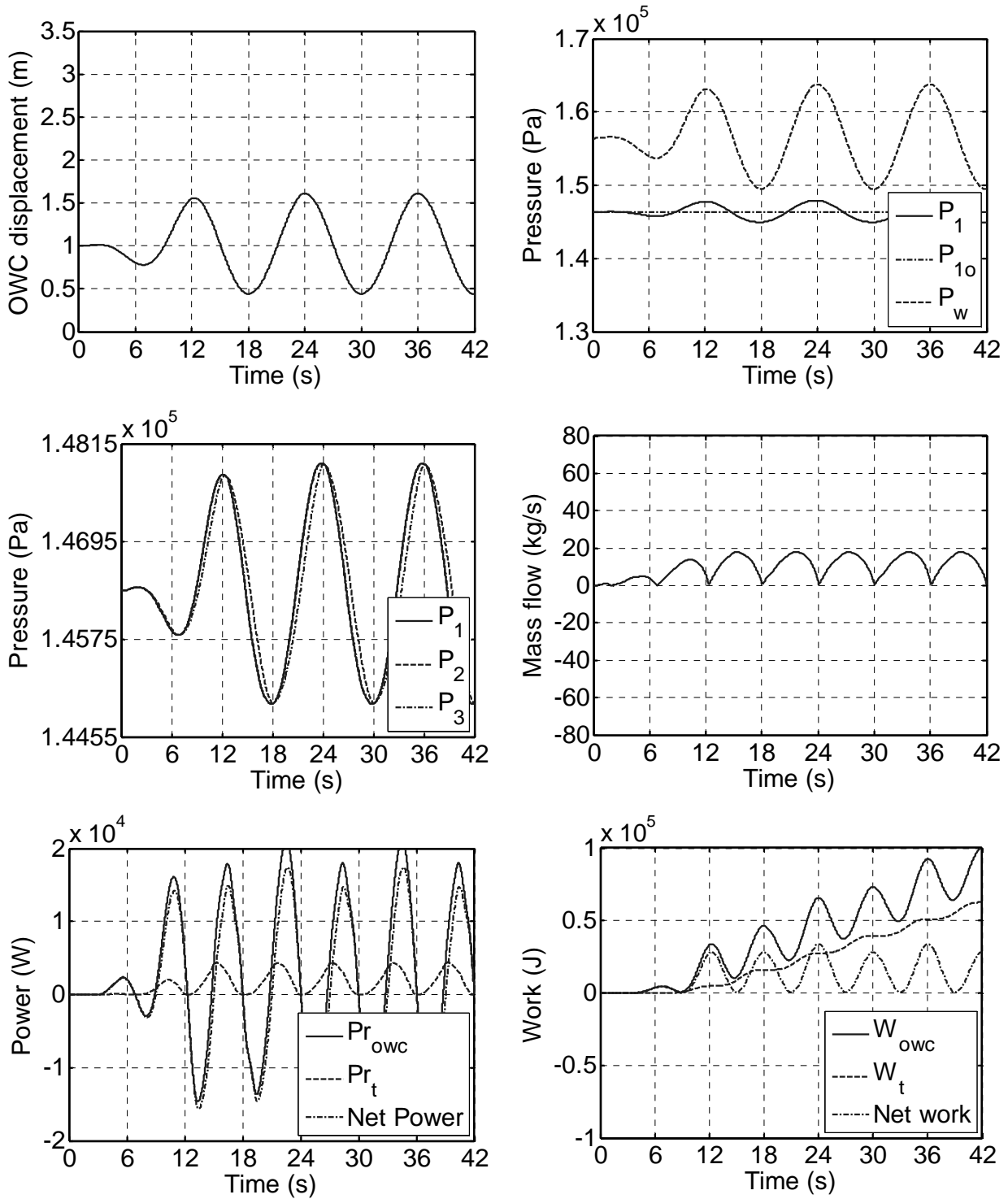


Figure 3: OWC displacement, pressure fluctuations, mass flow, power and work produced by the OWC and dissipated in the system.

Figure 3 shows how CV 2 is “pumped up” and air is drawn from CV 3 into CV 1. On careful inspection an increase and decrease in CV 3 and 2 pressure is noticed as air is “bled” through the turbine when not forced by the OWC.

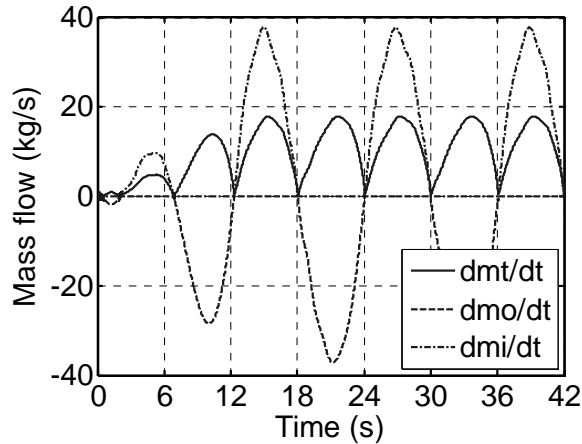


Figure 4: Mass flowing through turbine, in and out of CV1.

Figure 4 shows that the mass forced out CV 1 is drawn back when a favourable pressure gradient actuates valve operation. The majority of the work done on the system by the OWC is again removed by the OWC, the remainder is extracted by the turbine and dissipated through duct losses, Figure 5.

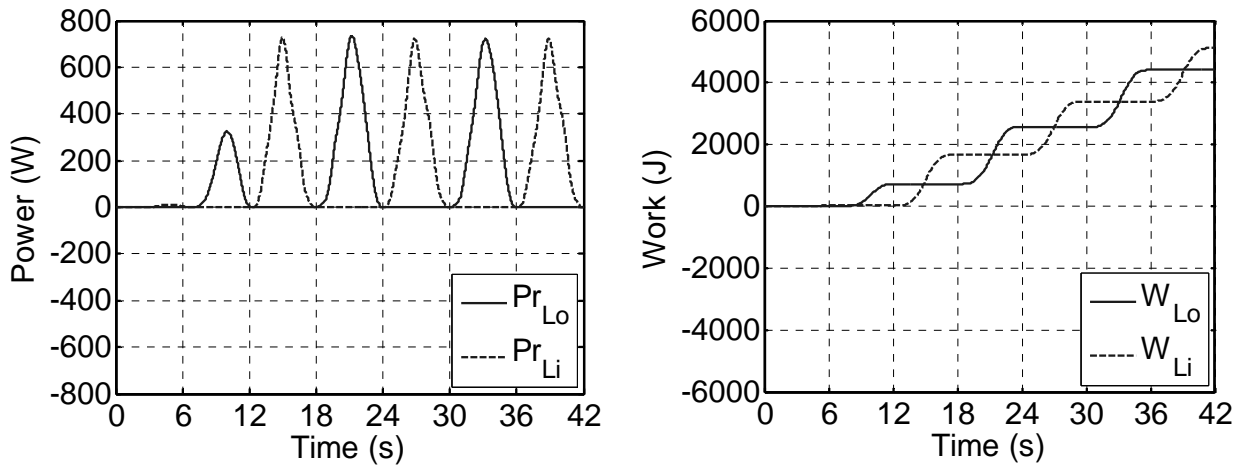


Figure 5: Rate of work loss and work dissipated through ducts.

4. Conclusion

Model validity is determined through the verification of conservation of mass and energy. In the models both of these conditions are shown to be satisfied.

2D sample calculation

To illustrate the 2D design program algorithm the following sample calculation is presented for mean annulus flow.

1. Environmental conditions

These properties define the conditions that the turbine is subject to, both environmentally conditions (pressure, temperature, gravitational acceleration etc) and fluid properties (gas constants, specific heat ratios etc).

$p_a = 101325 \text{ Pa}$	Atmospheric pressure
$T_w = 288.15 \text{ K}$	Water temperature
$g = 9.807 \text{ m/s}^2$	Gravitational acceleration constant
$R_a = 287.08 \text{ m}^2/\text{s}^2\text{K}$	Specific gas constant air
$R_v = 461.52 \text{ m}^2/\text{s}^2\text{K}$	Specific gas constant vapour
$\gamma_a = 1.4$	Specific heat ratio air

2. Program inputs

The program inputs include quantities needed to run the design program for various flow conditions (wave conditions).

2.1. Flow inputs

Of primary concern is the flow condition, which includes flow rate, pressure drop over turbine and diffuser blockage. With these inputs the design can be initiated.

$Q_t = 215.63 \frac{\text{m}^3}{\text{s}}$	Air flow rate through turbine
$\Delta p_t = 9233.3 \text{ Pa}$	Pressure drop over turbine
$B_3 = 0.02$	Diffuser inlet blockage

2.2. Turbine inputs

Turbine, diffuser, blade dimensions and mean radius are included in this section.

$\lambda=0.4$	Hub to tip ratio
$D_T=2.5\text{m}$	Turbine tip diameter
$D_H=\lambda D_T=1\text{m}$	Turbine hub diameter
$\lambda=0.4$	Hub to tip ratio
$D_T=2.5\text{m}$	Turbine tip diameter
$D_H=\lambda D_T=1\text{m}$	Turbine hub diameter
$D_m = \frac{1}{2} \sqrt{\left(\frac{D_T}{2}\right)^2 + \left(\frac{D_H}{2}\right)^2} = 1.9\text{m}$	Mean radius
$H_S = H_R = \frac{D_T - D_H}{2} = 0.75\text{m}$	IGV and rotor blade height
$r_{ra} = \frac{r_m}{r_m} = 1$	Radius ratio mean radius
$A_1 = \pi \left[\left(\frac{D_T}{2}\right)^2 - \left(\frac{D_H}{2}\right)^2 \right] = 4.123\text{m}^2$	Turbine cross sectional area
$\Psi_S = \Psi_R = 0.9$	Zwiefel space chord ratio (rotor and IGV)

2.3. Diffuser inputs

$D_3 = D_T$	Inlet diameter
$D_4 = 2 \sqrt{2 \left(\frac{\pi}{4}\right) \frac{D_{man}^2}{\pi}}$	Outlet diameter
$A_3 = A_1$	Inlet cross sectional area
$A_4 = \pi \left(\frac{D_4}{2}\right)^2$	Outlet cross sectional area

$$L_{\text{diff}} = 12\text{m}$$

Outlet cross sectional area

$$AR = \frac{A_4}{A_3} = 2.88$$

Area ratio

$$\delta = \text{atan}\left(\frac{D_4 - D_3}{2L_{\text{diff}}}\right) = 0.072\text{rad}$$

Divergence angle

$$C_{p_{\text{id}}} = 1 - \left(\frac{1}{AR}\right)^2 = 0.879$$

Ideal coefficient of performance

$$AR_f = AR(100B_3)^{\frac{1}{4}} = 3.425$$

Area ratio function (Sovran, 1967)

$$E_4 = 0.734$$

Effective outlet area fraction (Sovran, 1967)

$$A_{3\text{eff}} = A_3 - B_3 A_3 = 4.811\text{m}^2$$

Effective inlet area

$$E_3 = \frac{A_{3\text{eff}}}{A_3} = 0.98$$

Effective inlet area fraction (Sovran, 1967)

$$\vartheta = \frac{1}{E_3^2} \left[\left(1 - \frac{(E_3/E_4)^2}{AR^2} \right) / \left(1 - \frac{1}{AR^2} \right) \right] = 0.93$$

Diffuser effectiveness (Sovran, 1967)

$$C_p = \vartheta C_{p_{\text{id}}} = 0.817$$

Ideal coefficient of performance

$$K_{\text{diff}} = C_{p_{\text{id}}} - C_p = 0.062$$

Ideal coefficient of performance

2.4. Design variables

The following variables can be adjusted at the designer's discretion.

$$N_s = 29$$

Number of IGVs

$$N_R = 13$$

Number of rotor blades

$$N_s = 1500\text{rpm} = 157.1 \frac{\text{rad}}{\text{s}}$$

Number of rotor blades

$$U_m = N_s \frac{D_m}{2} = 149.535 \frac{\text{m}}{\text{s}}$$

Mean rotor blade speed

2.5. Fluid properties

Fluid properties (although calculated anew in each iteration) are presented here. This is done as to simplify the explanation of the body of the iteration process.

2.5.1. Station 1: IGV inlet

$p_{01}=143690\text{Pa}$	Total pressure
$T_{01}=288.15\text{K}$	Total pressure
$C_{p1}=1006.6\frac{\text{J}}{\text{kgK}}$	Specific heat at constant pressure
$p_1=141362\text{Pa}$	Static pressure
$T_1=286.81\text{K}$	Static pressure
$\rho_1=1.7022\frac{\text{kg}}{\text{m}^3}$	Density
$\mu_1=1.7785\times 10^{-5}\frac{\text{kg}}{\text{ms}}$	Dynamic viscosity
$\nu_1=1.0449\times 10^{-5}\frac{\text{m}^2}{\text{s}}$	Kinematic viscosity

2.5.2. Station 2: Rotor-IGV gap properties

$p_{02}=143570\text{Pa}$	Total pressure
$T_{02}=288.15\text{K}$	Total pressure
$C_{p2}=1006.5\frac{\text{J}}{\text{kgK}}$	Specific heat at constant pressure
$p_2=141254\text{Pa}$	Static pressure
$T_2=286.26\text{K}$	Static pressure
$\rho_2=1.6933\frac{\text{kg}}{\text{m}^3}$	Density

$$\mu_2 = 1.7762 \times 10^{-5} \frac{\text{kg}}{\text{ms}}$$

Dynamic viscosity

$$v_2 = 1.0490 \times 10^{-5} \frac{\text{m}^2}{\text{s}}$$

Kinematic viscosity

2.5.3. Station 3: Rotor exit

$$p_{03} = 143570 \text{ Pa}$$

Total pressure

$$T_{03} = 283.25 \text{ K}$$

Total pressure

$$C_{p3} = 1006.5 \frac{\text{J}}{\text{kgK}}$$

Specific heat at constant pressure

$$p_3 = 132230 \text{ Pa}$$

Static pressure

$$T_3 = 281.89 \text{ K}$$

Static pressure

$$\rho_3 = 1.6232 \frac{\text{kg}}{\text{m}^3}$$

Density

$$\mu_3 = 1.7762 \times 10^{-5} \frac{\text{kg}}{\text{ms}}$$

Dynamic viscosity

$$v_3 = 1.0490 \times 10^{-5} \frac{\text{m}^2}{\text{s}}$$

Kinematic viscosity

2.6. Initial program calculations

The following parameters remain constant regardless of the value of the estimated efficiency (updated by the iteration process) are grouped with respect to stations.

2.6.1. Station 1

Flow is assumed to approach the IGV axially (no swirl).

$$\alpha_{1m} = 0 \text{ rad}$$

Flow angle to actual flow vector

$$C_{1m} = \frac{Q_t}{A_1} = 52.295 \frac{\text{m}}{\text{s}}$$

Actual mean flow velocity

2.6.2. Station 3

Turbine exit flow is set to flow axially.

$$\beta_{3m} = \text{atan}\left(\frac{U_m}{C_{3m}}\right) = 1.234 \text{ rad}$$

Flow angle to relative flow vector

$$\alpha_{3m} = 0 \text{ rad}$$

Flow angle to actual flow vector

$$V_{3m} = \sqrt{U_m^2 + C_{3m}^2} = 158.42 \frac{\text{m}}{\text{s}}$$

Relative mean flow velocity

$$C_{3m} = C_{1m} = 52.295 \frac{\text{m}}{\text{s}}$$

Actual mean flow velocity

2.7. Flow variables

$$\varphi_m = \frac{C_a}{U_m} = 0.35$$

Flow coefficient

$$p_{ra} = \frac{p_{01}}{p_{02}} = 1.069$$

Turbine total pressure ratio

2.8. Convergence loop Initial values

These values are used in the convergence statement, gauging accuracy of the solution.

$$\eta_{tt} = 0.9$$

Estimate of turbine total-total efficiency

$$\Delta T_0 = \eta_{tt} T_{01} \left[1 - (p_{03}/p_{01})^{(\gamma_a - 1/\gamma_a)} \right] = 5.14 \text{ K}$$

Estimate of turbine total-total efficiency

2.9. Initiation of convergence loop

$$T_{03} = T_{01} - \Delta T_0 = 283.05 \text{ K}$$

Estimate of turbine total-total efficiency

Station 3 fluid properties updated.

$$\overline{C_p} = \frac{C_{p1} + C_{p2} + C_{p3}}{3} = 1006.6 \frac{\text{J}}{\text{kgK}}$$

Average specific heat

2.10. Flow variables

$$\psi_m = \frac{2\overline{C_p}\Delta T_0}{U_m^2} = 0.465$$

Load coefficient

2.10.1. Station 2

$$\beta_{2m} = \text{atan}\left(\frac{\Psi_m}{2\phi_m} - \tan(\beta_{3m})\right) = -1.143 \text{ rad}$$

Flow angle to relative flow vector

$$\alpha_{2m} = \text{atan}\left(\frac{1}{\phi_m} - \tan(\beta_{2m})\right) = 0.586 \text{ rad}$$

Flow angle to actual flow vector

$$V_{2m} = \frac{\phi_m U_m}{\cos(\beta_{2m})} = 126.15 \frac{\text{m}}{\text{s}}$$

Relative mean flow velocity

$$C_{2m} = \frac{\phi_m U_m}{\cos(\alpha_{2m})} = 62.78 \frac{\text{m}}{\text{s}}$$

Actual mean flow velocity

2.11. Turbine analysis

Reaction ratio is to be kept between 0 and 1 and Zweifel criterion is presented, manipulated to calculate chord distributions and blade numbers.

$$\Lambda_m = \frac{C_a}{2U_m} [\tan(\beta_{3m}) - \tan(\beta_{2m})]$$

Reaction ratio

2.11.1. IGVs

$$\zeta_{Sm} = \frac{\alpha_{1m} + \alpha_{2m}}{2} = 0.293 \text{ rad}$$

Initial estimate of stagger angle

$$sc_{aS} = \frac{\Psi_s}{2\cos^2(\alpha_{2m}) [\tan(\alpha_{1m}) + \tan(\alpha_{2m})]} = 0.976$$

Axial space to chord ratio

$$sc_S = sc_{aS} \cos(\zeta_{Sm}) = 0.935$$

Actual space to chord ratio

$$s_{Sm} = \frac{\pi D_m}{N_S} = 0.206 \text{ m}$$

Blade pitch

$$c_{aSm} = \frac{s_{Sm}}{sc_{aSm}} = 0.211 \text{ m}$$

Axial blade chord

$$c_{Sm} = \frac{s_{Sm}}{sc_{Sm}} = 0.221 \text{ m}$$

Actual blade chord

$$Dh_S = \frac{2h_S s_{Sm} \cos(\alpha_{2m})}{s_{Sm} \cos(\alpha_{2m}) + h_S} = 0.28 \text{ m}$$

Hydraulic diameter

$$Re_S = \frac{1/2(\rho_1 + \rho_2) C_{2m} Dh_S}{1/2(\mu_1 + \mu_2)} = 1.608 \times 10^6$$

Reynolds number

2.11.2. Rotor

$$\zeta_{Rm} = \frac{-\beta_{2m} + \beta_{3m}}{2} = 1.189 \text{rad}$$

Initial estimate of stagger angle

$$SC_{aR} = \frac{\Psi_R}{2\cos^2(\beta_{3m})[\tan(\beta_{3m}) + \tan(\beta_{2m})]} = 6.218$$

Axial space to chord ratio

$$SC_R = SC_{aR} \cos(\zeta_{Rm}) = 2.317$$

Actual space to chord ratio

$$S_{Rm} = \frac{\pi D_m}{N_R} = 0.46 \text{m}$$

Blade pitch

$$c_{aRm} = \frac{S_{Rm}}{SC_{aRm}} = 0.074 \text{m}$$

Axial blade chord

$$c_{Rm} = \frac{S_{Rm}}{SC_{Rm}} = 0.199 \text{m}$$

Actual blade chord

$$Dh_R = \frac{2h_R S_{Rm} \cos(\alpha_{3m})}{S_{Rm} \cos(\alpha_{3m}) + h_R} = 0.57 \text{m}$$

Hydraulic diameter

$$Re_R = \frac{1/2(\rho_2 + \rho_3) C_{3m} Dh_R}{1/2(\mu_2 + \mu_3)} = 2.684 \times 10^6$$

Reynolds number

2.12. Soderburg's loss correlation

Soderburg relates IGV and rotor blade and diffuser losses to losses in static pressure.

2.12.1. IGVs

$$\epsilon_{Sm} = \alpha_{2m} - \alpha_{1m} = 0.586 \text{rad}$$

Fluid deflection

$$\xi_{Sm} = 0.025 \left[1 + \left(\frac{180 \epsilon_{Sm}}{90\pi} \right)^2 \right] = 0.028$$

Primary loss factor

$$\xi'_{Sm} = 3.2 \left(\frac{c_{aS}}{h_S} \right) = 0.026$$

Secondary loss factor

$$\xi_{Scorr} = \left(\frac{10^5}{Re_S} \right)^{1/4} = 0.499$$

Reynolds number correction factor

$$\xi_S = (\xi_{Sm} + \xi'_{Sm}) \xi_{Scorr} = 0.027$$

IGV loss coefficient

$$c_{Rm} = \frac{S_{Rm}}{SC_{Rm}} = 0.199 \text{m}$$

Actual blade chord

2.12.2. Rotor

$$\varepsilon_{Rm} = \beta_{3m} - \beta_{2m} = 0.091 \text{ rad}$$

Fluid deflection

$$\xi_{Rm} = 0.025 \left[1 + \left(\frac{180 \varepsilon_{Rm}}{90\pi} \right)^2 \right] = 0.025$$

Primary loss factor

$$\xi'_{Rm} = 3.2 \left(\frac{c_{aR}}{h_R} \right) = 0.00792$$

Secondary loss factor

$$\xi_{Rcorr} = \left(\frac{10^5}{Re_R} \right)^{1/4} = 0.439$$

Reynolds number correction factor

$$\xi_R = (\xi_{Rm} + \xi'_{Rm}) \xi_{Rcorr} = 0.015$$

IGV loss coefficient

$$c_{Rm} = \frac{s_{Rm}}{SC_{Rm}} = 0.199 \text{ m}$$

Actual blade chord

2.12.3. Diffuser

$$\xi_{diff} = K_{diff} = 0.062$$

Diffuser loss coefficient

At this point the convergence loop counter is incremented and the efficiency and the total pressure drop are recalculated.

$$\eta_{tt} = \left[1 + \frac{\xi_S C_{2m}^2 + \xi_R V_{3m}^2 + \xi_{diff} C_a^2}{U_m^2 \psi_m} \right]^{-1} = 0.94$$

Diffuser loss coefficient

$$\Delta T_0 = \eta_{tt} T_{01} \left[1 - (p_{03}/p_{01})^{(\gamma_a - 1/\gamma_a)} \right] = 5.358 \text{ K}$$

Estimate of turbine total-total efficiency

Station 2 fluid properties updated.

Design is considered converged if the difference between successive efficiency values is less than 1×10^{-6} .